Fragment-based screening and discovery of small molecule ligands for TIGIT and TIM-3

By

Tyson Alexander Rietz

Dissertation

Submitted to the faculty of the

Graduate School of Vanderbilt University

in partial fulfillment of the requirements

for the degree of

DOCTOR OF PHILOSOPHY

in

Biochemistry

May 31st, 2022

Nashville, Tennessee

Stephen W. Fesik, Ph.D.

Martin Egli, Ph.D. (Chair)

Raymond D. Blind, Ph.D.

Walter J. Chazin, Ph.D.

Young J. Kim, MD/Ph.D.

Dedicated to my wife, Anna, and our daughter, Vivian, for their endless love and support.

ACKNOWLEDGMENTS

I would first like to gratefully acknowledge and thank Dr. Stephen Fesik for giving me the opportunity to pursue my graduate work in his lab. Steve has kindly offered his guidance and support throughout the years for which I am incredibly thankful. The Fesik lab is a unique academic training environment that has collated several exceptional scientific minds all focused on the primary goal to drug the undruggable. I would like to thank the current and previous leadership team members of the lab, Drs. Taekyu Lee, Jason Phan, Alex Waterson, John Sensintaffar, and Edward Olejniczak, for their mentorship and for the many enlightening discussions on drug discovery. I would also like to thank my committee members Drs. Martin Egli, Ray Blind, Walter Chazin, and Young Kim for their collective support and critical analysis of my work. I also want to thank all staff, post-docs, and graduate students that I have worked along-side in the Fesik lab. You have been friends, teachers, trusted colleagues, and sources of inspiration for which I am forever grateful.

Drug discovery is a highly collaborative endeavor and I have been blessed to have worked with several highly talented scientists during my projects. Taekyu Lee's leadership on the projects discussed herein has been exceptional and I would not have been able to succeed without his guidance. Under his supervision, several medicinal chemists were key contributors of new chemical analogs that advanced our projects. For their chemistry contributions, I gratefully thank Kevin Teushcer, Jonathan Mills, Rocco Gogliotti, Lance Lepovitz, Rush Scaggs, and Keisuke Yoshida. I thank Bin Zhao and Jason Phan for their sharing their wealth of X-ray crystallography knowledge. Their

advice and support were immensely helpful at every stage of the crystallography process. Similarly, Edward Olejniczak was extremely supportive with NMR advice and assisted with the backbone resonance assignment of TIM-3, for which I am grateful. I would like to thank Kelvin Luong for his contributions to protein purification. I would like to thank Gabriel Rodriguez and Dr. Michael Korrer from Dr. Young Kim's lab for their work on TIM-3 cellular assays.

Vanderbilt has incredible research cores that support our drug discovery efforts and are staffed with highly talented scientists. I would like to thank Markus Voehler and Joel harp from the biomolecular NMR and crystallography cores, respectively, for their training and assistance. Their persistent help with experimental setup and troubleshooting always made me confident that my experiments would be successful. I would also like to thank Corbin Whitwell from the high throughput screening core for her assistance with the several expedited or customized compound plate requests.

Finally, I also gratefully acknowledge financial support from the Biochemical and Chemical Training for Cancer Research T32 Training Grant (3T32CA009582-29S1). The Vanderbilt Biomolecular NMR Center is supported in part by grants for NMR instrumentation from the NSF (0922862), NIH (S10 RR025677) and Vanderbilt University matching funds. The Vanderbilt robotic crystallization facility is supported by NIH grant S10 RR026915. Use of the Advanced Photon Source was supported by the U.S. Department of Energy, Office of Science, Office of Basic Energy Sciences, under Contract No. DE-AC02-06CH113.

TABLE OF CONTENTS

Page

LIST OF FIGURES

LIST OF TABLES

Chapter 1 - Introduction and Background

1.1 Cancer and the immune system.

Malignant cancers are the second leading cause of death in the United States. In 2022, the American cancer society estimates that 1.9 million new cases of cancer will be diagnosed in the United States and 609,360 people will die from this diagnosis, accounting for almost one quarter of all deaths.[1] Costs of cancer care were estimated to be $190.2 billion in 2015 and $208.9 billion in 2020, representing a significant and growing economic burden on the country largely due to aging and growth of the U.S. population.[2] Although these statistics seem grim, continued research has led to the development of new and better approaches to cancer prevention, detection, diagnosis, and treatment, which are driving down incidence and death rates. The age-adjusted cancer death rate has decreased by 26% from 1991 to 2015, translating into almost 2.4 million lives spared.[3] However significant this progress has been, cancer continues to pose massive public health challenges in the United States. Cancer is largely a disease of aging and as the segment of the U.S. population age 65 and older is growing, the projected number of people diagnosed with cancer increases dramatically in the coming decades, from 1,762,450 in 2019 to 2,387,304 in 2035 in the United States alone.[3] While prevention and detection methods will be important to limit this rise, a reliable therapeutic toolkit is necessary to combat existing and future diagnoses.

Progress in cancer research has given us a significantly more advanced understanding of how this collection of diseases functions at a molecular level. We have found that cancer is the result of several acquired mutations, aberrant protein expression, and the ineffective turnover of proteins effecting different molecular pathways from which

a cell ultimately develops capabilities that drive tumorigenesis. These acquired traits were initially summarized as the six “hallmarks of cancer,” which are: evasion of cell death, sustained angiogenesis, sustained proliferative signaling, resistance to anti-growth signaling, replicative immortality, and capabilities related to tissue invasion and metastasis.[4] The hallmarks of cancer present the picture of a cell that is insensitive to checks on growth, capable of recruiting the resources necessary to support unregulated proliferation, and able to expand into other organs and systems in ways that eventually prevent their normal function. Increased basic understanding of these hijacked molecular pathways has led to the rise of rationally designed therapeutics that specifically target defective signaling pathways in specific cancer types.

Targeted therapies have allowed healthcare providers to start to move away from broad-application cytotoxic chemotherapies that not only kill rapidly dividing cancer cells but also destroy vulnerable normal cells. Coupled with advances in cancer genome sequencing, targeted therapies provide for precision medicine strategies that can be tailored from patient to patient by selectively disrupting pathways necessary for cancer cell survival.[5] Indeed, drug discovery in the new era of precision medicine has yielded several successful stories targeting oncogenic kinases and receptors in specific patient populations as well as given rise to several companion diagnostics.[6] Hundreds of these type of drugs are currently under clinical development, however the overall success rate in bringing drugs to markets is in the range of only 5-8%.[7] Successes have been limited, in large part, because cancer is a heterogeneous disease and developing targeted therapies that are effective for all patients within a population remains a difficult challenge.[8] This difficulty is compounded by the fact that cancer cells are rapidly evolving

and are capable of developing resistance to targeted therapies. Not only can drug-resistant clonal populations preexist within a given tumor, more complex mechanisms of adoptive resistance include drug target alteration, drug inactivation, drug efflux, DNA damage repair, cell death inhibition, and epithelial-mesenchymal transition.[9] These issues highlight the need for new broadly applicable therapeutic approaches capable of battling the heterogeneous and evasive nature of cancer.

In 2011, the hallmarks of cancer were reexamined to reflect a decade's worth of additional research. New research suggests two additional enabling characteristics, genome instability and tumor-promoting inflammation, and two new emerging hallmarks, reprogramming of cellular energy metabolism and immune evasion.[10] While all of these new findings represent new potential therapeutic targets, immune evasion is a particularly unique opportunity if successfully reversed. Survival is critical for a budding tumor to gain a foothold, therefore finding ways to escape the host's anti-cancer immunity is critical. Natural immune defenses can be a crucial combatant against the survival of a budding tumor.

Immune defenses are uniquely adapted to combat cancerous cells through a high degree of specificity and adaptability that can compete with cancer heterogenicity.[11] Durable responses can also be accomplished through the development of immunological memory cells against cancer cells. Genome instability in cancerous cells gives rise to several genetic and epigenetic alterations that lead to the expression of mutated of aberrantly upregulated proteins, or neoantigens, that immune cells use to differentiate cancer cells from normal cells, a process known as immune surveillance.[12] Several studies have demonstrated that immune cell subsets including macrophages, neutrophils,

natural killer (NK) cells, dendritic cells (DCs), T cells, invariant NK T (iNKT) cells, and B cells all have roles in tumor-associated immune responses.[13] Given the diverse subset of cells capable of combatting a budding tumor it appears unlikely a tumor could survive and grow, yet tumor cells have adapted robust methods to evade immune surveillance and flourish. These studies highlight the potential for these immune cells to be therapeutically relevant if they could be re-sensitized or reinvigorated to again recognize and attack cancerous cells.

Cytotoxic $CD8^+$ T cells have been particularly shown to be critical actors in combating cancers. Several studies have contributed to our understanding of how these cytotoxic T lymphocytes (CTLs) modulate anti-tumor responses and further allow for the potential design of therapeutic strategies. T cell immunity involves multiple cyclic steps including clonal selection, activation, and proliferation by DCs followed by trafficking, recognition, and elimination of neoantigen-presenting cells (Figure 1-1). Importantly, CTL recognition of a neoantigen-presenting cell alone is not sufficient for a complete T cell activation and cytotoxic response. T cell activation is tightly regulated by a number of activating and inhibitory signaling pathways, termed immune checkpoints, that are necessary for immune homeostasis (Figure 1-2).[14] A fully activated T cell is not possible without co-stimulatory immune checkpoints and, conversely, deactivation of the same T cell is not possible without co-inhibitory immune checkpoints. This allows for a natural system of checks and balances to avoid uncontrolled immune responses, protect healthy cells from immune response damage, and prevent autoimmunity. In the context of cancer, this balance has been skewed to an immune deactivated state, also referred to as T cell

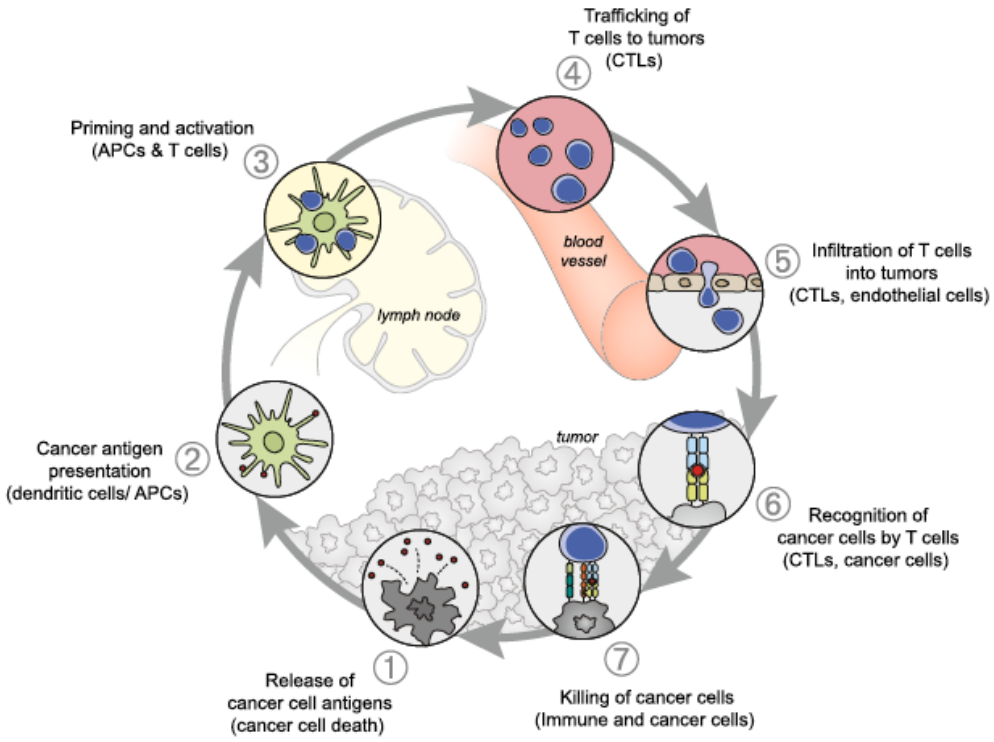

Figure 1-1. The cancer immunity cycle.
Natural immunity to cancer is a cyclic and self-propagating process. Immune stimulating factors are accumulated broadening and amplifying T cell responses. During this cyclic process, there are several inhibitory factors at every step that act as immune regulatory feedback mechanisms. These inhibitory factors can halt or limit the development of cancer immunity. Adapted from Chen, 2013.[15]

exhaustion, where T cells have become dysfunctional and is defined by poor effector function, sustained expression of co-inhibitory immune checkpoints, and a transcriptional state that is distinct from functional T cells.[16,17]

Immune checkpoint blockade (ICB) as a therapeutic modality to enhance the anti-tumor activity in T Cells was first hypothesized by James Allison and colleagues.[18] High affinity and avidity monoclonal antibodies (mAbs) raised to target and inhibit cytotoxic T lymphocyte associated protein 4 (CTLA-4) and programmed cell death protein 1 (PD-1) have been successful in combating advanced stage melanoma.[19] While their efficacy was initially proven in melanoma, these agents are not limited to a single cancer type due to

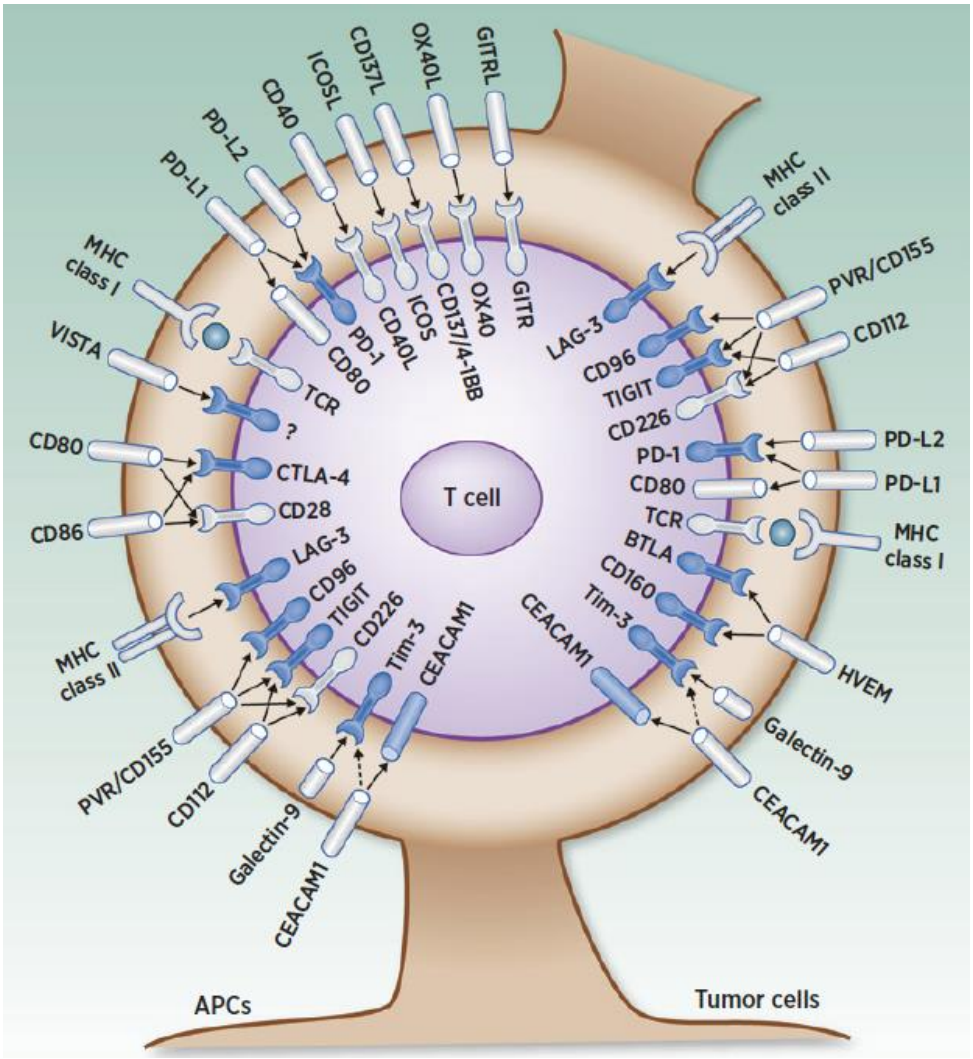

Figure 1-2. Co-inhibitory and co-stimulatory receptors that regulate T cell function.
Immune checkpoint receptors expressed by T cells bind their cognate ligands expressed by APCs or tumor cells and regulate T cell activity. Adapted from Zarour, 2016.[20]

their activation of immune defenses. Indeed, FDA-approved CTLA-4 and PD-1 pathway ICB has been shown to demonstrate durable responses in 16 different cancer types and their indications are still expanding.[21] Immune activating therapies have revolutionized the way physicians treat many cancer patients. Immunotherapy was recognized as Science's "breakthrough of the year" in 2013 and is now considered the 5th pillar of cancer treatment alongside surgery, radiation, targeted therapy, and chemotherapy.[22] Two pioneers in immunotherapy, James Allison and Tasuku Honjo, were awarded the 2018

Nobel Prize in Physiology or Medicine for their tremendous contributions to the basic understandings of cancer immunotherapy.

1.2 Current state of cancer immunotherapy.

The broad successes of ICB cancer immunotherapy are previously unprecedented. To date, FDA-approved mAbs are in clinical use for 16 different cancer types including both solid and hematological tumors. While these successes are profound, there are still outstanding concerns and questions that have yet to be fully addressed by the current research. One major question that has resulted from CTLA-4 and PD-1 blocking therapies is why 40-60% of patients fail to respond to treatment.[23] Response rates from single agent therapies have hovered around 20-30%, however, combination therapies that target both CTLA-4 and PD-1 pathways simultaneously have been shown to demonstrate response rates of 40-50%.[24] Because CTLA-4 and PD-1 checkpoint pathways have different mechanisms of T cell regulation, combination therapies that target both pathways have a synergistic effect resulting in increased response rates. These increased responses have driven considerable efforts to find additional combinatorial therapies with ICB mAb and other cancer treatment modalities or by targeting additional immune checkpoint pathways that will further increase response rates. Currently, there are over 1,000 clinical trials involving combination therapies of a ICB mAb with diverse therapy types including chemotherapy, radiotherapy, virotherapy, targeted therapies, vaccines, and other immune modulators.

One troubling and persistent issue during ICB therapy has been a high incident of immune-related toxicities, termed immune-related adverse events (irAEs). These toxicities are very frequent, occurring in 90% of patients treated with anti-CTLA-4 mAb

and 70% of patients treated with an anti-PD-1 pathway mAb.[25] While the majority of irAEs are low grade (grades 1-2) and not life threatening, there is a high prevalence of severe irAEs (grades 3-4) that can require hospitalization at 10-42% in patients treated with anti-CTLA-4 mAb and 1-20% of patients treated with an anti-PD-1 pathway mAb. These severe irAEs occur at a significantly higher rate in combination therapy, approximately 40-60% of melanoma patients reported grade 3-4 adverse events in combination ipilimumab (anti-CTLA-4) and nivolumab (anti-PD-1 therapy) (Figure 1-3).[26,27] High grade irAEs are rarely fatal, 0.64% in ipilimumab and 0.1-0.3% in nivolumab, but these events will likely increase as more patients are moved to combination therapies.[28] As therapy design moves more towards combination treatments, significant efforts will have to be made to find combinations that limit irAEs while still achieving increased response rates.

As these therapies have advanced in clinical settings, incidences of adaptive or acquired resistance to therapy have also risen. Studies have shown that both tumor-cell-intrinsic and -extrinsic factors contribute to mechanisms of acquired resistance to therapy.[29] Tumor-cell-intrinsic mechanisms of resistance include expression or repression of certain genes and pathways in tumor cells that prevent immune cell infiltration or function within the tumor microenvironment. Tumor-cell-extrinsic mechanisms of resistance involve components other than tumor cells within the microenvironment including T regulatory (Treg) cells, myeloid derived suppressor cells, M2 macrophages, and other inhibitory immune checkpoints, which may all contribute to inhibition of anti-tumor immune responses. It has become clear that approximately one fourth to one third of metastatic melanoma patients that initially respond to ICB mAb therapy will relapse over time, even despite receiving continued therapy.[30] Continued

research into mechanisms of acquired resistance underscores an unmet need to expand the immunotherapeutic toolkit in order to combat complications that arise during therapy.

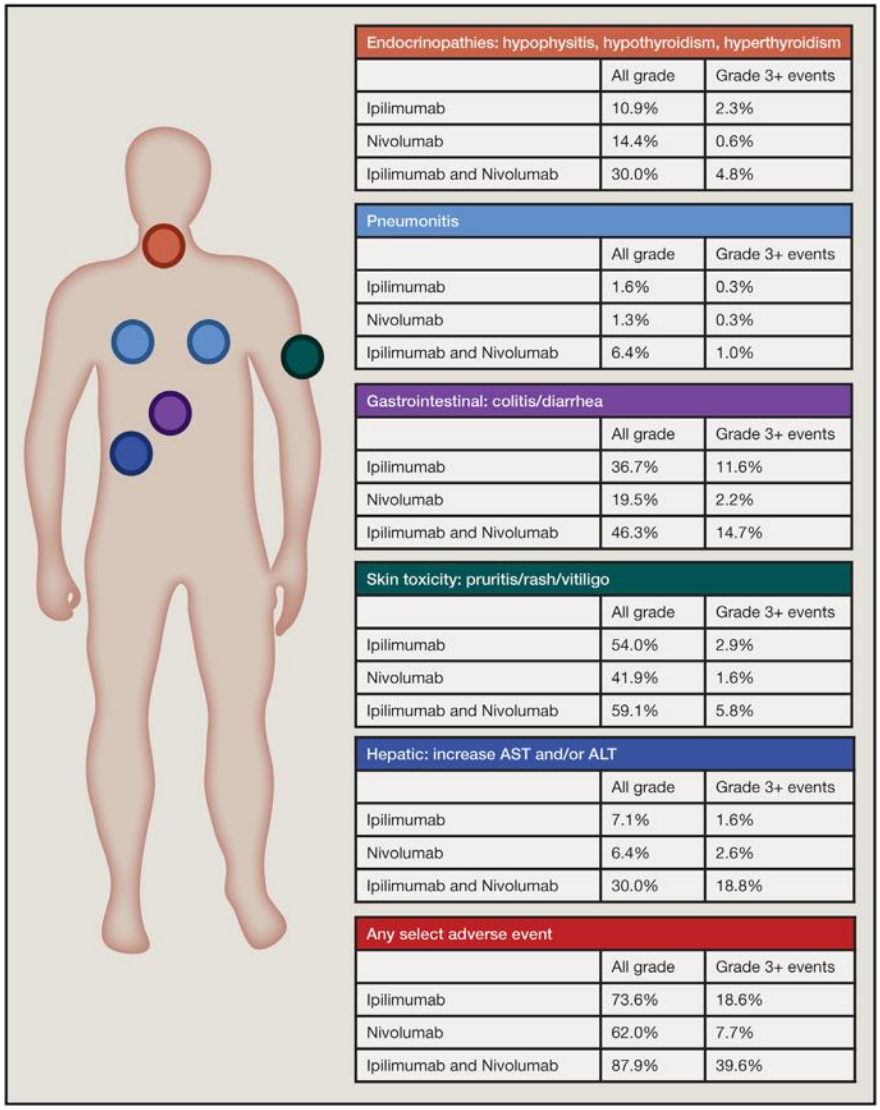

Endocrinopathies: hypophysitis, hypothyroidism, hyperthyroidism		
	All grade	Grade 3+ events
Ipilimumab	10.9%	2.3%
Nivolumab	14.4%	0.6%
Ipilimumab and Nivolumab	30.0%	4.8%

Pneumonitis		
	All grade	Grade 3+ events
Ipilimumab	1.6%	0.3%
Nivolumab	1.3%	0.3%
Ipilimumab and Nivolumab	6.4%	1.0%

Gastrointestinal: colitis/diarrhea		
	All grade	Grade 3+ events
Ipilimumab	36.7%	11.6%
Nivolumab	19.5%	2.2%
Ipilimumab and Nivolumab	46.3%	14.7%

Skin toxicity: pruritis/rash/vitiligo		
	All grade	Grade 3+ events
Ipilimumab	54.0%	2.9%
Nivolumab	41.9%	1.6%
Ipilimumab and Nivolumab	59.1%	5.8%

Hepatic: increase AST and/or ALT		
	All grade	Grade 3+ events
Ipilimumab	7.1%	1.6%
Nivolumab	6.4%	2.6%
Ipilimumab and Nivolumab	30.0%	18.8%

Any select adverse event		
	All grade	Grade 3+ events
Ipilimumab	73.6%	18.6%
Nivolumab	62.0%	7.7%
Ipilimumab and Nivolumab	87.9%	39.6%

Figure 1-3. Immune-related toxicities in patients treated with antibody immune checkpoint blockade single agent and combination therapy.
Selected immune-related toxicities in melanoma patients that were treated with ipilimumab (anti-CTLA-4), nivolumab (anti-PD-1), or a combination of both antibodies compared by frequency and severity. Adapted from Callahan et al., 2016.[26]

1.3 Second-generation immunotherapeutic targets: TIGIT and TIM-3.

The immunotherapeutic successes in targeting the CTLA-4 and PD-1 pathways have prompted investigation into new immune checkpoint receptors in order to broaden the therapeutic repertoire. If CTLA-4 and PD-1 are to be considered first-generation

immune checkpoint targets, there is a growing group of second-generation immune checkpoint targets that includes T cell immunoreceptor with Ig and ITIM domains (TIGIT) and T cell immunoglobulin and mucin-domain containing-3 (TIM-3).

TIGIT (also known as VSIG9 and VSTM3) is a member of the poliovirus receptor (PVR)/nectin family, a subset of the immunoglobulin superfamily. The expression of TIGIT is limited to lymphocytes and is primarily expressed on effector and regulatory CD4+ T cells, follicular helper CD4+ T cells, effector CD8+ T cells, and natural killer (NK) cells.[31–36] The study of TIGIT across different lymphocytes has suggested TIGIT contributes to the regulation of several steps of the cancer immunity cycle including early innate immune cell cytotoxicity, T cell activation and priming, and late adaptive immune cell cytotoxicity.

Promising pre-clinical studies including anti-TIGIT agents have prompted several clinical trials involving therapeutic TIGIT antibodies both in monotherapy and in combination therapies. Currently, 16 active clinical trials are ongoing testing anti-TIGIT agents across multiple conditions including non-small cell lung cancer (NSCLC), small cell lung cancer, multiple myeloma, cervical and ovarian cancer, esophageal squamous cell carcinoma, glioblastoma, and solid and metastatic tumors. One trial with the anti-TIGIT therapeutic tiragolumab (Roche) used in combination with anti-PD-L1 atezolizumab to treat NSCLC patients resulted in the doubling of objective response rates, 31.3%, in combination compared to monotherapy with atezolizumab, 16.2%.[37] Combination treatment also resulted in adverse events in 80.6% of the patient population with high grade adverse events in 14.9% of patients. This safety profile was considered acceptable for the FDA and they granted tiragolumab with a Breakthrough Therapy Designation

designed to accelerate the development and review of therapies for life-threatening conditions with preliminary evidence that demonstrates an improvement over existing therapy. Tiragolumab appears poised to become the first FDA-approved anti-TIGIT therapeutic in the near future.

TIM-3 (also known as HAVCR2) is a type I trans-membrane protein belonging to the TIM family and immunoglobulin superfamily that was originally discovered in an effort to identify novel cell surface molecules that would serve as a biomarker for interferon gamma (IFN-g)-producing type 1 helper (Th1) and cytotoxic T cells.[38] TIM-3 was found to play a key role in inhibiting Th1 response and the expression of cytokines such as TNF and IFN-g. In addition to its expression on T cells, TIM-3 has been identified on DC cells, NK cells, monocytes, and Treg cells. High levels of TIM-3 expression correlate with suppression of T cell responses and T cell dysfunction.[16] TIM-3 has been implicated as a checkpoint receptor in tumor immunity by regulating T cell exhaustion in TILs from both human and mouse tumors.[39,40]

TIM-3 expression on exhausted T cells usually is associated with PD-1 expression and marks “deeply” exhausted T cells from both human and animal studies, supporting the functional correlation between TIM-3 and PD-1 during the development of T cell exhaustion.[40–42] The combination of TIM-3 blockade with PD-1 blockade is remarkably more effective in these models, leading to greater tumor regression with higher frequency than with blockade of either TIM-3 or PD-1 pathway alone.[40,43] Furthermore, upregulation of TIM-3 has also been implicated in the adaptive resistance to PD-1 mAb blockade in both mouse models and patients.[44] Consistent with a key regulatory role in both innate and adaptive immune responses, blockade of TIM-3 signaling with mAbs in preclinical

tumor models exhibited therapeutic benefit in cancer immunotherapy. TIM-3 has emerged as a target for numerous mAb-based therapeutics that are currently under clinical development both as a single agent and in combination therapies.[45]

1.4 Rationale for small molecule inhibitors of immune checkpoints.

Several ICB mAbs have been approved by the FDA for clinical use that offer substantial anti-tumor benefits both as single agents and for use in combination therapies. These mAbs have helped to revolutionize how clinicians can combat cancer, however, like all cancer treatments, there are drawbacks and complications that arise when using these agents.[46] Several drawbacks inherent to mAbs can be attributed to their physical and pharmaceutical properties. Firstly, deep tissue penetration of mAbs is challenging to achieve due to their large size (~150 kDa) and may contribute to current mAb therapeutic having sub-optimal efficacy.[47] Indeed, immune checkpoint expressing T cells are found to have infiltrated the solid tissues of tumors.[48] If a mAb therapeutic targeting ICB cannot physically reach the site of target engagement, this will subsequently lead to a sub-optimal response. Secondly, the half-lives of current clinically used ICB mAbs are on the order of 2-4 weeks.[49] Moreover, it has been found that these agents have such high affinity and avidity for their target that they can stay engaged with their target receptor for more than 2 months after the antibodies have cleared circulation.[50,51] This long-term exposure will lead to long periods of inhibited immune checkpoint signaling pathways and can potentially result in off-target T cell activation and increased autoimmunity. Clinical data has suggested that long-term ICB contributes to incidences of irAEs.[49] When designing new ICB therapeutics, efforts should be made to maximize tissue penetration and mitigate potential irAEs that arise from prolonged target engagement.

Another inherent problem with ICB mAbs is the presence of the Fc chain that interacts with Fc receptors and can lead to off-target immune responses in macrophages and NK cells. These interactions can lead to unwanted immunogenicity that induce anti-drug antibodies (ADA).[52–54] ADA can induce reactions at the site administration or alter the pharmacokinetics of the ICB mAbs affecting its clearance and overall treatment efficacy by neutralizing the activity of the drug through neutralizing antibodies (NAb).[55] In anti-CTLA-4 and anti-PD-1 combination therapy, reported incidences of ADA were 24-38% and NAb were 1-5% following mAb administration to patients with advanced solid tumors.[56]

In addition to unwanted immunogenicity, the expense of using ICB mAbs as single agents and in combination is a significant concern. The production of antibodies is complex and they are, therefore, associated with higher production costs and more expensive to alternative therapeutics. FDA-approved pembrolizumab (anti-PD-1 antibody) costs $150,000 per patient per year and a combination of pembrolizumab with ipilimumab (anti-CTLA-4 antibody) costs $254,000 per patient per year.[57] This significant expense places a large burden on patients and health care systems worldwide. In fact, nivolumab (anti-PD-1 antibody) has been rejected for UK patients with head and neck cancer because the price is too high.[58] Alternative therapeutics with a lower cost of production could reduce the overall expense of therapy and, thereby, make these revolutionizing therapeutics more widely available to less advantaged patients throughout the world.

A viable alternative therapeutic approach to ICB is through the use of small molecules that inhibit co-inhibitory immune checkpoint proteins with their cognate

receptors. Small molecule inhibitors of these pathways could be more cost-effective, have less unwanted immunogenicity, have tunable pharmacokinetic (PK) and pharmacodynamic (PD) profiles, and offer deeper tissue penetration compared to their antibody counterparts. Importantly, small molecules are more readily modulated such that they offer potential for designing compounds with shorter half-lives along with enhanced tissue penetration and biodistribution. Small molecule inhibitors can be designed with PK/PD profiles that allow for patient-dependent dosing strategies to achieve maximum efficacy while minimizing potential irAEs. Patients experiencing severe irAEs could be simply discontinue small molecule treatment allowing for the quick and full clearance of the drug and a return to immune homeostasis. As more patients are moved to combination therapies, clinicians expect the number of severe irAEs to rise and ICB through small molecules will allow for more controllable therapeutic windows potentially resulting in more successful therapy.

Reports of small molecule inhibitors of immune checkpoint proteins have been limited to date despite the potential advantages discussed above.[59] Immune checkpoint proteins are predicted to be challenging targets for small molecules because of their lack of deep hydrophobic pockets and reliance on protein-protein interaction (PPI) active sites that require large surface areas to interact with their ligands. Due to the large and plastic surface of PPIs, traditional drug discovery methods such as high throughput screening have been ineffective in developing drug candidates. Consistent with this notion, no small molecule inhibitors have entered clinical trials for TIGIT or TIM-3. A peptidomimetic modulator (CA-327) reported by Curis Inc. to target both TIM-3 and PD-L1 is in preclinical development. The reported therapeutic results mimic those of FDA-approved monoclonal

antibodies to some extent while overcoming the limitations of the high production costs and adverse effects of the latter. However, no conclusive biophysical evidence proving the binding to TIM-3 has ever been presented. A similar compound in clinical trials, CA-170, that targets both PD-L1 and VISTA has come under recent scrutiny. A biophysical testing of CA-170 via NMR and homogenous time resolved FRET showed no direct binding between CA-170 and PD-L1 or disruption of PD-L1 and PD-1 by CA-170.[60] Despite these findings, CA-170 has shown promising results in preclinical trials questioning the true mechanism of action. A similar review of CA-327's interaction with TIM-3 is warranted.

Our lab has previously endeavored to develop small molecule inhibitors for the immune checkpoint targets CTLA-4, PD-1, and PD-L1. Dr. Evan Perry's dissertation outlines his efforts to discover and develop compounds capable of inhibiting these proteins.[61] Fragment screening of CTLA-4 and PD-1 identified few tractable fragment hits and both proteins were ultimately considered to be undruggable by small molecules. However, fragments were identified that bind to PD-L1 and were capable of displacing PD-1. Structural information of binding was obtained and used to facilitate structure-based design to elaborate hits into more potent analogs.[62] That work both highlights the difficulty in developing inhibitors for immune checkpoint proteins and the potential for success. There remains and unmet need for the development of novel small molecule inhibitors of TIGIT and TIM-3.

1.5 Fragment-based drug discovery.

As discussed above, protein-protein interactions (PPIs) are difficult to develop small molecule ligands for by traditional methods because of large, flat surface areas of

interaction. Many validated cancer drug targets have PPIs with their cognate ligands necessitating non-traditional drug discovery methods to probe the druggability of these challenging targets. Fragment-based drug discovery (FBDD) methods in combination with structure-based designed was first introduced by Stephen Fesik and colleagues at Abbott labs as a highly effective method to develop small molecule ligands for difficult to target proteins.[63] FBDD has led to the design of several high-affinity ligands for proteins once thought to be "undruggable."[64]

FBDD consists of screening libraries of low molecular weight "fragments" (<300 kDa) that adhere to an altered Lapinski's rule of five in which five is replaced with 3 for direct binding to protein targets. These fragments are smaller and less complex than molecules screened in traditional high throughput screening (HTS) campaigns. While this lack of complexity often yields lower-affinity hits, smaller fragment screening libraries can cover more chemical space than the large libraries used in traditional HTS.[65] Although fragment hits are generally low-affinity, they often make high quality interactions with the target resulting in a higher starting ligand efficiency compared to HTS hits that make numerous suboptimal interactions within a binding site (Figure 1-4A). FBDD screens can identify chemotypes that bind to shallow binding pockets that would otherwise be missed by HTS campaigns due to numerous potential steric clashes of elaborated compounds (Figure 1-4B). [66] Generally, several rounds of SAR are required to optimize compound binding from a starting milli- or micromolar fragment hit to a nano- or picomolar binding drug-like compound.

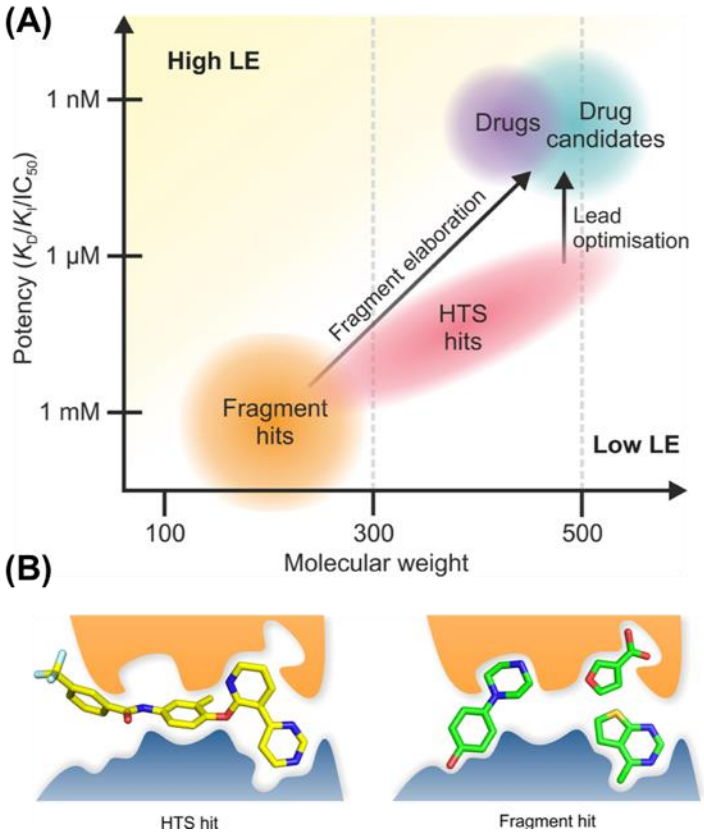

Figure 1-4. Comparing hits from conventional HTS and FBDD approaches.
(A) Comparison of molecular mass vs potency of leads developed from conventional HTS and FBDD approaches. The dashed lines show Lipinski's Rule of Five 500 molecular weight cutoff and the Rule of Three 300 molecular weight limit. (B) HTS hits may bind by virtue of numerous suboptimal interactions. By contrast, fragment hits are more ligand efficient and involve fewer but more optimized interactions. Adapted from Scott et al., 2012.[66]

Structural information of fragment binding can be utilized in several different ways to aid the discovery of a high-affinity compound. For example, if two fragments are found to bind adjacent sites within a close proximity, those fragments can be covalently linked to generate a compound with higher binding affinity. Indeed, the predicted binding affinity of a two fragment linked compound is equal to the product of the K_d of the first fragment (A) and the K_d of the second fragment (B) multiplied by a linking constant (L):[63]

$$K_{\mathrm{d}}\mathrm{AB} = K_{\mathrm{d}}\mathrm{A} \times K_{\mathrm{d}}\mathrm{B} \times \mathrm{L}$$

Adjacent site-binding fragments can be found through the initial screen or through second site screening, where a saturated protein-fragment complex undergoes a second

fragment screen to identify additional binding fragments. Alternatively, fragments that bind within the same general binding site can be merged together by analyzing the interactions made by different fragments and mimicking those interactions in a merged compound that shares those interacting features around a binding-site admissible core. Iterative optimizations through fragment linking, merging, or growing to improve binding affinity are aided by structural information from X-ray crystallography or NMR and molecular modeling to generate high-affinity lead compounds (Figure 1-5).

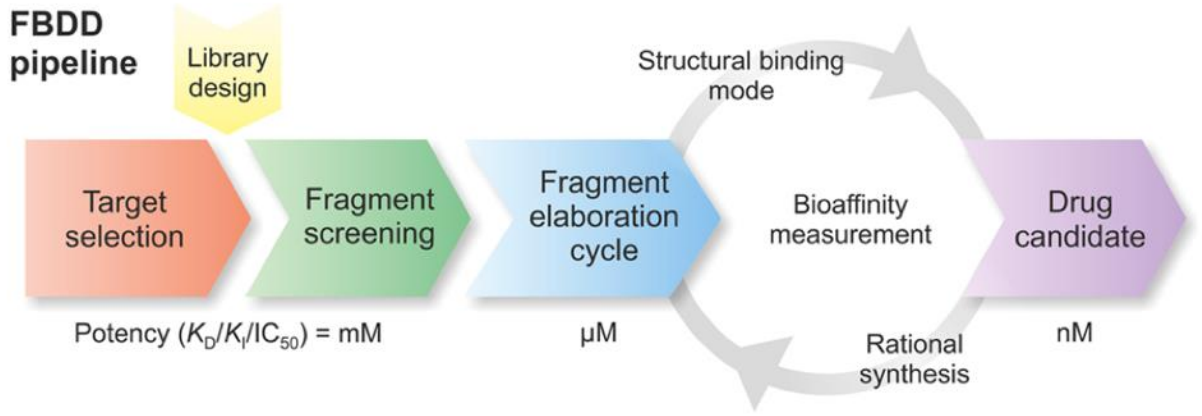

Figure 1-5. General workflow of the FBDD approach.
The iterative cycle of design, binding mode determination, and affinity measurement to incrementally improve potency and biophysical properties is shown. Adapted from Scott et al., 2012.[66]

FBDD requires a reliable assay to observe the direct binding of low-affinity fragments (K_d = 100 μM to 5 mM). Compared to other biophysical methods, protein-observed NMR is arguably the most robust method for conducting fragment-based screens.[67] Protein-observed NMR utilizes uniformly ^{15}N or ^{13}C labeled protein to obtain $^{1}H/^{15}N$ or $^{1}H/^{13}C$ HSQC spectra of the protein of interest in the presence and absence of fragment mixtures. The resonance peaks observed in HSQC spectra correspond to a specific amino acid backbone amide NH of the protein. Ligand binding changes the chemical environment that a binding-site amino acid amide NH observes resulting in chemical shift perturbations in binding-site resonance peaks (Figure 1-6A). The chemical

shift changes can be easily observed by overlay of the HSQCs with and without ligand (Figure 1-6B). The advantages of protein-observed NMR fragment screening include the observation of direct ligand binding resulting in few false positives, the ability to measure binding affinity without the need of a secondary assay, the ability to distinguish between fragments that bind at different binding sites with different chemical shift patterns, and the ability to identify protein binding sites if the backbone peak resonances have been assigned.[67] Advances in NMR technologies have allowed for rapid acquisition of $^{1}H/^{15}N$ HMQC spectra coupled with automated sample changers making fragment screening by NMR a medium throughput assay.[68]

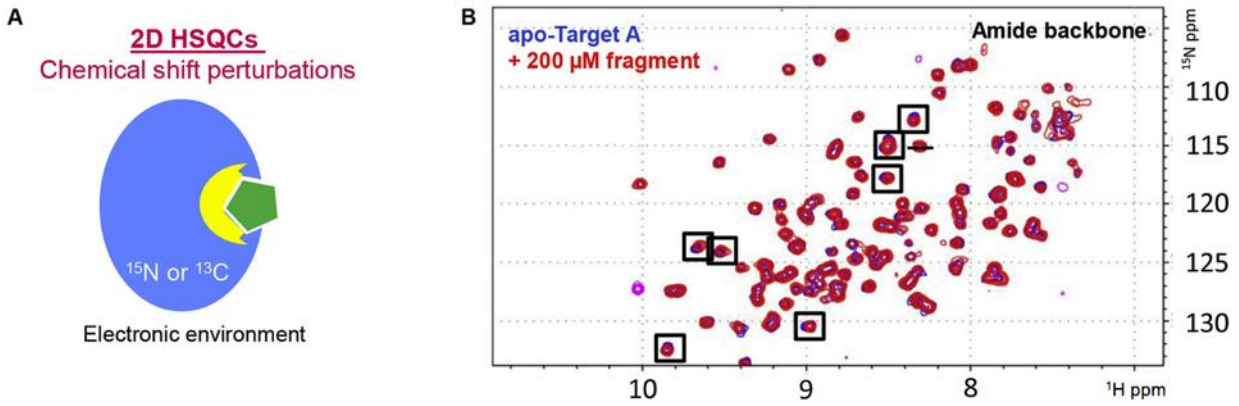

Figure 1-6. Fragment screening by protein-observed NMR.
(A) Cartoon depiction of target-observed NMR binding assays, where the portion of the target colored yellow will experience a change in chemical environment upon binding of a fragment hit, resulting in chemical shift perturbations. (B) Two-dimensional $^{1}H/^{15}N$ HSQCs detect binding of weak fragment hits to protein target A and allow for binding site mapping when resonance assignments are known. The boxed backbone resonances indicate residues that are perturbed upon binding. Adapted from Harner et al., 2017.[69]

Computational methods have been used to assess the druggability of a protein target by algorithmically analyzing a protein structure to identify potential small molecule "hot spots."[70,71] These methods usually assume the protein structure is rigid and fail to account for protein dynamics or ligand-induced conformational changes. More direct experimental assessments of a target's druggability are often warranted. The success of a protein- observed NMR fragment screening has a high correlation with the ability to

identify high-affinity protein ligands. Experimental evidence suggests protein targets with fragment hit rates > 0.1% are likely to be druggable targets.[72,73] Thus, NMR fragment screens can be used to experimentally assess protein druggability and aid in important decisions about the prioritization of targets in a drug discovery program.

1.6 Scope of this Thesis

In the following chapters, I describe my efforts to develop novel small molecule inhibitors of the immune checkpoint proteins TIGIT and TIM-3 using fragment-based drug discovery methods and structure-based design for analog optimization. In chapter 2, I describe expression, purification, and screening results of a fragment-based screen of TIGIT. In chapter 3, I describe the results of an unbiased fragment-screen of TIM-3, hit validation and optimization of fragment hits and subsequent analogs by structure-based design. In chapter 4, I describe the development of a fragment-based screen directed at targeting the FG-CC' active site of TIM-3, the results of the fragment screen, and hit validation. In chapter 5, I summarize all results and discuss the future direction for the development of small molecule inhibitors against these important yet challenging targets.

Chapter 2 – Fragment Screen of T cell immunoreceptor with Ig and ITIM domains (TIGIT).

2.1 Introduction

2.1.1 *TIGIT is a validated immunotherapeutic target.*

T cell immunoreceptor with Ig and ITIM domains (TIGIT) is a cell-surface expressed immune checkpoint co-inhibitory protein composed of an extracellular IgV domain, a type 1 transmembrane region, and a cytoplasmic tail containing an immunoreceptor tyrosine-based inhibitory motif (ITIM) and an immunoglobulin tail tyrosine (ITT)-like motif which are highly conserved between mouse and human.[31–33,74,75] The TIGIT ligands PVR and CD112 are widely expressed on tumor cells. TIGIT-deficient mice have been shown to significantly delay tumor growth in two different tumor models, confirming TIGIT's role in negatively regulating anti-tumor responses.[76] Within the tumor microenvironment, TIGIT is highly expressed on human and murine tumor-infiltrating leukocytes (TILs) including CD8+ T cells, natural killer (NK) cells, and regulatory T (Treg) cells across a broad range of tumors.[35,76,77] TIGIT expressing $CD8^+$ TILs have also been shown to express immune checkpoint inhibitors PD-1, TIM-3, and LAG-3 resulting in a highly dysfunctional phenotype among TILs in murine tumors.[76] Furthermore, the expression of TIGIT is relatively poor in the peripheral lymphoid organs of tumor-bearing mice but highly enriched in tumor tissue, indicating a specialized role for TIGIT in regulating immune responses in tumor tissue.[76] This anatomically distinct expression could underlie the lack of autoimmunity in TIGIT-deficient mice and would be expected to translate into reduced occurrence of irAEs in human patients.

Recent monoclonal antibody blockade studies indicate that TIGIT blockade has synergistic immune activating effects with blockade of the PD-1/PD-L1 pathway. In $CD8^+$ TILs from melanoma patients, co-blockade of TIGIT and PD-1 improved proliferation, cytokine production, and degranulation over mono-blockade.[77] Similarly, co-blockade of TIGIT with PD-L1 showed synergistic effects in the murine CT26 tumor model, leading to enhanced TIL effector function and reversal of $CD8^+$ T cell exhaustion. The combined treatment in mice resulted in complete tumor regression and induced tumor-antigen specific protective memory responses.[35] TIGIT also synergizes with TIM-3 in impairing protective anti-tumor response further indicating that TIGIT and other co-inhibitory checkpoint proteins additively dampen effector T cell responses and promote T cell dysfunction.[76] Tumor-associated $TIGIT^+$ Treg cells exhibit a highly suppressive phenotype and have been shown to play a key role in driving suppression in the tumor environment.[76] Thus, TIGIT can suppress anti-tumor immunity by multiple mechanisms that which will be further discussed in the next section.

2.1.2 *TIGIT negatively regulates several steps in the cancer immunity cycle.*

NK cells are thought to be most important in the early stages of cancer elimination and in preventing metastases, but also as cytolytic effector cells as they participate in the release of tumor antigens. TIGIT signaling has been best studied on NK cells where it can signal through its ITIM as an immune-inhibiting receptor.[74] Ligation of cognate receptor PVR on target cells results in diminished NK cell effector function.[78–80] NK cells from TIGIT-deficient mice produced more interferon gamma (IFN-g) in the presence of PVR-expressing target cells, whereas TIGIT-transgenic NK cells produced less IFN-g than WT cells. TIGIT signaling leads to a strong reduction of NK cytotoxicity, granule

polarization, and cytokine secretion in NK cells.[74,79,80] These data suggest that TIGIT-mediated regulation of NK cell function impacts step 1 of the cancer immunity cycle by inhibiting the cytotoxicity of innate immune NK cells (Figure 2-1).

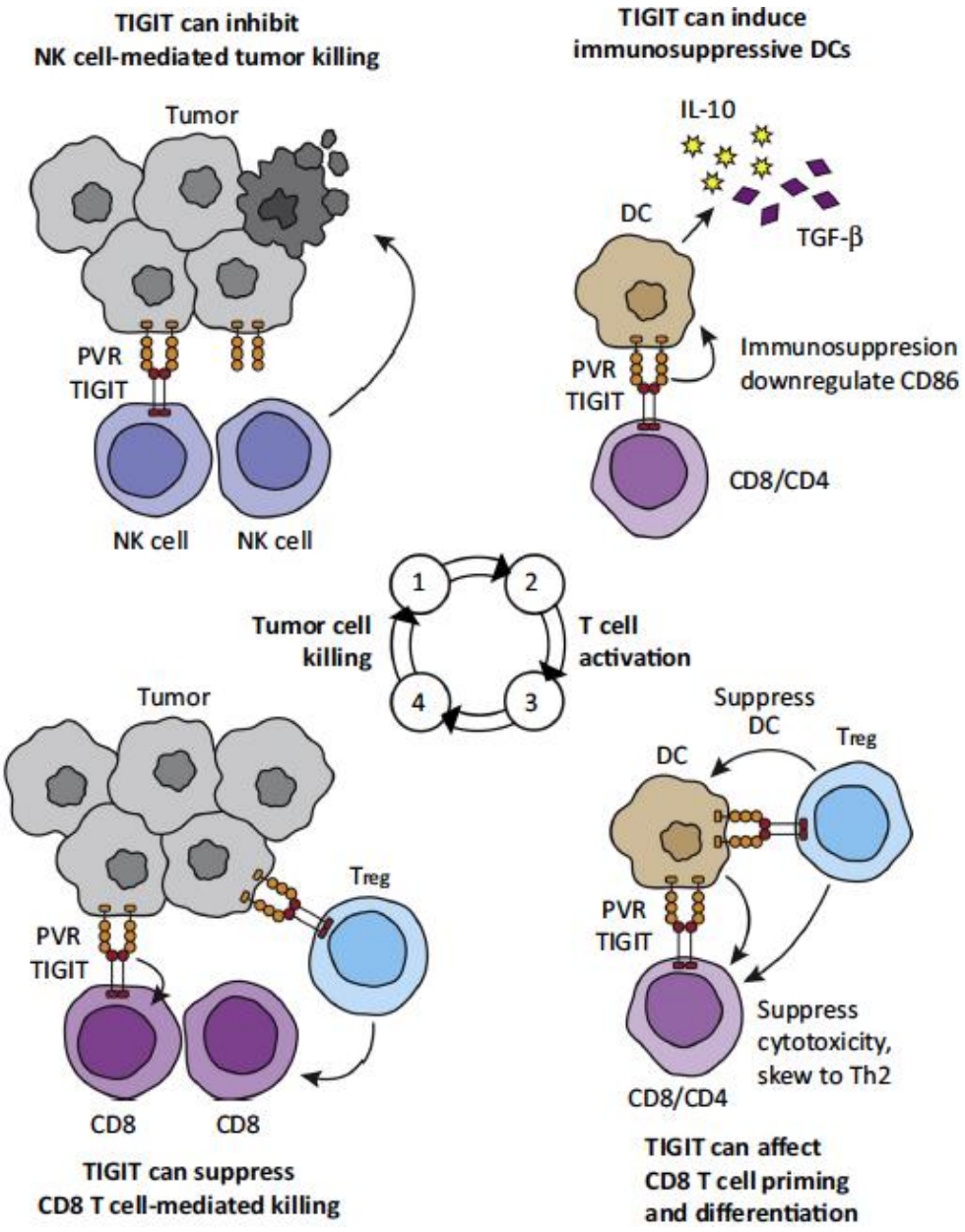

Figure 2-1. TIGIT inhibits the Cancer Immunity Cycle at several steps.
TIGIT can inhibit immune cells at multiple steps in the cancer immunity cycle. Starting with step 1, TIGIT can inhibit NK cell effector function preventing initial tumor cell death and release of cancer cell antigens. At step 2, TIGIT on T cells can suppress dendritic cell co-stimulatory abilities, leading to reduced cancer antigen presentation and increased anti-inflammatory cytokines such as IL-10. At step 3, TIGIT+ Tregs or PVR-stimulated myeloid cells can suppress CD8+ T cell effector function or skew CD4+ T cell polarization. At the final step in the cycle, TIGIT can directly inhibit CD8+ T cell effector function, or TIGIT+ Tregs can inhibit CD8+ T cells and prevent the elimination of cancer cells. Adapted from Manieri et al., 2017.[81]

Cancer cells can evade immune responses as a result of an immunosuppressive tumor microenvironment (TME). TIGIT induces dendritic cells (DCs) to acquire a tolerogenic phenotype via ligation of PVR, resulting in elevated immunosuppressive IL-10 expression and concomitant reduction in pro-inflammatory IL-12.[31] IL-10 is an immunosuppressive cytokine that acts on T cells directly and prevents antigen-presenting cells from upregulating molecules involved in antigen presentation, thereby suppressing T cell proliferation and elaboration of effector cytokines such as IFN-g. TIGIT may also affect cytokine balance by shifting the immune response towards one dominated by IL-10 by skewing T cell differentiation away from pro-inflammatory Th1 and Th17 phenotypes and towards Th2.[34,82,83] These data suggest TIGIT can modulate the TME and its immunosuppressive properties affect step 2 of the cancer immunity cycle because a pro-inflammatory environment is needed to properly activate DCs (Figure 2-1).

Regulatory T cells (Tregs) can influence multiple steps of the cancer immunity cycle, including the suppression of effector T cell activation and cytotoxicity (Figure 2-1). TIGIT is constitutively expressed by most Tregs and has been shown to play an important role in the function and maintenance of these cells.[36,84] $TIGIT^+$ Tregs have been shown to be more immunosuppressive than $TIGIT^-$ Tregs by several groups.[36,76,84] Furthermore, $TIGIT^+$ Tregs can suppress pro-inflammatory Th1 and Th17 responses but not anti-inflammatory Th2 responses. Tregs may play an important role early in tumor development. However, it remains to be seen if anti-TIGIT therapy, once tumors are established, works by acting on Tregs, CD8+ T cells, or both.

Generating CD8+ T cell antitumor responses is a primary goal for most immunotherapies because it is thought that CD8+ TIL activation is necessary to fully reject

tumors. TIGIT is an important inhibitory molecule found on CD8+ TILs in several different human solid tumors, including lung, colon, breast, uterine, renal, and metastatic melanoma.[35] This expression was also found to be tightly associated with PD-1 expression.[35,77] TIGIT inhibits productive T cell activation, proliferation, and acquisition of effector functions by targeting molecules in the T cell receptor (TCR) signaling pathway. When engaged with PVR, TIGIT downregulates components and central regulators of the TCR signaling cascade such as TCRα, CD3ε, and PLCγ.[82] CD8+ TILs expressing high levels of TIGIT are dysfunctional, with reduced capacity for pro-inflammatory cytokine production, higher production of IL-10, and impaired degranulation.[76] Interestingly, this dysfunctional state is coupled with the upregulation of anti-apoptotic molecules such as BCL-xL as well as the receptors for cytokines IL-2, IL-7, and IL-15 which promote T cell survival. Therefore, TIGIT inhibits T cell activation but also contributes to the maintenance of the cells ensuring that, although functionally inactivated, they are retained for future activation.

Several anti-TIGIT studies have highlighted TIGIT's inhibitory role on CD8+ T cells in different cancer models. Combined antibody blockade of TIGIT and PD-L1 in mice led to the rejection of CT26 tumors and an increase in IFN-g+ CD8+ T cells in tumors compared to either treatment alone. Anti-TIGIT and anti-PD-1 co-blockade was also able to increase the proliferation and cytokine production of CD8+ TILs from patients with melanoma, and knockdown of TIGIT was able to restore cytokine production by CD8+ T cells from AML patients.[77,85] Furthermore, TIGIT–PVR interactions controlled melanoma-specific T cell responses during the effector phase.[86] High expression of TIGIT was found on melanoma TILs, whereas CD226 was downregulated, suggesting that there may be a

tipping point at which the inhibitory signal of TIGIT can overcome the activation signal of CD226. PVR expression levels on tumor cells also contributed to the strength of TIL responses. Collectively, these data suggest that TIGIT can modulate CD8+ T cell effector function and effect the final stage in the cancer immunity cycle (Figure 2-1).

2.1.3 *TIGIT structure and function.*

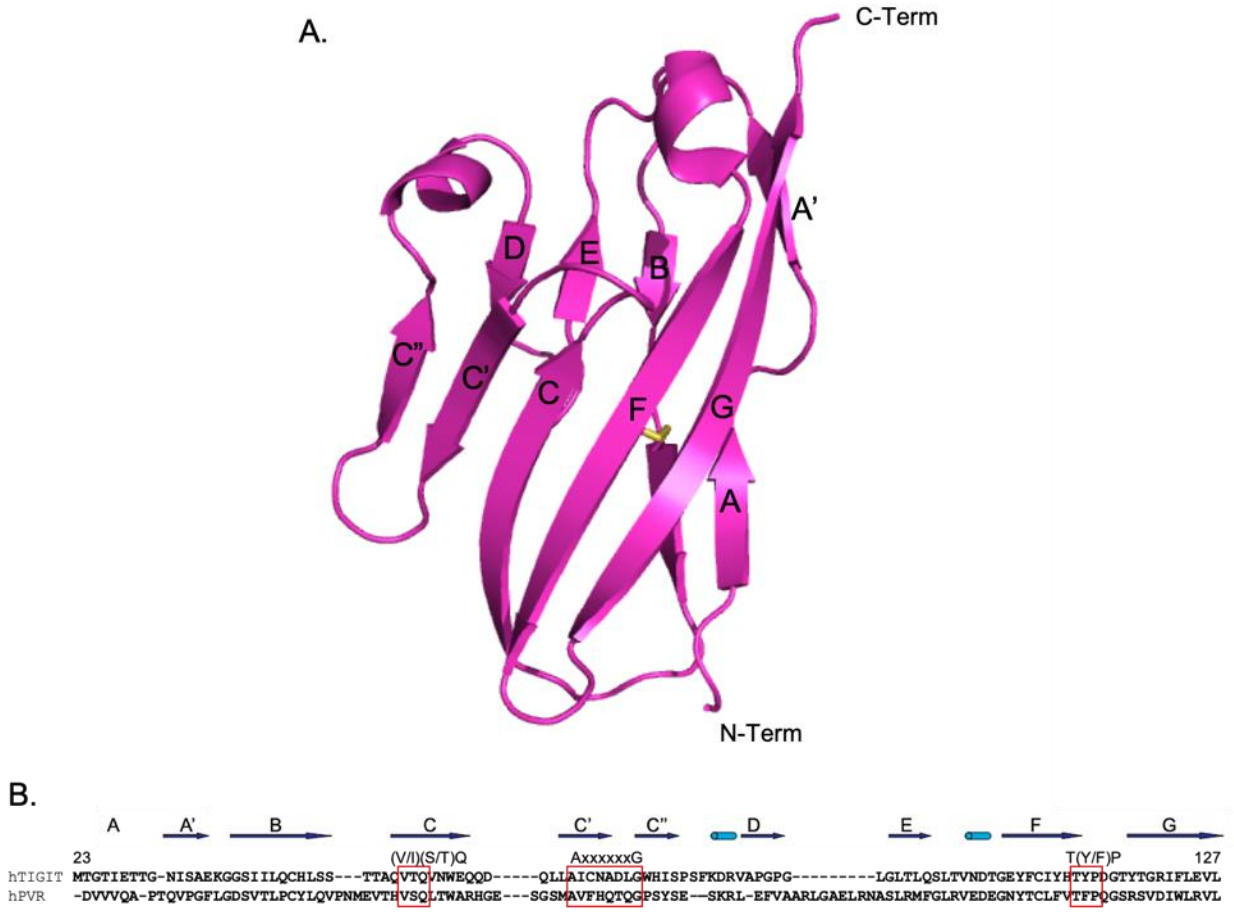

Figure 2-2. TIGIT primary and tertiary structure.
(A) 3D structure of the TIGIT IgV domain (PDB ID: 3Q0H) with labeled β-strands and internal disulfide bond shown as sticks. (B) Structure-based sequence alignment of human TIGIT and PVR IgV domains. Secondary structure elements are indicated above the aligned sequences with arrows for β-strands and cylinders for α-helices. Outlined areas indicate the PVR-related submotifs (V/I)(S/T)Q, AX_6G, and T(Y/F)P.

TIGIT is a member of immunoglobulin (Ig) superfamily and further classified as a member of the PVR/nectin family. TIGIT is composed of an extracellular Ig variable (IgV) domain, a type 1 transmembrane region, and cytoplasmic tail that contains an

immunoreceptor tyrosine-based inhibitory motif (ITIM) and an immunoglobulin tail tyrosine (ITT)-like motif which are highly conserved between mouse and human.[31–33,74,75] The TIGIT IgV interaction domain has a typical IgV β-sandwich fold with ABED strands forming one β-sheet and A'GFCC'C" strands forming the second β-sheet (Figure 2-2A). A disulfide bond between C45 of the B strand and C108 of the F strand internally stabilizes the two β-sheets.[75] The TIGIT IgV domain contains highly conserved PVR-family submotifs (V/I)(S/T)Q, AX_6G, and T(Y/F) in β-strands C, C′, and F (Figure 2-2B).

TIGIT binds to both PVR (CD155) and CD112 (PVRL2, nectin-2), which are expressed on lymphocytes and a variety of non-hematopoietic cell types, including tumor cells.[31,32,74,87,88] These ligands are shared with CD226 and CD96, and together with TIGIT form an immune-regulatory pathway in which CD226 delivers a positive co-stimulatory signal while CD96 and TIGIT deliver inhibitory signals (Figure 2-3A). Within this immune regulatory pathway, TIGIT has a higher affinity for PVR than CD226 and will outcompete CD226 in a dose-dependent manner dampening the co-stimulatory signal while providing its inhibitory signaling (Figure 2-3B).[31,32,74,81] Thus, selective inhibition of TIGIT will allow for CD226 to maintain its interaction with PVR allowing for prolonged immune activation. Furthermore, PVR contains an ITIM that is specifically activated during engagement with TIGIT leading DCs to halt IL-12p40 production and inducing IL-10 that quiets the immune response. Why PVR engagement with CD226 and CD96 does not induce a similar tolerance is not fully understood. It is known that TIGIT and PVR form a heterotetramer with a core TIGIT-TIGIT homodimer. When the TIGIT-TIGIT interface is disrupted, the phosphorylation of PVR ITIM is diminished.[75] This suggests that the ability of TIGIT

versus CD226 and CD96 to induce an immune-dampening signal in DCs could be linked to the ability to induce PVR clustering.

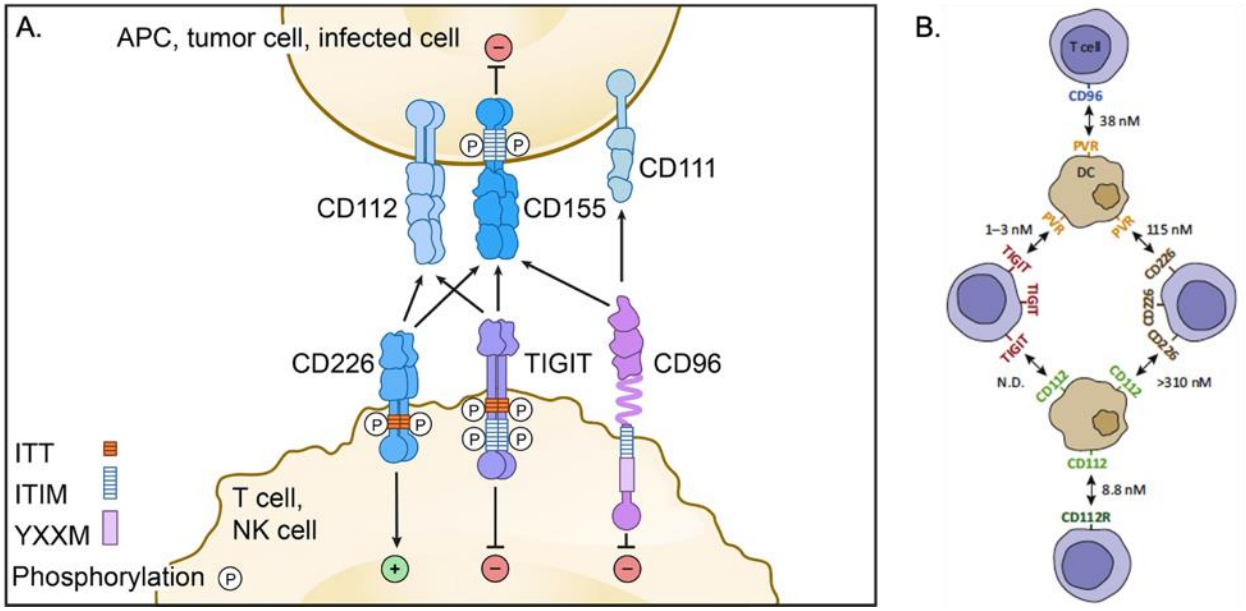

Figure 2-3. Expression and interactions of PVR family members.
(A) CD226, TIGIT, and CD96 on T cells and NK cells and their binding partners on APCs and tumor cells are depicted. CD226, TIGIT, and CD155 (PVR) interact as homodimers. Upon binding, residues in the cytoplasmic tails are phosphorylated and induce co-stimulatory or co-inhibitory signals for CD226 and TIGIT/CD96, respectively. CD155 can also deliver an inhibitory signal when engaged by TIGIT. Adapted from Dougall et al., 2017.[89] (B) The known binding affinities of human TIGIT, CD226, and CD96 to human PVR are indicated. Adapted from Manieri et al., 2016.

TIGIT signaling pathways have been best studied in NK cells. Groups have reported an essential role for phosphorylation of tyrosine in either the ITIM (Y231) or the ITT-like motif (Y225) of the cytoplasmic tail of TIGIT.[74,80] It remains unclear what the contribution of the ITIM versus ITT-like motif in mediating the inhibitory signal in human cells and further investigation of these roles is necessary. Upon engagement with PVR (CD155), phosphorylation of the ITIM is induced through Fyn and Lck and the recruitment of SH2 domain-containing inositol-5-phosphatase 1 (SHIP1) through the cytosolic adapter growth factor receptor-bound protein 2.[79] When SHIP1 is recruited to the TIGIT tail, signal transduction through the phosphoinositide 3-kinase and mitogen-activated protein kinase pathways is inhibited and results in NK cell inhibition.[79,80] Phosphorylation

of the ITT-like motif results in binding of β-arrestin 2 and recruitment of SHIP1 to limit nuclear factor-κB signaling. The combined effect of TIGIT on these signaling pathways leads to a reduction of granule polarization, cytokine secretion, and cytotoxicity in NK cells.[74,79,80]

2.1.4 *TIGIT interaction with PVR.*

The interaction between TIGIT and its cognate ligand PVR is an essential step in all mechanisms of TIGIT inhibition of the cancer immunity cycle. Disrupting this interaction would be an essential qualification for any potential TIGIT-targeted therapeutic. In the TIGIT-PVR trans-dimer complex structure, the TIGIT-PVR interface is formed by interactions between the A'GFCC′C″ β-sheets of each molecule (Figure 2-4A).[75] The FG loop of each IgV domain contacts the C′C″ loop of its partner. In total, the protein-protein interaction (PPI) buries a molecular surface area of about 1,600 $Å^2$. Additionally, the conserved sequence motifs AX_6G (residues 67-74 in TIGIT, 76-83 in PVR) in the C′C″ loop and T(F/Y)P in the FG loop (residues 112-114 in TIGIT, 127-129 in PVR) define signature lock-and-key interactions on symmetric corners of the interface that latch the two molecules together. The conserved AXXXXXZG (AX_6G) motif in the C′C″ loop creates a hydrophobic pocket with the Z residue as a lid, forming a concave "lock." The conserved aromatic "key" residue in the FG loop (Y113 in TIGIT and F128 in PVR) latches into the hydrophobic lock pocket on the opposing molecule (Figure 2-4BC).[75] These lock-and-key motifs are highly conserved in the IgV domain of nectins and comprise the distinctive PVR family motifs. The (V/I)(S/T)Q motifs in each molecule (residues 54-56 in TIGIT, 61-63 in PVR) also contribute to the intermolecular packing in the TIGIT-PVR complex. Together,

these conserved structural motifs account for most of the TIGIT-PVR interaction topography.

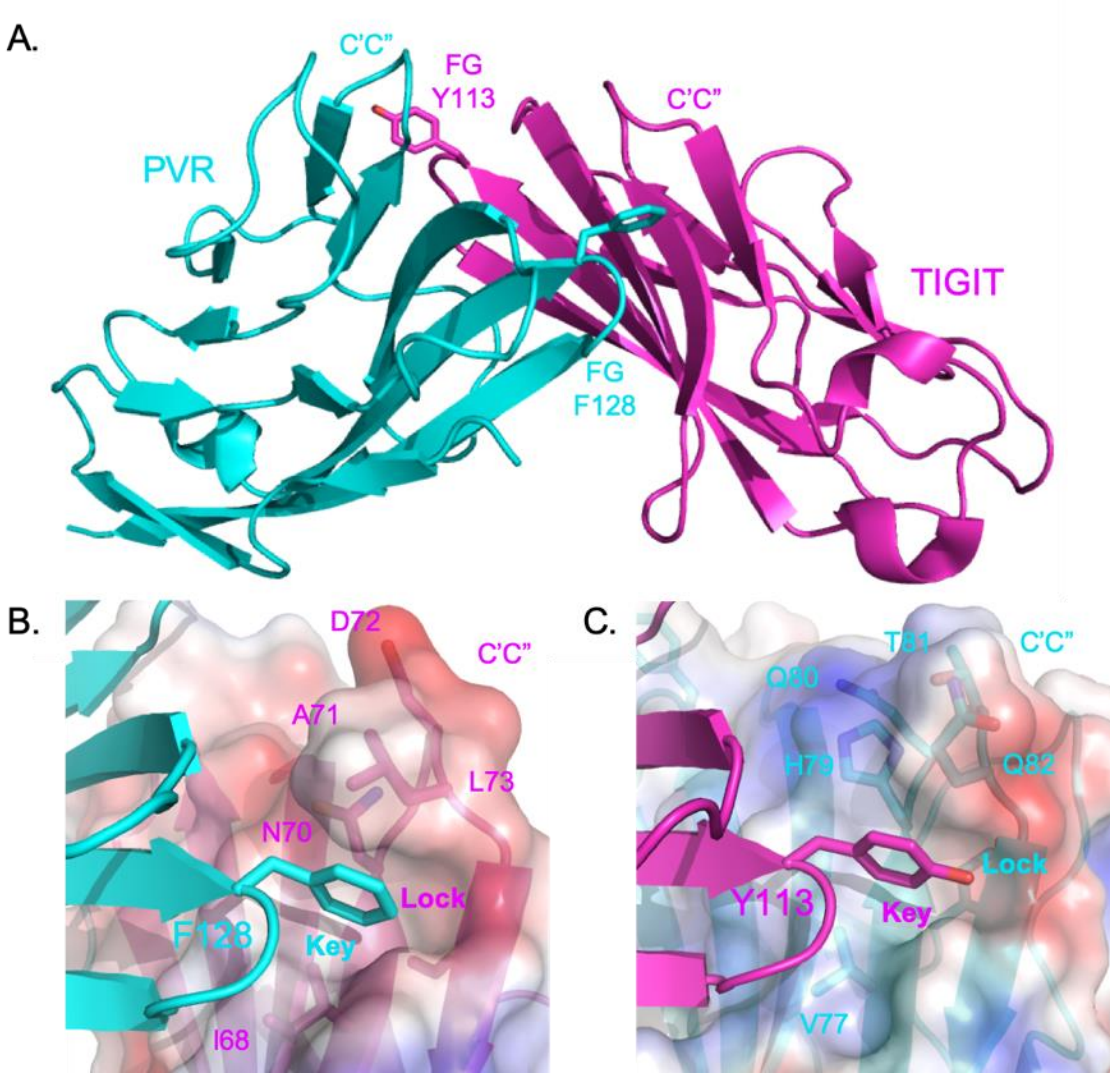

Figure 2-4. Structure of TIGIT-PVR complex.
The TIGIT-PVR interface shows a conserved lock-and-key (A) interaction between the two molecules. The "lock" is formed by the AX_6G motif, and the "key" is formed by the corresponding T(Y/F)P motif on the neighboring molecule. The "key" FG loop residues Y113 and F128 in the conserved TIGIT motif TYP and the PVR motif TFP are labeled. (B) Detailed view of the "key" formed by F128 of PVR and the lock formed by the AX_6G motif of TIGIT. (C) Detailed view of the "key" formed by Y113 of TIGIT and the lock formed by the AX_6G motif of PVR.

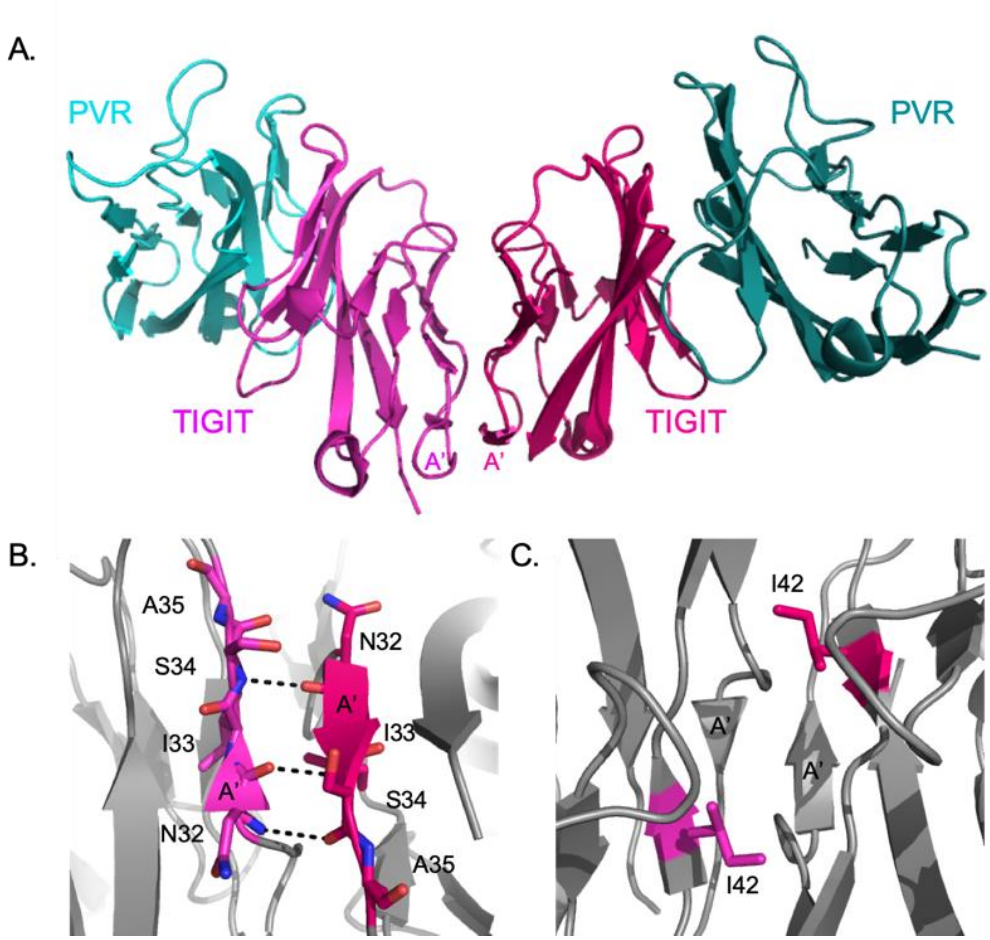

Figure 2-5. TIGIT-PVR complex has a heterotetrameric assembly with a TIGIT-TIGIT homodimer core.
(A) A core TIGIT homodimer (magentas) is flanked by two PVR (teals) molecules. (B) Detailed view of the symmetrical TIGIT-TIGIT homodimer interface, formed by main-chain interactions of the two A′ strands and (C) residue I42 at the dimer core.

The core of the TIGIT-PVR heterotetramer is formed by a symmetrical homodimer of two TIGIT molecules in which the C termini are in close proximity to each other (Figure 2-5A), suggesting the formation of a TIGIT lateral *cis*-homodimer on cells is possible.[75] The TIGIT homodimer interface buries a total molecular surface area of about 1,000 Å^2 and uses the flat surface of the ABED β-sheet on the back of the molecule. TIGIT monomers pack tightly against their neighboring protein primarily held together by main-chain interactions between A' strands (Figure 2-5B). The two A′ β-strands of adjacent molecules for an antiparallel hydrogen-bonding network. Additionally, I42 binds into a

shallow groove formed by the main-chain atoms of T29 and C45 on the opposing TIGIT monomer (Figure 2-5C). Interestingly, mutation of I42 to either alanine or aspartic acid in CHO cells resulted in reduced cell clustering and a loss of PVR phosphorylation.[75] These results suggest that robust adhesion and signaling through PVR is dependent on both TIGIT-PVR trans-interaction and TIGIT-TIGIT surface homodimerization.

The data presented above collectively suggest that inhibiting the “lock and key” TIGIT-PVR interaction can be accomplished by targeting the AX_6G “lock” motif (TIGIT residues 67-74). This shallow pocket has a hydrophobic core between C69 and G74 in which the hydrophobic F128 of PVR binds during interaction (Figure 2-6A,B). This type of binding site is ideally suited for exploration by fragment screening given the potential for central hydrophobic interaction and branching secondary interactions with the AX_6G motif residues. A potential secondary route to achieve therapeutic efficacy would be by targeting the TIGIT-TIGIT homodimer interface. In particular, I42 binds into a small hydrophobic pocket of the neighboring protein created by main-chain atoms of T29 and C45 (Figure 2-6C,D). Developing small molecule ligands for this homodimerization interface would inhibit TIGIT homodimerization, ultimately leading to reduced signaling through PVR similar to the I42 mutations discussed above. However, there is no current evidence to suggest TIGIT signaling will be affected by disrupting homodimerization. For these reasons, the development of a TIGIT inhibitor should primarily focus on the disruption of the TIGIT-PVR interface with disruption of the TIGIT homodimer as a secondary goal. Unbiased fragment-based screening of the TIGIT IgV domain can lead to hits that bind to either potential therapeutic “hotspot.” Thus, fragment screening is warranted to assess the druggability of TIGIT by small molecules.

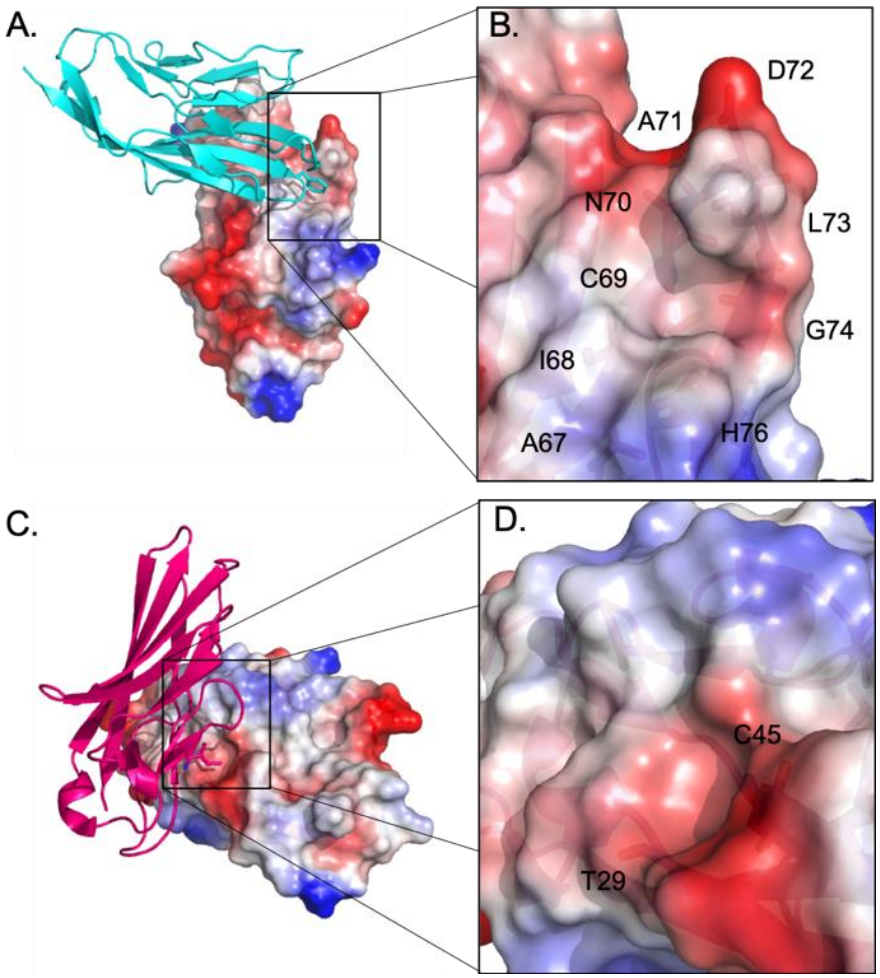

Figure 2-6. Potential therapeutic "hotspots" of the TIGIT IgV domain.
(A) TIGIT-PVR complex with the (B) residues of the AX_6G "lock" motif highlighted and labeled. (C) TIGIT-TIGIT homodimer complex with (D) I42 binding site residues highlighted and labeled. TIGIT is represented with electrostatic surface potential.

2.2 Results

2.2.1 *Expression and purification of TIGIT IgV domain.*

As discussed above, TIGIT interacts with PVR solely through its extracellular IgV domain. Thus, a TIGIT IgV domain construct was prepared for fragment screening. Previous X-ray studies revealed that C69 is solvent-exposed with the free side chain directed away from the TIGIT-PVR interface. The free cysteine was mutated to serine to avoid the formation of possible false-positive covalent adducts during fragment screening. The TIGIT C69S IgV domain (residues 23-128, MW = 11.5 kDa) was cloned into a

pET28b *E. coli* expression vector to express the protein with a thrombin cleavable N-terminal 6His tag. Uniformly ^{15}N-labeled protein required for protein-observed NMR screening was expressed from BL21 (DE3) *E. coli* raised in M9 minimal media with $^{15}NH_4Cl$ as the sole nitrogen source. TIGIT IgV protein was purified from inclusion bodies, as previously described in Stengel et al., 2012. Briefly, insoluble inclusion bodies were first purified by a series of detergent and salt washing steps using centrifugation to pellet the inclusion bodies between washes. 6His-TIGIT inclusion bodies were denatured and solubilized in 6M guanidine HCl then refolded dropwise into a TIGIT refolding buffer. 6His-TIGIT was further purified and concentrated by nickel metal affinity chromatography. Eluted protein was dialyzed and treated with thrombin to remove the 6His tag. TIGIT was separated from the 6His tag and thrombin by size exclusion chromatography resulting in pure ^{15}N-TIGIT-IgV protein with a final yield of 8 mg per liter of culture (Figure 2-7A).

A previous analysis of TIGIT homodimer formation purified in a similar manner suggests that the protein begins to favor the dimer isoform when concentrations reach 200 µM of protein.[75] Where possible during and after purification, total protein concentrations were kept below 175 µM (2.0 mg/ml) in order to ensure a population of monomeric protein. Analysis of the ^{1}H-^{15}N SOFAST HMQC spectra of purified ^{15}N-TIGIT IgV indicated a well-folded, monomeric protein suitable for fragment screening (Figure 2-7B).

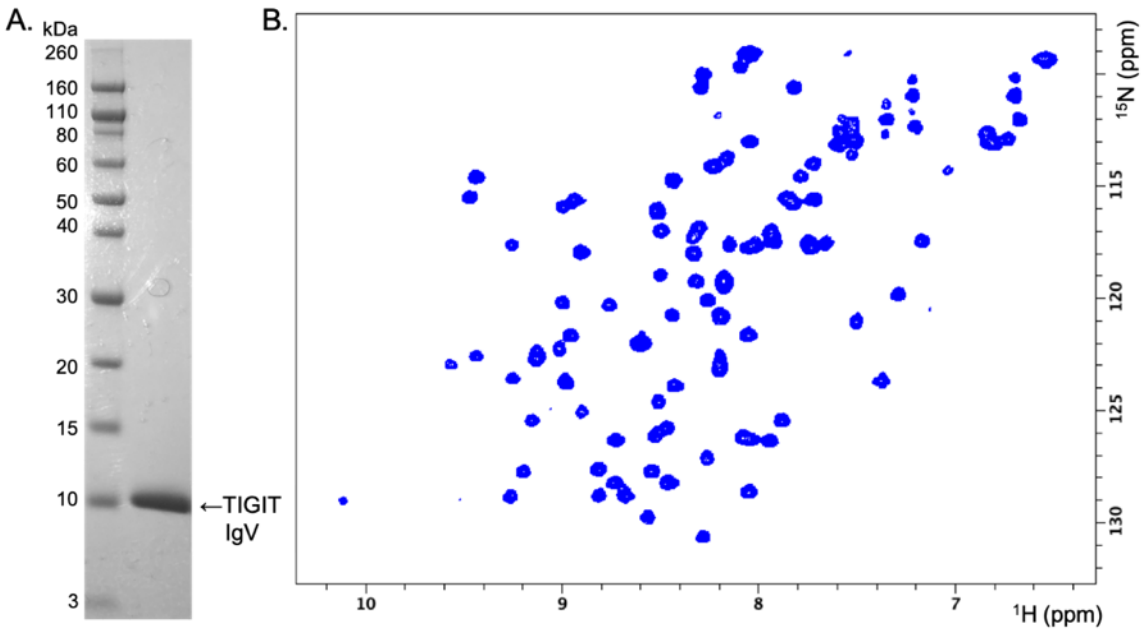

Figure 2-7. Uniformly labeled ^{15}N-TIGIT IgV domain.
(A) SDS-PAGE gel of ^{15}N-TIGIT IgV domain post-purification. (B) ^{1}H-^{15}N SOFAST HMQC spectra of purified ^{15}N-TIGIT IgV indicating a well-folded protein suitable for fragment screening.

2.2.2 *Fragment screen of TIGIT.*

Protein-observed NMR screening conditions were optimized by monitoring peak intensity in ^{1}H-^{15}N SOFAST HMQC spectra and adjusting the pH, salt concentrations, and protein concentrations. Optimal conditions were found to be 0.3 mg/mL protein (26 μM) in buffer containing 50 mM Sodium Phosphate (pH = 7.0) and 25 mM NaCl. Our fragment library of 13,824 small molecule compounds was screened by recording ^{1}H-^{15}N SOFAST HMQC spectra of ^{15}N labeled TIGIT C69S in the presence of mixtures of 12 fragments at 800 μM concentration each. A mixture sample was labeled as a “hit” if chemical shift changes were observed in fragment mixture samples relative to a sample containing only DMSO (Figure 2-8).

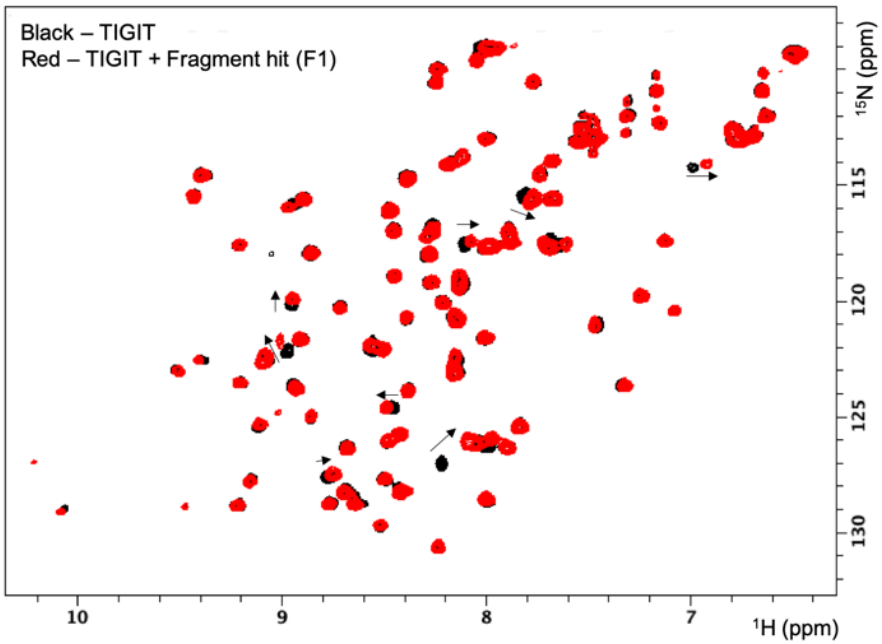

Figure 2-8. TIGIT chemical shifts seen from a deconvoluted fragment hit.
Overlayed ^{1}H-^{15}N SOFAST HMQC spectra of TIGIT alone (black) and with 800 µM of fragment hit. Chemical shift perturbations are highlighted by black arrows.

From the mixture screen, 131 mixtures were identified as hits. These mixtures were deconvoluted by first breaking down hit mixtures into sample mixtures of 3, followed by testing fragments as singletons if they were found to be hits in mixtures of 3. After deconvolution, 67 fragment hits were identified that bind to the TIGIT IgV domain with an overall hit rate of 0.5%. A qualitative visualization score (VS) was assigned to each fragment hit from 0-4 with 0 indicating no peak shifts, 1 indicating weakly shifted peak signals, and 2-4 indicating varying degree and quantity of peak shifts with 4 being the largest observed shifts. In total, we identified 2 strong hits (VS = 4), 8 moderate hits (VS = 3), and 57 weak hits (VS = 1,2).

2.2.3 *Fragment hit classes identified from the NMR screen.*

Amongst the identified fragment hits, it became evident that three different chemical shift perturbation patterns were possible upon fragment binding (Figure 2-9). Generally, a shared set of peak shifts among fragment hits would indicate a single, shared

binding site. With multiple shift patterns present, one might expect multiple fragment binding sites or a shared binding site that allows for different fragment binding poses. Both circumstances are important in fragment-based drug discovery as fragments that bind different sites can be linked together or fragments with different binding poses within the same site can be merged to rapidly increase binding affinity.[90,91]

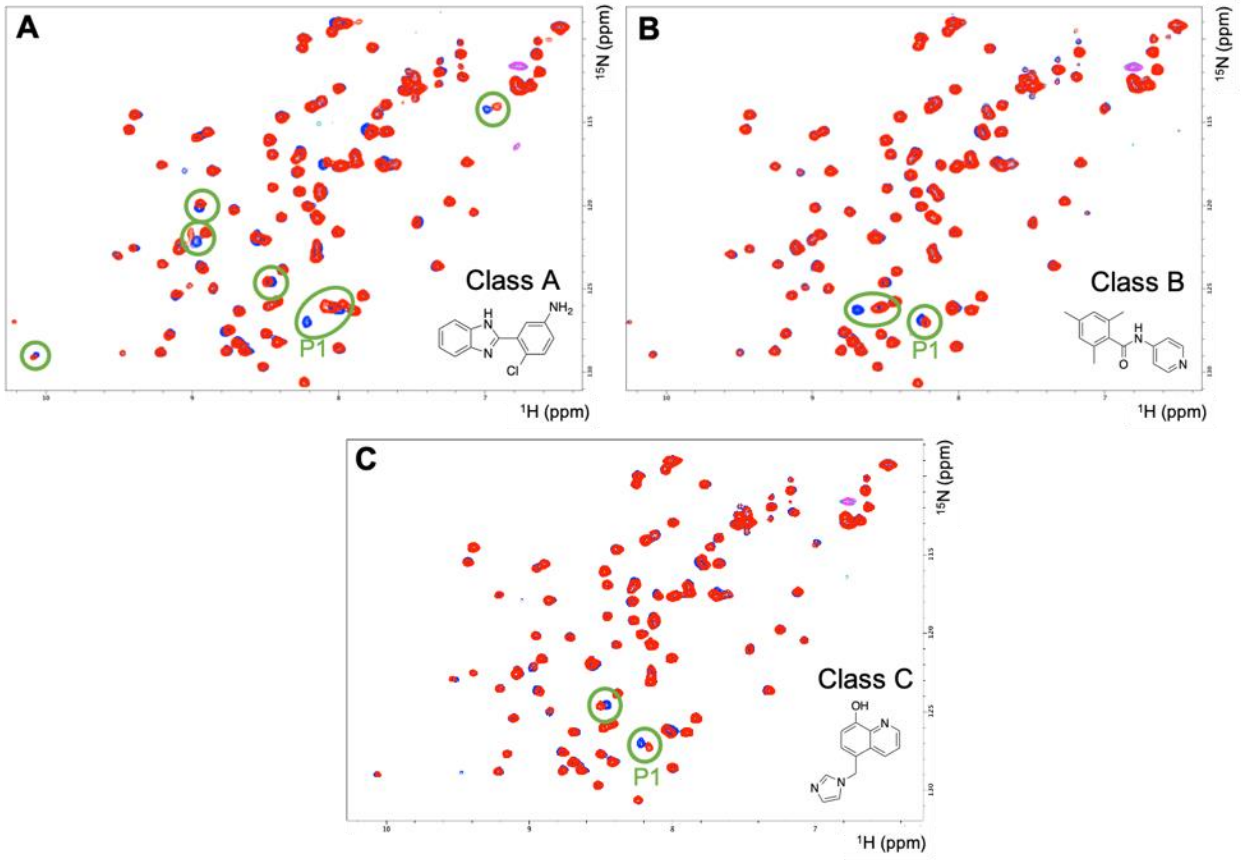

Figure 2-9. Fragment hit classes identified from NMR screen.
(A-C) Overlayed spectra from class A, B and C hits with fragment structure in the inset and peak shifts highlighted by green circles. The shared shifted resonance in all three classes is labeled as P1.

The class A shift pattern was exemplified by multiple peak shifts highlighted in Figure 2-9A and contained 50 fragment hits with 7 strong to moderate hits (VS = 3,4) and 43 weak hits (VS = 1,2). The class B shift pattern is exemplified by two shifting peak resonances one of which is shared among all classes (labeled P1) and the other is unique to the shift class (Figure 2-9B). Class B hits were few in number compared to A with 1

moderate hit (VS = 3) and 8 weak hits (VS = 1,2). The class C shift pattern similarly contains two shifting peak resonances both of which are shared with class A, however the absence of multiple shifts seen in class A led to the classification of C as a separate shift pattern (Figure 2-9C). Class C hits were the least represented with 2 moderate hits (VS = 3) and 6 weak hits (VS = 1,2). Notably, all classes shared peak shifts in resonance P1 which may suggest crossover in the binding conformations among the different classes despite the chemical dissimilarity between the classes.

2.2.4 *Fragment hit clustering.*

Fragment hits were clustered by similar chemotypes into 10 different cluster groups (Figure 2-10). The most represented clusters, 1 and 2 containing 31 fragment hits, are predominantly characterized by benzimidazole containing compounds functionalized at the 2 position. In cluster 1, the most active fragments, as measured by VS, were those functionalized with substituted anilines. Cluster 2 fragments were less active in comparison to cluster 1 and contained different thiol linked moieties off of the benzimidazole. All cluster 1 and 2 hits were characterized as class A binders. Cluster 3 is the second largest stand-alone cluster with 15 hits which are predominantly characterized by the amide linker between two variously substituted aromatic ring systems or heterocycles. The majority of cluster 3 hits were classified as class B binders and they're unique chemical structures compared to benzimidazole containing class A hits may further give credence to the existence of multiple binding poses. Cluster 4 hits are benzimidazoles substituted off of the 1-position which appear to be significantly less active than the 2-position substituted benzimidazoles of cluster 1.

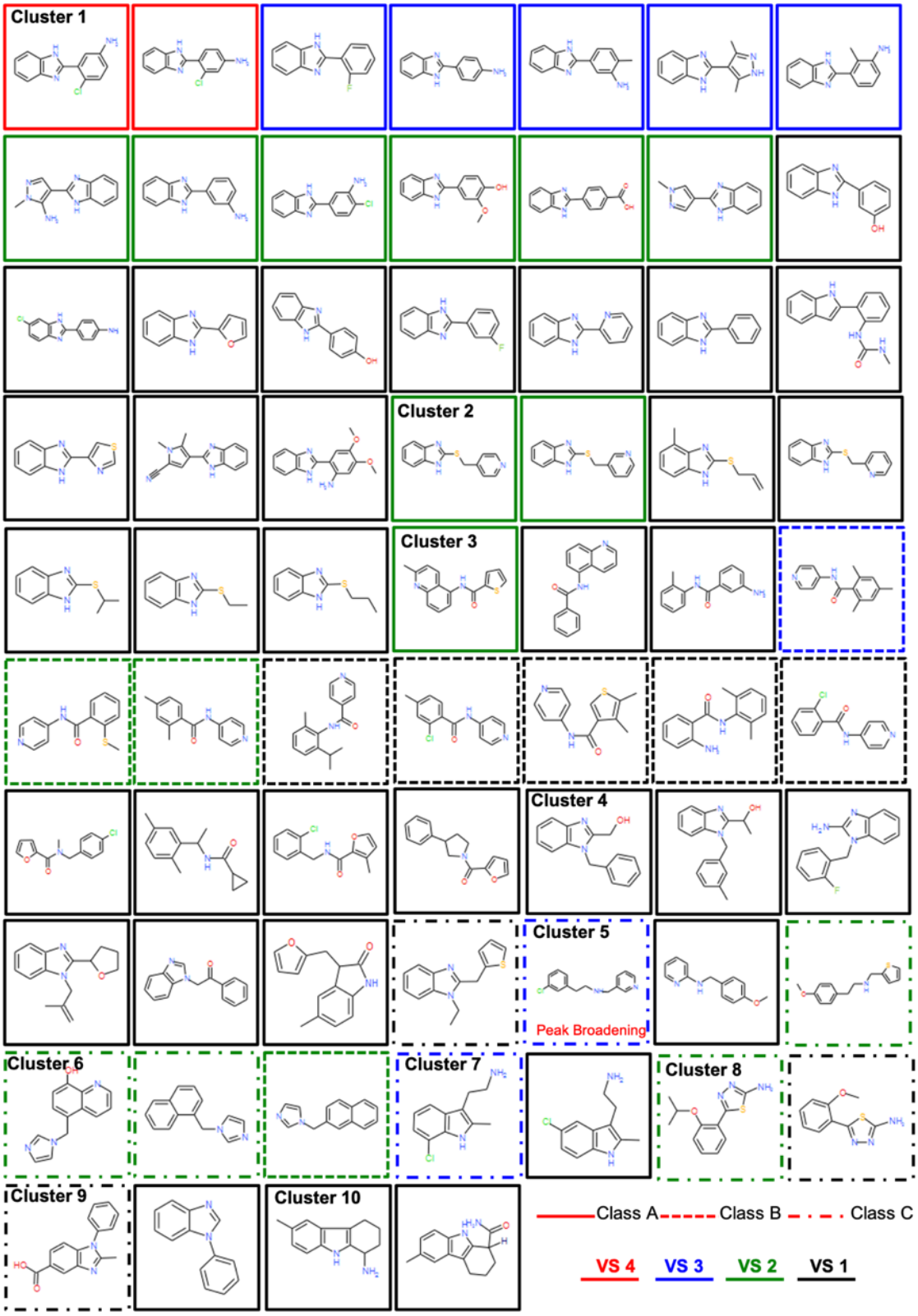

Figure 2-10. TIGIT fragment hit clusters.
Chemical structures of fragment hits identified in NMR screening and clustered by chemotype. The VS and shift class is indicated by color and type of outline around structure according to the included legend.

Clusters 5-10 contain chemical aspects of the first four clusters, were small in number, although unique enough to warrant their own groupings. All class C binders were among clusters 5-10 and did not share a specific chemical feature that may be uniquely attributable to class C binding. Included among class C binders was one fragment from cluster 5 that exhibited significant peak broadening (Figure 2-11). Peak broadening can indicate that the fragment is binding in the intermediate exchange regime with a K_d less than 10 µM, the fragment is causing a protein aggregation artifact, or the fragment is affecting the protein dynamics leading to decreased signal intensities. A further examination of the cluster 5 peak broadening hit will be discussed later.

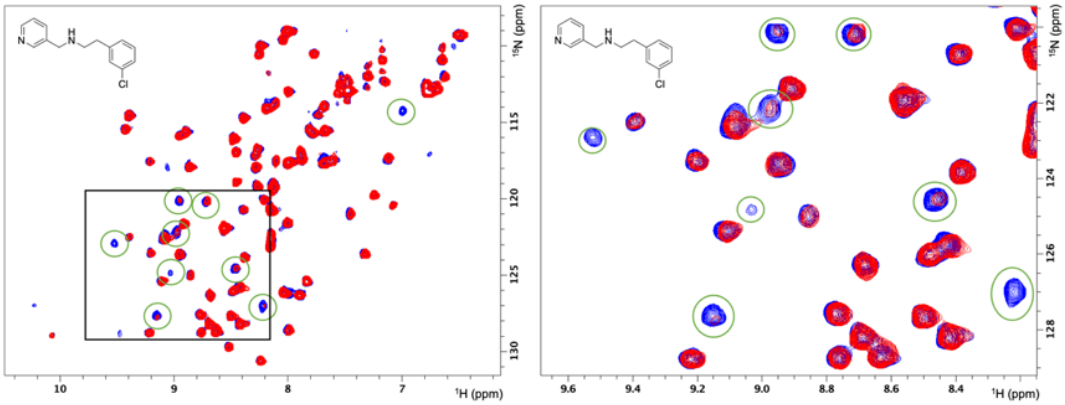

Figure 2-11. Cluster 5 fragment hit peak broadening.
SOFAST HMQC of cluster 5 hit (800 µM, structure shown in inset) with broadened peaks upon fragment addition highlighted by green circles. Zoom on right is highlighted by black box in left.

2.2.5 *Rank ordering fragment hits by NMR titration.*

Rank ordering fragment hits by VS is initially useful for prioritizing fragments of chemotype clusters for further analysis. However, qualitative VS does not always correlate with higher binding affinity due to different shielding and de-shielding properties of fragment hits that can lead to more or less significant chemical shift perturbations in NMR spectra. To more accurately rank order fragment hits based on their affinity for TIGIT, K_d values were determined from NMR titrations. Titration experiments were

conducted using a 6-point, 50% serial dilution with 1.6 mM as the top concentration of fragment (Figure 2-12A). Unfortunately, titrations conducted in this manner often failed to reach saturating concentrations complicating the calculation of binding affinities (Figure 2-12B). The binding affinities of all fragment hits from the screen were determined in this manner and ranged from 490 μM to >2 mM, with only three hits having a K_d less than 1 mM all of which were analogs of fragment **1** (Figure 2-12C). Collectively, the fragment hits identified through our NMR screen represent weak binders that may prove as difficult starting points for hit-to-lead optimization.

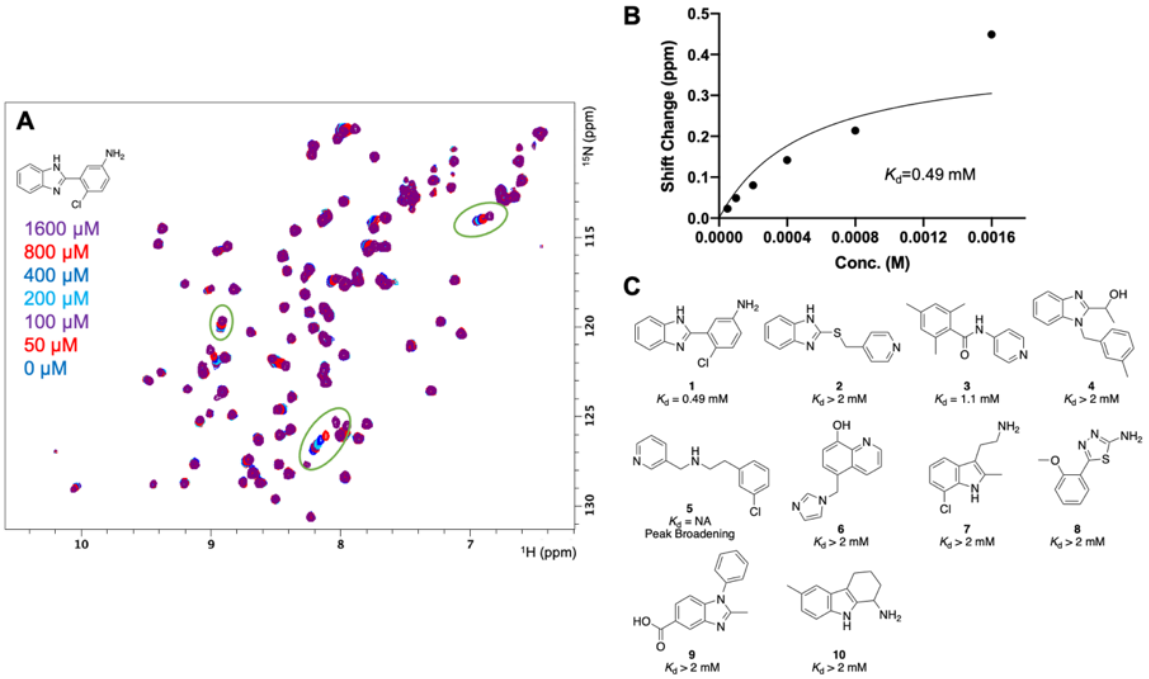

Figure 2-12. NMR titration of representative fragment hits of different chemotype classes. (A) Overlay of SOFAST-HMQC spectra of a fragment titration. Fragment concentration is coded by spectra color Binding affinities (K_d) determined by NMR titration experiments are displayed below fragment hit. (B) Peak shift changes verses compound concentration used to calculate K_d values of fragment hits. (C) Representative hits from each chemotype class with calculated K_d values.

2.2.6 *Reexamination of fragment binding to TIGIT WT.*

For screening purposes, we introduced the C69S mutation in order to avoid any non-specific covalent adducts that would produce false positive hits. Solvent-exposed C69 is a part of the AX_6G lock motif, however, the side chain is directed away from the

binding interface so we rationalized this mutation would not drastically affect lock motif conformation (Figure 2-13A). It is reasonable to reconfirm fragment binding against TIGIT WT in order in order to eliminate any notion that this mutation affected TIGIT conformation or introduced a non-native binding site. Uniformly ^{15}N-labeled TIGIT WT IgV domain was produced for rescreening the fragment hits found in our C69S screen. Interestingly, the SOFAST HMQC spectra of TIGIT WT revealed shift perturbations in peaks associated with fragment binding when compared to the C69S screening construct spectra (Figure 2-13B). Serine is spatially an acceptable analog for cysteine and usually a well-tolerated substitution when cysteine is solvent-exposed, but the polar hydroxyl sidechain of serine introduces a different chemical environment for its neighboring residues. This change in chemical environment is visualized in the comparison of the NMR spectra and suggests that the shifted resonances are localized closely to C69. Alternatively, the chemical shift perturbations could suggest a conformational change in the IgV domain, however, in this case the global similarity between the two spectra do not suggest a broader conformational change. The fact that shifted residues seen between the two protein construct spectra are shared with those seen in fragment binding would suggest that the fragment binding site is near or directly associated with the C69S lock motif residue mutation.

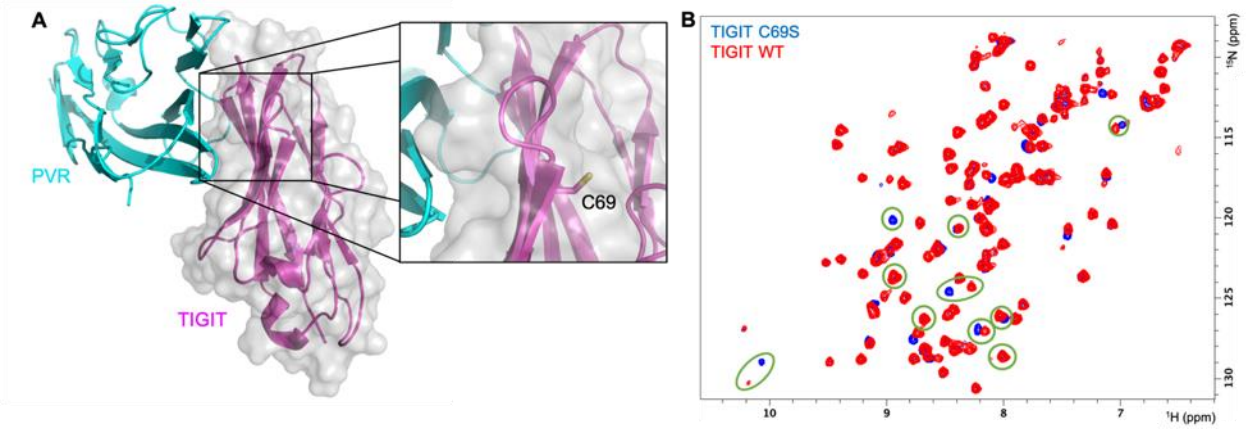

Figure 2-13. Examination of TIGIT C69S mutation.
(A) Structure of TIGIT-PVR interaction with the inset highlighting C69 side chain (sticks) directed away from interaction interface. (B) Overlay of SOFAST HMQC spectra of TIGIT C69S (blue) and TIGIT WT (red). Resonances that shift during fragment binding are highlighted with green circles.

We rescreened the best 10 fragment hits by VS against ^{15}N-labeled TIGIT WT IgV and found that cluster 1, 3, and 7 hits with a VS of 4 or 3 when screened against the C69S protein construct did not bind to TIGIT WT (Figure 2-14A). This would suggest that the introduction of serine for cysteine artificially created a new fragment binding site for which the majority of fragments found in the C69S screen bind. The only fragment that still exhibited binding against TIGIT WT was the cluster 5 hit (**5**) that induced peak broadening upon binding. As previously discussed, this peak broadening could indicate intermediate exchange, protein aggregation, or changes in protein dynamics. If **5** is binding in the intermediate exchange regime with K_d less than 10 µM, it would be assumed that shifted peak intensities would return when the protein is saturated with ligand at concentrations several times higher than the K_d. The return of peak intensity was not seen at saturating levels of **5** suggesting that this fragment is not exhibiting intermediate exchange (Figure 2-14B). It is likely then that **5** is either inducing insoluble protein aggregation or changing the protein dynamics. To test this hypothesis, **5** was removed from the NMR sample by dialysis and re-collecting HMQC spectra on the dialyzed sample. The rescue of broadened signal intensities in the dialyzed sample suggests that peak broadening is

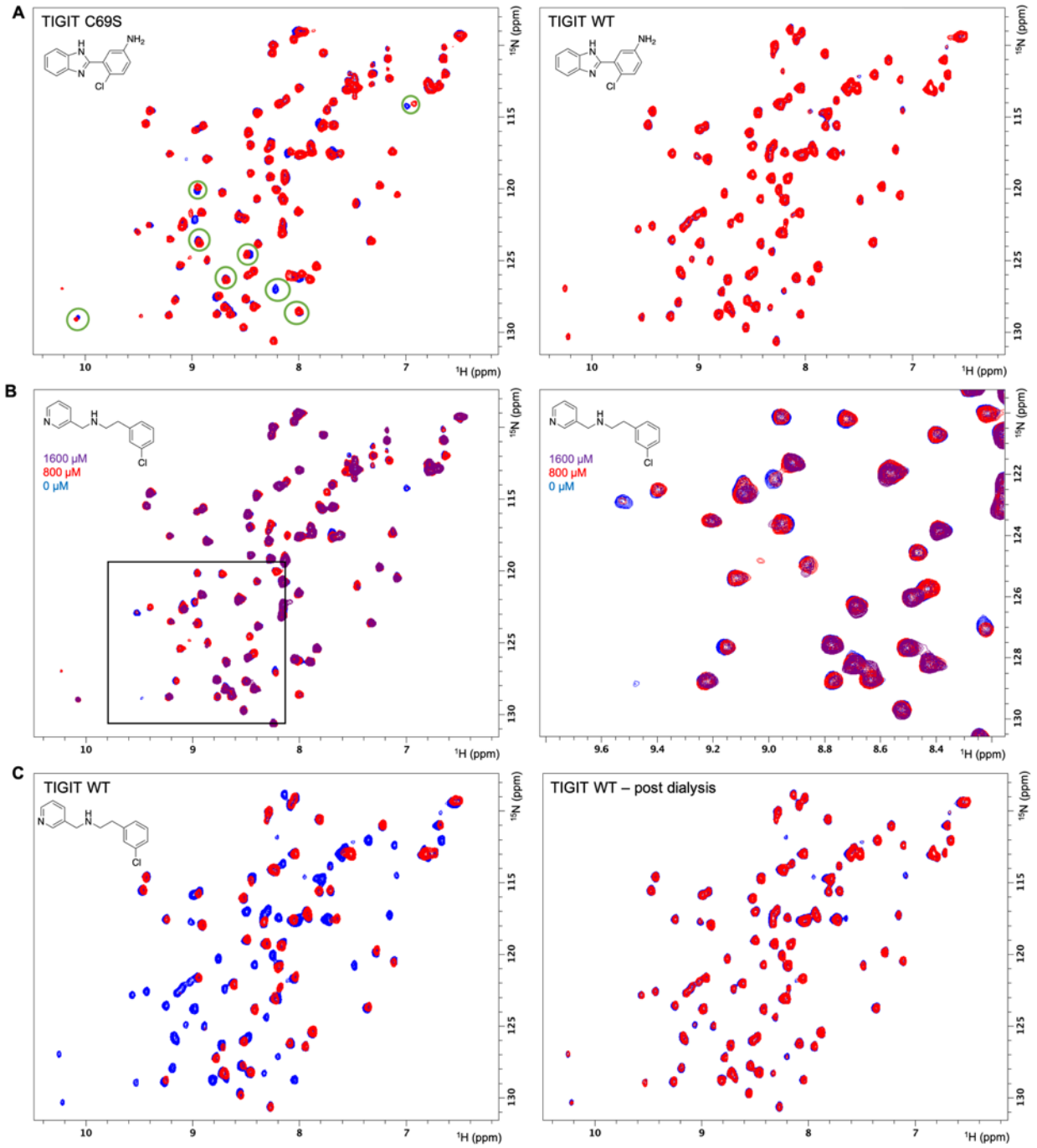

Figure 2-14. Binding of identified fragment hits against TIGIT WT.
(A) Fragment binding of **1** (800 µM, structure in inset) to TIGIT C69S (left) is not recapitulated with TIGIT WT (right). In the left spectra, peaks that shift between C69S and WT spectra as in Figure 2-13B are highlighted by green circles. (B) Titration of **5** (structure in inset) does not reveal peak intensity rescue at high concentrations. Zoom in right spectra is highlighted by black box in left spectra. (C) Peak broadening upon binding of **5** is shown in left spectra. Right spectra are collected on the same sample as in left after dialysis to remove **5** and shows the rescue of broadened peaks.

fragment specific and that the reversible binding of **5** induces a change in protein dynamics that leads to the loss of peak intensity (Figure 2-14C). The most acceptable explanation of the change in protein dynamics that leads to peak broadening is that **5** induces dimerization or soluble oligomerization of TIGIT and, thereby, decreases the molecular tumbling rate. This slower tumbling rate results in shorter T2 relaxation rates and a loss of signal over the experiment due to increased T2 relaxation.

The results of our focused rescreen of fragment hits against TIGIT WT suggest that the majority of fragment hits identified during initial screening are binding through the C69S mutation introduced in the screening construct. It is possible that the serine mutation introduces a site for hydrogen bond formation, both as a donor and acceptor, which fragments can interact with. The shared set of shift perturbations seen between fragment hits and TIGIT WT compared against apo TIGIT C69S further suggests that the mutated residue is involved in fragment interaction. Therefore, we have concluded that the majority of hits identified in our initial fragment screen are artifactual and specific to the C69S screening construct. This leads us to believe that TIGIT is much less “druggable” than initially indicated by fragment screening. Rescreening the fragment library against TIGIT WT is not predicted to produce significantly different screening results as the AX_6G lock motif is not considered to be conformationally impacted by the C69S mutation, particularly at the TIGIT-PVR interface “hot spot.” The lone reconfirmed hit, fragment **5**, likely induces dimerization or oligomerization of the TIGIT IgV domain and has potential as a TIGIT inhibitor if the ligand-induced dimerization could be optimized to be strong enough to disrupt TIGIT interaction with PVR.

2.2.7 *Attempts to obtain crystal structure of fragment 5 binding.*

Further structural information of binding would be necessary to evaluate if fragment **5** could be a hit-to-lead candidate. To this end, the confirmed fragment hit **5** was used with TIGIT WT and TIGIT C69S to set up co-crystal screening plates for structure determination through X-ray crystallography. To approach saturation during co-crystallization, concentration levels of **5** were set at 4 mM. Commercially available crystallization screens (Index HT and JCSG+) designed to sample diverse reagent sets were used in attempts to produce a fragment bound TIGIT structure.

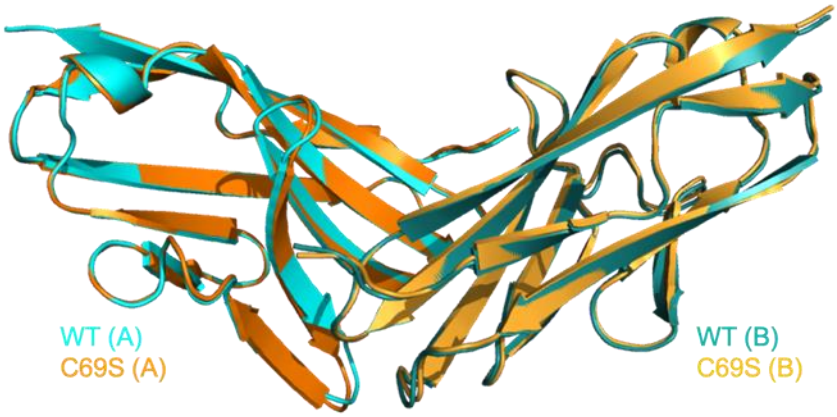

Figure 2-15. TIGIT WT and C69S crystal structures.
TIGIT WT (orange) and C69S (teal) IgV domain structures are aligned and overlayed. The two IgV domain monomers in the asymmetric unit are labeled A and B.

Crystals that formed from the screening plates were cryoprotected with glycerol and shipped to the Advanced Photon Source at Argonne National Laboratory for data collection. These crystals did not diffract well with the best attainable resolutions around 3.0 Å. In all cases, structures resulting from the low-resolution diffraction data collected did not contain electron densities that could be attributed to a bound ligand. It is notable, however, that structures resulting from both protein constructs, WT and C69S, were nearly identical with an RMSD = 0.69 Å (Figure 2-15). These structures further confirm

that the C69S mutation does not significantly impact the global IgV domain conformation and suggest that rescreening of TIGIT WT would be largely redundant.

It is possible that fragment **5** did not reach saturation even at the high concentration used or that fragment binding disrupts intermolecular contacts needed for crystal packing. In fact, ours and previous TIGIT structures suggest that ligand binding at the AX_6G "lock" motif may disrupt crystal packing. The TIGIT IgV domain structure PDB 3UCR was solved with 4 monomers in the asymmetric unit (Figure 2-16A). The internal core dimer is centralized around a face-to-face interaction between the two A'GFCC'C" β-sheet faces of TIGIT monomers (Figure 2-16B). This crystal packing would completely bury and occlude the lock motif from any binding ligands and, therefore, any ligands bound at the lock motif would disrupt this crystal packing interaction. It is not unreasonable to believe different crystallization conditions can be found to allow for ligand-bound crystal growth, however those attempts were unsuccessful in our hands. With only one confirmed fragment hit and the failed attempts to obtain a co-crystal structure, efforts to develop small molecule inhibitors against TIGIT were deprioritized.

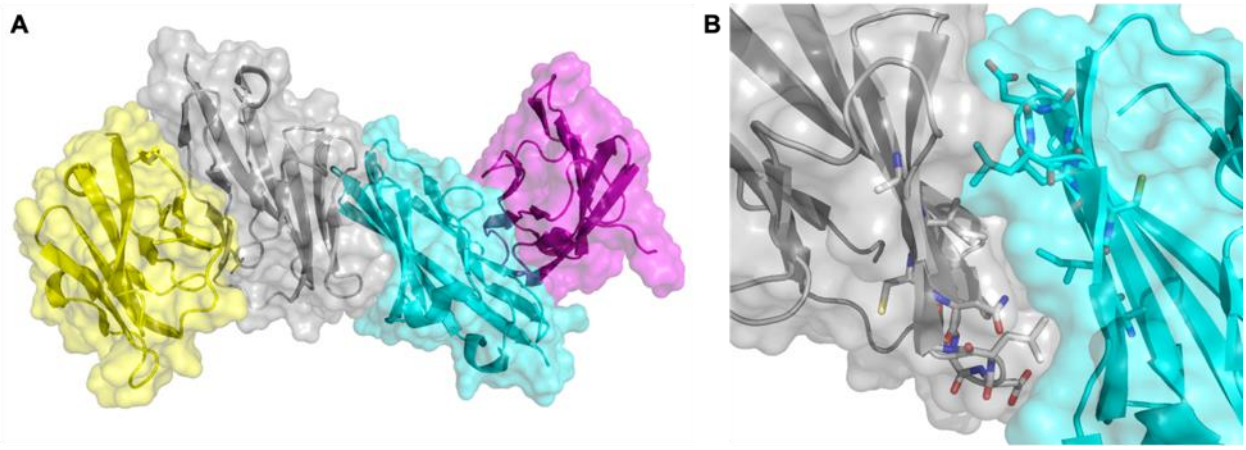

Figure 2-16. Crystal packing of TIGIT IgV domain.
(A) TIGIT IgV domain structure (PDB ID: 3UCR) with all TIGIT monomers in the asymmetric unit shown as different colored cartoons with transparent surface maps. (B) Dimer interaction between internal two TIGIT monomers. AX_6G "lock" motif residues in both monomers are shown as sticks.

2.3 Conclusions

Our initial fragment screen against the TIGIT C69S IgV domain resulted in the identification of 67 low-affinity fragment hits with a 0.5% hit rate. A hit rate of this level suggests that TIGIT is potentially druggable based on a previous analysis of fragment-based screens in which greater than 0.1% hit rate from a fragment screen can result in high-affinity small-molecule ligands against the target protein.[72] A focused rescreening of the best identified hits against TIGIT WT revealed that the majority of hits do not bind to TIGIT WT. As indicated by he shared set of shift perturbations seen between fragment hits and TIGIT WT compared against apo TIGIT C69S, the most likely explanation is that the fragment hits identified directly interact with the introduced C69S mutation. We concluded that these hits were specific to the C69S construct. Crystal structures of WT and C69S did not reveal significant conformational differences suggesting rescreening the fragment library against TIGIT WT would be redundant and not yield new chemical matter.

The lone confirmed hit against TIGIT WT, fragment **5**, induces resonance peak broadening. Based on the reversible nature of this loss of signal, it is likely that fragment **5** induces dimerization or oligomerization of the TIGIT IgV domain. Optimization of ligand-induced dimerization could lead to a viable compound with TIGIT inhibiting capabilities. However, with a single fragment hit and without guidance from structural information, a direct path forward for medicinal chemistry was unclear. It remains plausible that fragment **5** binding could be optimized through more traditional exploratory medicinal chemistry, however an NMR-based primary assay would be problematic for rank ordering new analogs as K_d is not readily extractable from NMR spectra with peak disappearance. For

these reasons, we decided to deem TIGIT undruggable by small molecules and shift fragment screening efforts to other immune checkpoint targets.

2.4 Methods

2.4.1 *Protein expression and purification.*

The genes encoding for the extracellular domain of human TIGIT WT and C69S (residues 23 – 128, MW=11.5 kDa) were synthesized with codon optimization for E. coli expression and inserted into the pET28b vector using *NdeI* and *XhoI* to contain a thrombin cleavable N-terminal 6-His tag (GenScript) and transformed into E. coli BL21 (DE3) cells. Uniformly ^{15}N labeled TIGIT was expressed as inclusion bodies in M9 minimal media containing $^{15}NH_4Cl$ as the sole nitrogen source. Protein production was induced with 1 mM IPTG at OD600 of 0.8 and harvested 4 hours later. The cell pellet was frozen and resuspended in lysis buffer (50 mM Tris-HCl pH = 8.5, 150 mM NaCl, 20 mM DTT, 2 mM EDTA and 1 mM PMSF) prior to lysis by homogenization. Inclusion bodies were collected by centrifugation and washed twice with the lysis buffer containing 2% Triton. Inclusion bodies were additionally washed with lysis buffer containing 1% Triton, 0.5% Triton, and 1.5 M NaCl wash steps. Purified inclusion bodies were solubilized in 50 mM Tris-HCl pH = 8.5, 200 mM NaCl, 7.5 mM beta-mercaptoethanol, 6M Guanidine HCl for 2 hours at room temperature. The solubilized inclusion bodies were filtered through a 0.45 μm filter and refolded by dropwise rapid dilution into the TIGIT refolding buffer (50 mM Tris-HCl pH = 8.0, 1 mM reduced glutathione, and 1 mM oxidized glutathione). After 24 hours refolding at 4 ˚C, refolding buffer containing TIGIT was filtered and loaded to a ProBond nickel column (Thermo) using the refolding buffer as Buffer A and the refolding buffer + 500 mM imidazole as Buffer B. Eluted TIGIT was dialyzed against 10 mM Tris-HCl pH =

8.0 and 20 mM NaCl to remove imidazole. After dialysis, the N-terminal 6-His tag was removed with thrombin (10 units of thrombin per mg of TIGIT). Monomeric TIGIT was collected from size exclusion chromatography (Superdex75 26/60) pre-equilibrated with NMR buffer (50 mM Sodium Phosphate pH = 7, 25 mM NaCl).

2.4.2 *NMR experiments.*

NMR screening was performed at 25 °C using a Bruker Avance III 600 MHz spectrometer equipped with a 5 mm single-axis z-gradient cryoprobe and Bruker SampleJet sample changer. Screening samples (500 µL) screened contained 26 µM of ^{15}N TIGIT C69S, 12 fragments at 800 µM each, and 4% DMSO-d6. ^{1}H-^{15}N SOFAST-HMQC spectra were obtained using 24 scans and analyzed using Topspin (Bruker BioSpin). Deconvolution of hit mixtures was necessary to isolate individual hit fragments. Deconvolution was accomplished by screening each twelve-compound mixture hit as a series of mixtures of three fragments followed by singleton fragment samples at 800 µM.

SOFAST-HMQC titration experiments were used to quantify the binding affinity of the best hits identified from the screen. The change in ^{1}H-^{15}N chemical shifts of backbone resonances upon the stepwise addition of fragment was measured and fit by an in-house script.

2.4.3 *Protein crystallization, data collection, and structure refinement.*

Screening of crystallization conditions of TIGIT WT and TIGIT C69S with fragment **5** were described above. X-ray data were collected on the Life Sciences Collaborative Access Team (LS-CAT) Sector-21 beamlines at the Advanced Photon Source (APS), Argonne National Labs. Data were indexed, integrated, and scaled with HKL2000.[92] Molecular replacement with Phaser[93] was accomplished using Phenix[94] and the TIGIT

IgV domain structures previously determined (PDB ID: 3QOH) as the search model.[95] Structure refinement was accomplished with Phenix and included several rounds of manual model building with COOT. Final refinement and X-ray data collection statistics are provided below in Table 1. Figures have been prepared using PyMOL unless otherwise stated.[96]

Table 2-1. X-ray data collection and refinement statistics for TIGIT WT and C69S.

Construct	**WT**	**C69S**
Data Collection		
Space Group	P6422	P6422
Cell Dimensions		
a, b, c (Å)	117.599, 117.599, 99.282	117.544, 117.544, 99.435
α, β, γ (˚)	90, 90, 120	90, 90, 120
Resolution (Å)	29.40 – 2.90 (2.95 – 2.90)	28.23 – 3.00 (1.83 – 1.80)
Rmerge (%)	10.6 (211.4)	10.5 (191.4)
Mean I / σI	42.4 (1.9)	40.5 (2.0)
Completeness (%)	100 (100)	100 (100)
Redundancy	29.4 (30.3)	23.5 (24.2)
Structure Refinement		
No. Reflections	9430	8522
R_{work} / R_{free}	0.2197 / 0.2510	0.2174 / 0.2636
R.m.s deviations		
Bond lengths (%)	0.010	0.010
Bond angles (˚)	1.265	1.416
Ramachandran		
Preferred regions (%)	93.33	90.00
Allowed regions (%)	6.19	8.57
Disallowed regions (%)	0.48	1.43

Related to Figures 2-15 and 2-16. Highest resolution shell is in parentheses.

Chapter 3 - Fragment screen of T cell immunoglobulin mucin receptor 3 (TIM-3).

3.1 Introduction

3.1.1 *TIM-3 is a validated target for cancer immunotherapy.*

T cell immunoglobulin and mucin domain-containing molecule 3 (TIM-3; HAVCR2) has been identified as an immune checkpoint receptor involved in regulating innate and adaptive immunity.[97] TIM-3 is a negative regulator of immune activity expressed on several immune cell types including T-helper 1 (Th1) lymphocytes, cytotoxic $CD8^+$ T cells, dendritic cells, natural killer (NK) cells, and macrophages. High levels of TIM-3 expression correlate with the suppression of T cell responses and T cell dysfunction in cancer.

Studies carried out in different cancer settings conclusively establish that TIM-3 acts as a negative regulator of anti-tumor immunity due to its association with T cell exhaustion in the tumor. TIM-3 expression on exhausted T cells is usually associated with the well-established immune checkpoint protein programmed death receptor 1 (PD-1) expression. $TIM\text{-}3^+$ $PD\text{-}1^+$ cells are considered “deeply” exhausted T cells from both human and animal studies, supporting a functional correlation between TIM-3 and PD-1 during the development of T cell exhaustion.[40–42] Furthermore, upregulation of TIM-3 has been implicated in the adaptive resistance to PD-1 mAb blockade in both mouse models and patients[44] and has been associated with a poor prognosis for tumor progression.[98,99] In patients with advanced melanoma, $TIM\text{-}3^+$ $PD\text{-}1^+$ $CD8^+$ T cells represent a highly dysfunctional population of T cells and approximately 30% of $CD8^+$ T cells express TIM-3.[41] Similarly, in patients with NSCLC, approximately 30% of $CD8^+$ and 60% of $CD4^+$ $FoxP3^+$ TILs express TIM-3.[100] The presence of functionally superior immunosuppressive $TIM\text{-}3^+$ $CD4^+$ $FoxP3^+$ Treg cells seems to be a common feature across multiple forms of

cancer, including hepatocellular, ovarian, colon, and cervical carcinomas.[101] Accumulating evidence suggests that TIM-3 is also expressed on cancer cells such as melanoma, osteosarcoma, cervical cancer, and clear cell renal cell carcinoma.[102–105]

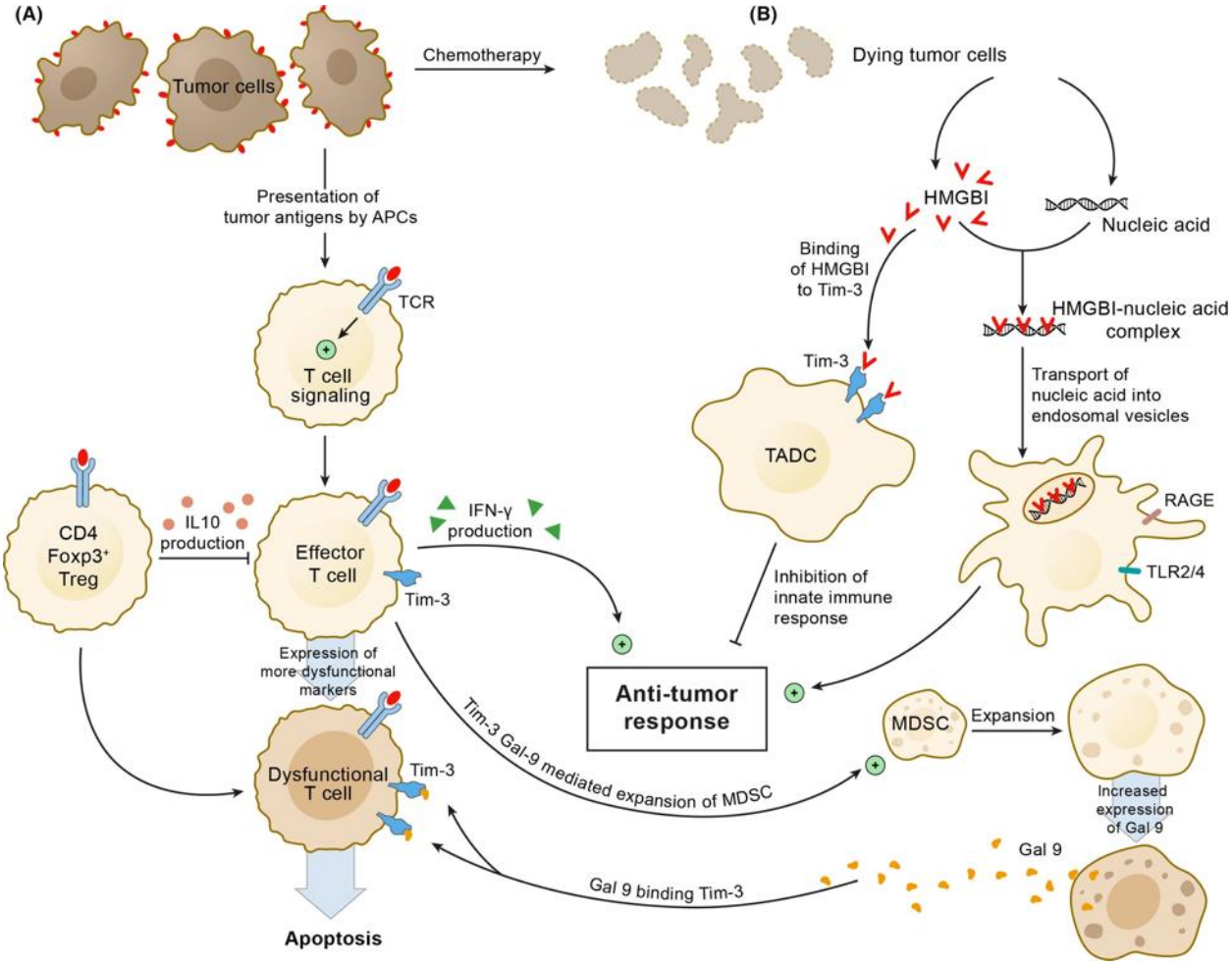

Figure 3-1. TIM-3 mechanism of inhibition in cancer.
Tim-3 serves as a major regulator of immunity. In DCs, TIM-3 deters the transport of nucleic acids into endosomal vesicles and consequently limits protective innate immune responses to tumor-derived stress factors. TIM-3 expressing effector T cells promote expansion of myeloid-derived suppressor cells (MDSC). Increased Galectin-9 (Gal9) molecules, which then bind to Tim-3 molecules expressed on Tim-3 expressing effector CD8+ T cellsleading to apoptosis of effector T cells. Tim-3+FoxP3+ Tregs present within the tumor express high amounts of Treg effector molecules and inhibit effector T cells. Adapted from Das et al., 2017.[106]

Several studies have suggested that TIM-3 can promote tumor progression through different mechanisms, including facilitating tumor cell migration and invasion, directly suppressing T cells, facilitating myeloid-derived suppressor cell (MDSC)

expansion, or activating the well-known oncogenic mTOR pathway (Figure 3-1).[104,106–108] Cumulatively, these studies characterize TIM-3 as a promising immune checkpoint target deserving of a focused drug discovery effort. TIM-3 has emerged as a target for numerous mAb-based therapeutics that are currently under clinical development both as a single agent and in combination therapies. Early clinical trial data has shown efficacy in combination with chemotherapy in myelodysplastic syndrome (MDS) and acute myelogenous leukemia (AML)[109] as well as in advanced or relapsed refractory solid tumors as a monotherapy.[110]

3.1.2 *TIM-3 structure and function.*

TIM-3 is a single-pass transmembrane protein that consists of a membrane distal variable immunoglobulin (IgV) domain, a mucin domain, a transmembrane domain, and a cytoplasmic tail involved in phosphotyrosine-dependent signaling. The primary receptor interaction domain in TIM-3 is the membrane-distal IgV domain (residues 22-130) which is largely conserved with mTIM-3. The IgV domain is characterized by a two anti-parallel β-sheet sandwich formed from front AFGCC'C" and back BED faces which are linked by B-C, E-F, C"-D, and A-B loops (Figure 3-2A). The two faces are stabilized by inter-sheet interactions and three disulfide bonds: one internal bond between C38 and C110 which stabilizes the two β-sheets and two noncanonical bonds between C52 and C63, and C58 and C109 which stabilize the upward fold of the CC' loop forming the FG-CC' cleft. The FG-CC' cleft is a conserved feature of TIM family proteins and has been reported to possess a conserved metal ion-dependent ligand binding site that is capable of chelating a single calcium cation (Ca^{2+}) (Figure 3-2B).[111,112] The TIM-3 IgV domain has three predicted N-linked glycosylation sites (N33, N100, and N124).

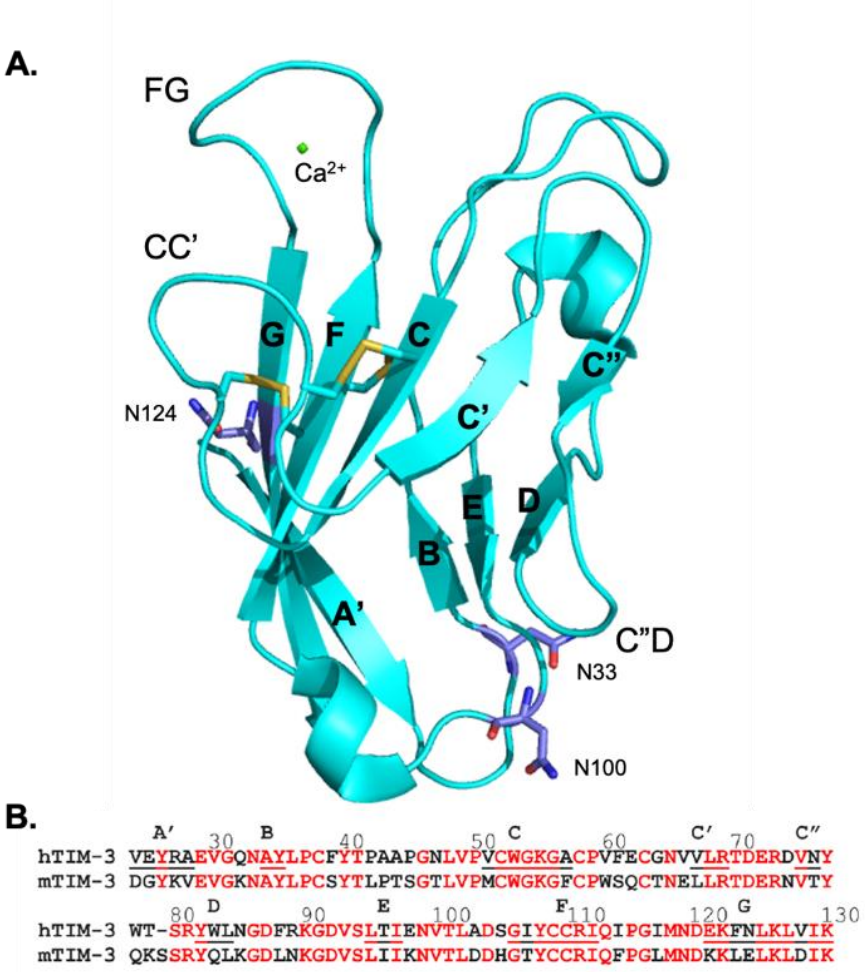

Figure 3-2. TIM-3 primary and tertiary structure.
(A) 3D structure of the TIM-3 IgV domain (PDB 6DHB) with labeled β-strands and loops. Disulfide bonds and potential N-linked glycosylation sites (purple) are shown as sticks. Calcium (Ca^{2+}) coordinated in the FG-CC' cleft is shown as a green sphere. (B) Sequence alignment of human and mouse TIM-3 IgV domains. Conserved residues are red the β-strands are labeled above the sequences and underlined in red and black for conserved and no-conserved, respectively.

Previous studies have identified four TIM-3 ligands that interact with the IgV domain: phosphatidylserine (PtdSer), carcinoembryonic antigen-related cell adhesion molecule 1 (CEACAM1), high mobility group box 1 (HMGB1), and galectin-9.[113–116] Galectin-9, the first reported natural TIM-3 ligand, was found to bind TIM-3 through the interaction of the two carbohydrate recognition domains of galectin-9 and N-linked oligosaccharides of the IgV domain. The elucidation of the crystal structure of mTIM-3 IgV domain led to the discovery of the conserved FG-CC' binding cleft shared among TIM

family members as a galectin-9 independent binding site.[117] Interestingly, both galectin-9 and CEACAM1 binding events have been separately shown to induce a TIM-3 active state leading to the phosphorylation of Y256 and Y263 despite having independent binding sites.[116,118]

The Tim-3 cytoplasmic tail adjacent to the trans-membrane domain is devoid of the classical inhibitory switch motifs found in other inhibitory receptors. It does, however, contain a conserved region of five tyrosine residues, two of which have been shown to be critically important for coupling to downstream signaling pathways. Although the precise intracellular signaling mechanism has not been fully elucidated, it has been found that Y256 and Y263 are critical for the binding of HLA-B associated transcript 3 (BAT3), to the C-terminal tail of Tim-3.[119] The peptide sequences surrounding these two tyrosine residues are highly conserved and function as SH2 domain-binding motifs, where multiple SH2 domain-containing kinases including Fyn, Lck, PI3K p85, and Itk are found to bind.[118,120] Many of these molecules are key components of the T cell receptor (TCR) signaling pathway, indicating a functional relationship between TIM-3 and the TCR pathway. It has been found that Tyr256 and Tyr263 are critical for the binding of HLA-B associated transcript 3 (Bat3), to the C-terminal tail of TIM-3.[119] In its inactive state, Bat3 recruits the catalytically active form of Lck and forms an intracellular molecular complex with TIM-3 that preserves and potentially promotes T cell signaling and represses TIM-3-mediated cell death and exhaustion (Figure 3-3A). When ligand bound and in its active state, Y256 and Y263 are phosphorylated and BAT3 is released from the Tim-3 tail, thereby promoting Tim-3-mediated T cell inhibitory function by allowing binding of tyrosine kinase FYN resulting in immunological synapse disruption and phosphatase recruitment

(Figure 3-3B). Consequently, the cell becomes anergic and undergoes apoptosis through the induced intracellular calcium influx.[115] Because FYN and BAT3 bind to the same domain in the TIM-3 cytoplasmic tail, a likely molecular switch between TIM-3-Bat3 and TIM-3-FYN might trigger the switch of TIM-3 function from being permissive to TCR signaling to inhibition of proximal TCR signaling.

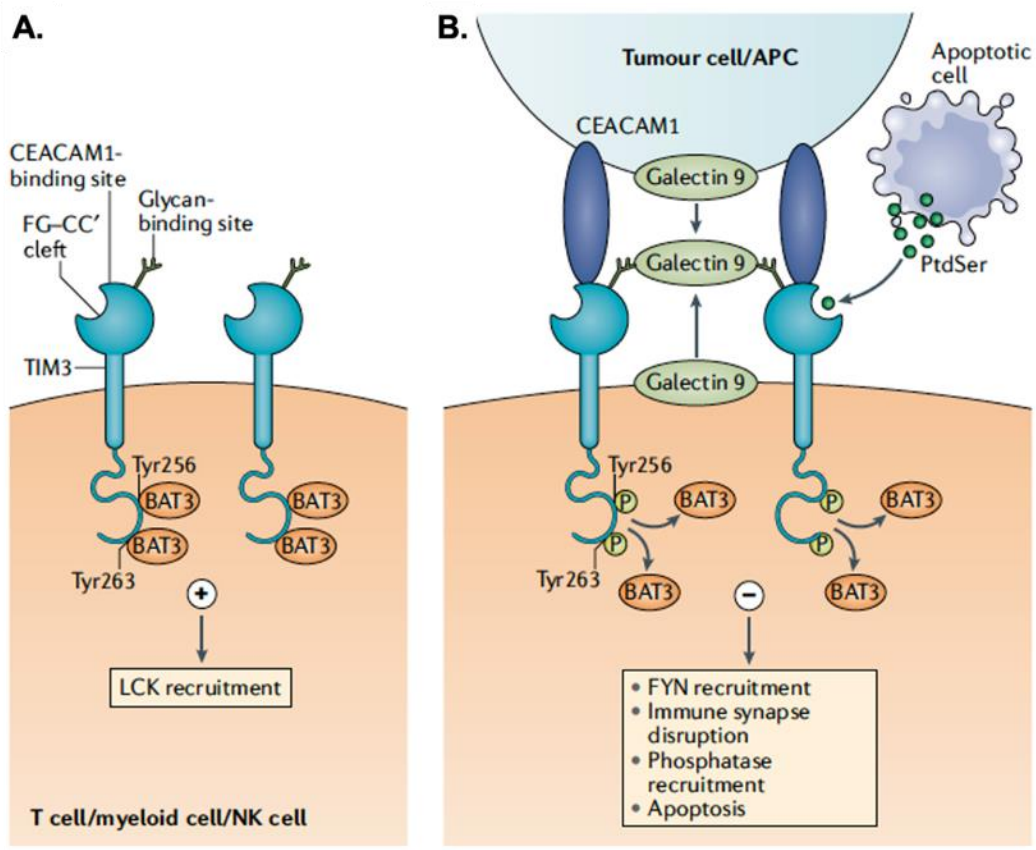

Figure 3-3. Models for TIM-3 activation states and ligand binding.
TIM-3 inhibits immune cells when in its active, ligand-bound state. (A) In its inactive, unbound state, the cytoplasmic tail of TIM-3 interacts with BAT3 and maintains T cell activation by LCK recruitment. (B) Ligand binding of galectin-9 or CEACAM1 leads to phosphorylation of Y256 and Y263, release of BAT3, and recruitment of FYN. This results in the disruption of immune synapse formation and phosphatase recruitment, and ultimately leading to cell apoptosis. Adapted from Wolf et al., 2020.[121]

While phosphorylation of Y256 and Y263 is widely accepted as the trigger of TIM-3 inhibitory function, the structural dynamics that lead to this event are unknown. Generally, single-pass transmembrane receptor activation mechanisms are not fully understood. However, the study of transmembrane domains of single-pass receptors has

suggested that most transmembrane domains have a tendency to self-associate.[122,123] Transmembrane domain self-association contributes to the overall dimerization of the protein but is also balanced by the potential positive or negative interactions of the soluble domains. It is likely that each receptor has a particular set of conditions, including ligand binding, that leads to receptor oligomerization and activation. A working mechanistic hypothesis of receptor activation includes potential contributions from ligand-induced dimerization, ligand-induced rotation, and clustering (Figure 3-4A).[124] In each circumstance, ligand binding to the receptor can lead to the reduction of free energy barriers to oligomerization allowing for dimerization, rotation, and/or clustering (Figure 3-4B).

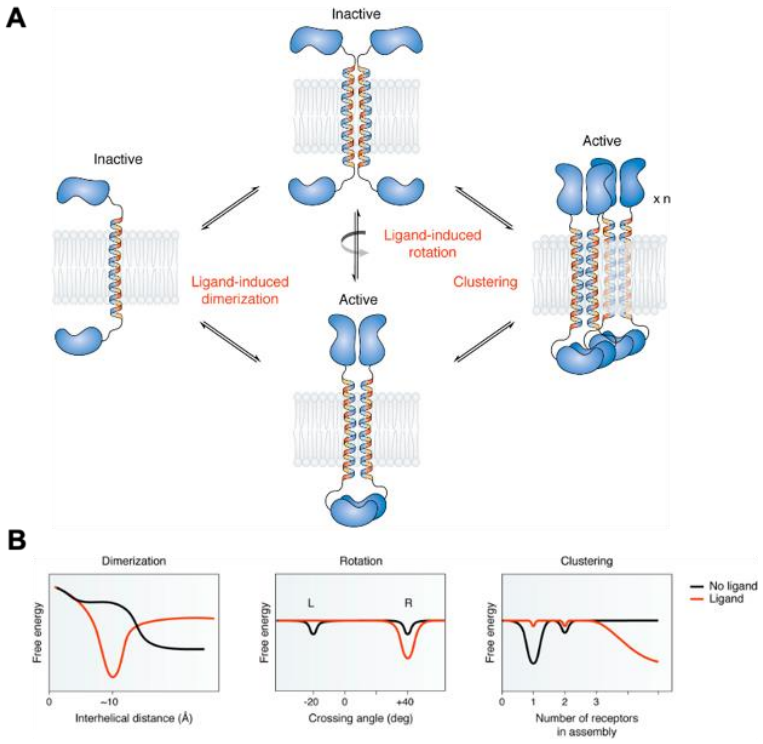

Figure 3-4. Single pass transmembrane receptor mechanisms of activation.
(A) Lingand-induced dimerization and ligand-induced rotation hypotheses posit that ligand binding to the extracellular domains brings receptor monomers together or brings intracellular domains into active configurations to form a signaling-competent dimer. Clustering occurs when receptors are stabilized as higher order oligomeric signaling complexes. These mechanisms are not mutually exclusive and may be utilized in combination. (B) Receptor activation is energetically unfavorable when not ligand bound. Ligand binding reduces the free energy barriers and stabilizes dimerization, rotation, and/or clustering. Adapted from Westerfield, 2019.[124]

In the context of TIM-3, both ligands CEACAM-1, which has been shown to interact with TIM-3 in *cis* and *trans*, and galectin-9, which is a tandem-repeat protein containing two carbohydrate recognition domains capable of TIM-3 binding through N-linked glycans, would have potential clustering effects which may lead to receptor activation. It is also possible that these events are not mutually exclusive and galectin-9 induced clustering and CEACAM-1 induced conformational changes to the IgV domain and required for complete signal transduction. Both binding events have separately been shown to induce phosphorylation of Y256 and Y263. However, it should be noted that CEACAM1 engagement of the FG-CC' cleft alone has not been shown to induce apoptosis, but galectin-9 binding of N-linked glycans does. This may suggest multiple functional and/or activation states of TIM-3 depending on specific ligand binding that lead to different functional cellular outcomes. TIM-3 biology is complicated by its non-canonical signaling, a broad expression across different immune cells, and multiple ligands. Further molecular tools may be necessary to fully understand aspects of TIM-3 activation and subsequent biological outcomes.

3.1.3 *Flexibility of TIM-3 IgV domain.*

Previously solved crystal structures of the TIM-3 IgV domain suggest a high degree of flexibility in the loop regions of the IgV domain. Two structures of the human TIM-3 IgV domain have been previously deposited in the PDB representing two unique states: calcium (Ca^{2+}) coordinated in the FG-CC' cleft (PDB 6DHB, Figure 3-5A)[95] and sodium (Na^{+}) bound in the C"D loop (PDB 5F71, Figure 3-5B).[125] The Ca^{2+} coordinated state is considered to be the more biologically relevant state as ligands that bind the FG-CC' cleft, PtdSer, CEACAM-1, and HMGB1, have all been shown to do so in a calcium dependent

manner.[113,114,116] Furthermore, the Ca^{2+} coordinated structure is the more energetically favorable conformation over the Na^{+} bound structure based on MacroModel (Maestro) potential energy calculations. Interestingly, the binding affinity of Ca^{2+} with the FG-CC' site has been reported to be 27.2 mM as assayed through NMR titration experiments.[95] With this weak reported binding affinity combined with an estimated extracellular concentration of ionized and free Ca^{2+} ranging from 1.1-1.4 mM (2.2-2.6 mM total including bound Ca^{2+}),[126] the proportion of TIM-3 that could be expected to be Ca^{2+}-bound at the cell surface would be less than 10%, assuming standard equilibration kinetics and ignoring the potential contributions of energetic coupling between Ca^{2+} and cognate ligand binding. A global examination of the two IgV domain structures reveals that the primary conformational differences lie in the BC and C"D loops (Figure 3-4AB). These observed differences are likely associated with the flexibility of BC and C"D loop regions, which may also account for the missing assignments of the BC and C"D loop regions in NMR studies.[95] Taken together, the potential for a low proportion of Ca^{2+} bound and the flexibility of the BC and C"D loops suggest the IgV domain is rapidly sampling many different conformations. Ligand binding likely solidifies the adoption of a specific conformation that can lead to activation of TIM-3 signaling. Conversely, if the binding of a compound can rigidify the IgV domain in an inactive conformation, TIM-3 activation can be inhibited. Therefore, it is warranted to screen an uncoordinated IgV domain to find small molecules that can potentially lock TIM-3 in inactive conformations.

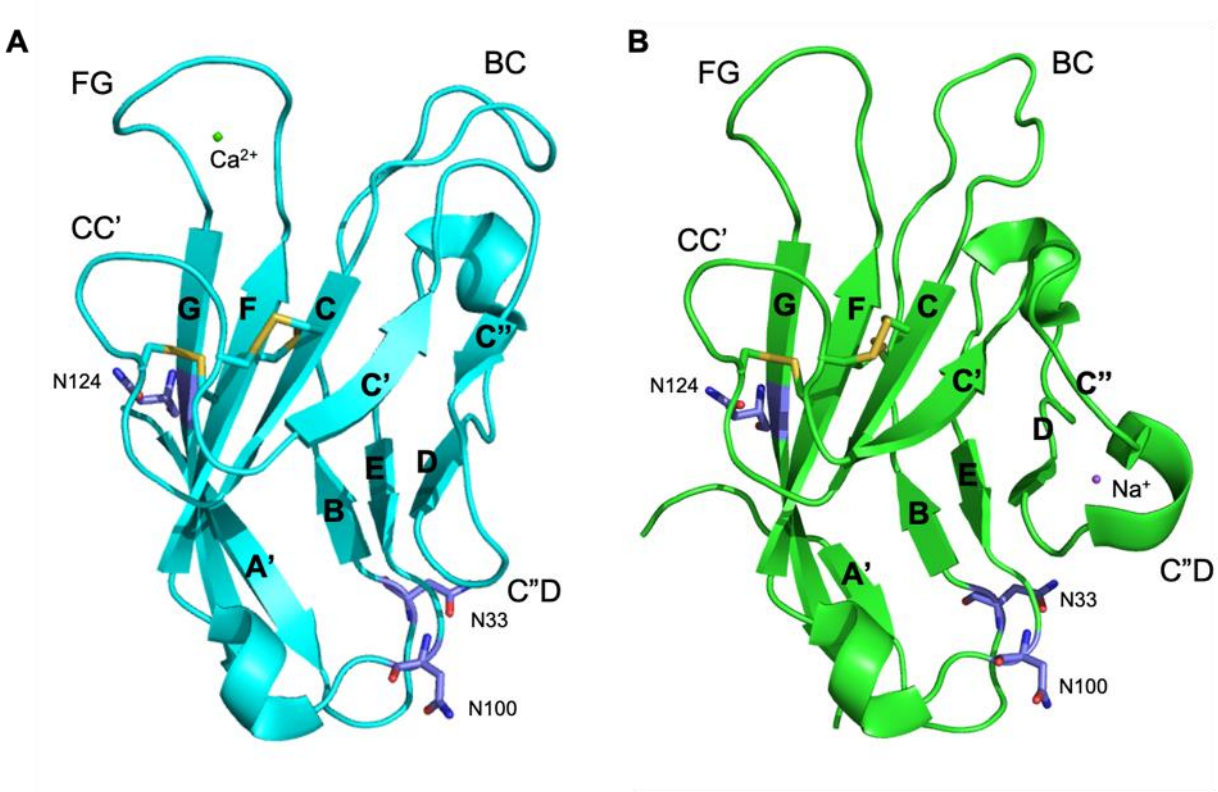

Figure 3-5. Crystal structures of apo TIM-3 IgV domains.
(A) TIM-3 IgV domain (PDB ID: 6DHB) (cyan) with beta strands and loop regions are labeled and coordinated Ca^{2+} is shown as a green sphere. Potential N-linked glycosylation sites are highlighted as purple sticks. (B) TIM-3 IgV domain (PDB ID: 5F71) (green) displayed as in (A) with Na+ shown as a purple sphere.

3.2 Results*

3.2.1 *Expression and purification of TIM-3.*

The IgV domain is the only reported interaction domain for TIM-3, therefore the mucin domain, transmembrane domain, and cytoplasmic tail can be removed for screening purposes. The TIM-3 IgV domain (residues 22-130, MW=12.3 kDa) was cloned

* Portions of this section were previously published in Rietz, T.A., et al. Fragment-Based Discovery of Small Molecules Bound to T-Cell Immunoglobulin and Mucin Domain-Containing Molecule 3 (TIM-3). **2021**. *Journal of Medicinal Chemistry.* 64, 19, 14757–14772.

into a pET28b *E. coli* expression vector for tagless expression. Uniformly ^{15}N-labeled protein required for protein-observed NMR screening was expressed from BL21 (DE3) *E. coli* raised in M9 minimal media with $^{15}NH_4Cl$ as the sole nitrogen source. The TIM-3 IgV protein was purified from inclusion bodies, as previously described.[127] Briefly, insoluble inclusion bodies were first purified by a series of detergent and salt washing steps using centrifugation to pellet the inclusion bodies between washes. Washed TIM-3 inclusion bodies were denatured and solubilized in 8M urea denaturing buffer then refolded dropwise into a TIM-3 refolding buffer. The refolded TIM-3 IgV domain was dialyzed against 20 mM Tris pH 7.5, 200 mM NaCl, and 1 mM EDTA. The dialysate was clarified by centrifugation and filtration before concentration to ~1 mg/mL protein. The concentrated and dialyzed refolded protein solution was purified by size exclusion chromatography resulting in pure ^{15}N-TIM-3 IgV protein with a final yield of 4 mg per liter of culture (Figure 3-6A). Uniformly ^{15}N-labeled TIM-3 IgV domain provides a suitable ^{1}H-^{15}N SOFAST HMQC spectra for protein-observed fragment screening (0.2 mg/mL TIM-3 IgV, 24 scans, ~12min, Figure 3-6B).

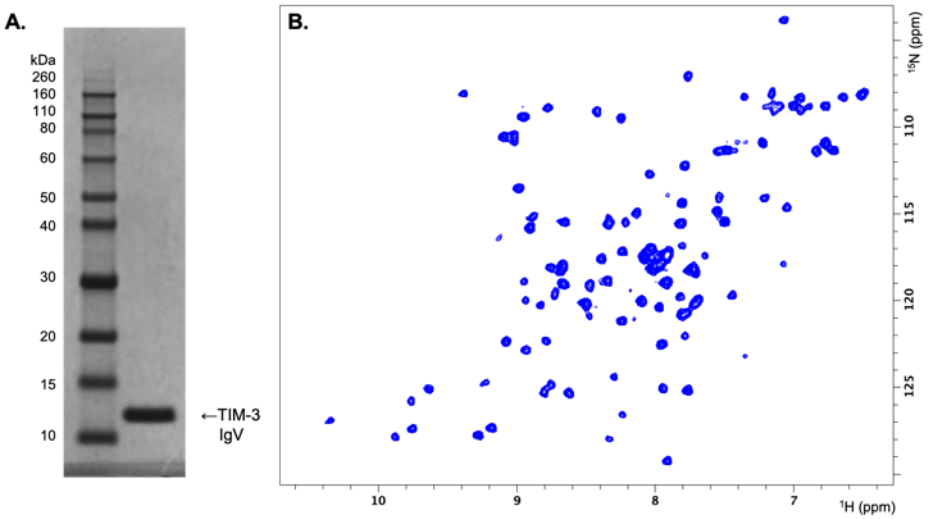

Figure 3-6. Uniformly labeled ^{15}N-TIM-3 IgV domain.
(A) SDS-PAGE gel of purified ^{15}N-TIM-3 IgV domain used for NMR experiments. (B) ^{1}H-^{15}N HSQC spectra of purified ^{15}N-TIM-3 IgV indicating a well-folded protein suitable for fragment screening.

3.2.2 *Identification of Fragment Hits that Bind to the TIM-3 IgV Domain.*

Screening of an unbiased fragment library containing 13,824 molecules has been completed by collecting protein-observed $^{1}H/^{15}N$ SOFAST-HMQC NMR spectra on uniformly ^{15}N-labeled TIM-3 IgV domain (residues 22-130) in the presence of mixtures containing 12 fragments. Fragment screening was conducted in an NMR buffer free of calcium in order to probe the uncoordinated FG-CC' cleft for ligand binding. The mixture was considered a hit if, relative to the absence of fragments, chemical shift changes were observed for backbone resonances in the HMQC spectra in the presence of fragments (Figure 3-7A). Hit mixtures were then deconvoluted as singletons to identify the fragment that binds. A total of 101 fragment hits in 12 distinct chemotype clusters were found to bind TIM-3 (Appendix I). Despite the structural diversity among the hit classes, we observed a set of resonance perturbations in the spectra that were shared between the different chemotypes, suggesting a single shared binding site.

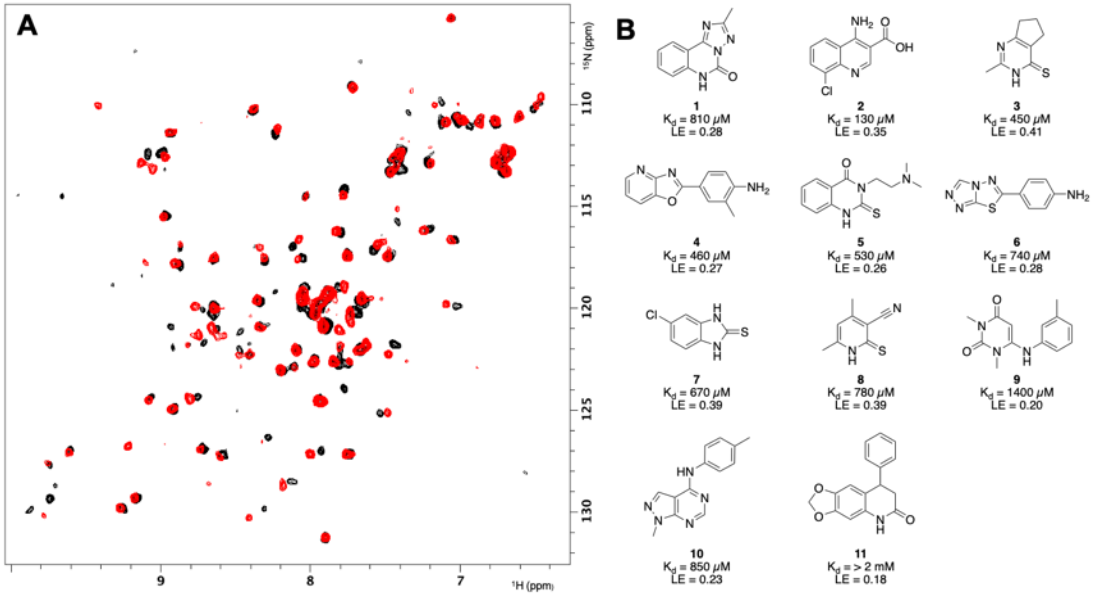

Figure 3-7. Fragment hits identified in TIM-3 screen.
(A) ^{1}H-^{15}N SOFAST HMQC spectra of TIM-3 acquired with (red) and without (black) a fragment hit. The NMR sample contained 16 μM ^{15}N-labeled TIM-3 and 800 μM fragment. (B) Representative fragment hits of different chemotype classes identified in the NMR screen.

Binding affinities for the hits were determined by SOFAST-HMQC titration experiments and range from 130 μM to >2 mM, with 18 hits having a K_d less than 1 mM with a ligand efficiency (LE) greater than 0.25 (Figure 3-7B). An overall screening hit rate for the TIM-3 IgV domain was 0.7%. Based on a statistical analysis, a protein target with greater than 0.1% fragment hit rate is considered to be druggable by small molecules[72]; therefore, our results suggest that the discovery of potent small molecule TIM-3 antagonists is feasible using fragment-based methods and structure-based design.

3.2.3 *Co-crystal structures of fragment hits bound to TIM-3.*

Obtaining structural information of fragment binding to the protein is critical to inform the design of more potent analogs. The resonance assignments of the HSQC spectra were not known at the time of our initial screen so we could not define the binding site by NMR. Instead, structural information was obtained by X-ray crystallography. Soaking methods where apo crystals are incubated with fragments which pass through solvent channels to reach their binding site can be useful with a known binding site that is not occluded by crystal packing of the apo protein. Because the binding site of these fragments were not known, co-crystallization of fragments with TIM-3 was prioritized over soaking methods. Standard protocols for co-crystallization suggest using ligand concentrations that are near 10 times the K_d to saturate the protein for the highest probability of obtaining ligand-bound structures. This can be problematic with ligands of modest affinity since saturation concentrations required, estimated 1 mM to 20 mM for fragments, may approach the ligand's solubility limit. For this reason, emphasis was placed on higher affinity fragments from different chemotype clusters. Attempts to co-crystallize TIM-3 with fragments near their respective saturation concentration in the

sparse matrix IndexHT screen (Hampton) and in a refinement screen around previously reported conditions (0.8 M KNaTartrate, 0.1 M HEPES) were largely unsuccessful.[125] It was only after 35 days of incubation that two crystals with fragment **2** (4-amino-8-chloroquinoline-3-carboxylic acid) and **3** (2-methyl-3,5,6,7-tetrahydro-4*H*-cyclopenta[*d*]pyrimidine-4-thione) were obtained from the refinement screen.

The co-crystal structure of TIM-3 with fragment **2** was solved from a crystal that formed in 0.8 M KNaTartrate, 0.1 M HEPES pH 7.5 crystallization conditions. This structure revealed a novel binding site in the C"D loop region, distal from the FG-CC' cleft active site (Figure 3-8A). Interestingly, this structure revealed a crystallographic water in the Ca^{2+} coordination site and a CC' loop conformation not seen previously in which the CC' loop is flipped down away from the FG loop and significantly broadening the FG-CC' cleft. A further examination of this CC' loop down and open cleft conformation will be discussed below. The binding of **2** at this location is mediated by a dual pi-pi stacking interaction with non-conserved residues W78 and W83, where the quinoline core is sandwiched between the two tryptophan indole side chains (Figure 3-8B). Additionally, the carboxyl substituent of the quinoline core engages with the backbone amide of R81 to form a hydrogen bond and the quinoline core N is in close proximity (<3.0 Å) with the backbone carbonyl of Y82 likely due to electrostatic interaction between the electronegative carbonyl and electropositive quinoline N. The chloro substituent of the quinoline core sits in a small hydrophobic pocket (P1) created by the hydrophobic side chains of L68, V75 and L84 (Figure 3-7B).

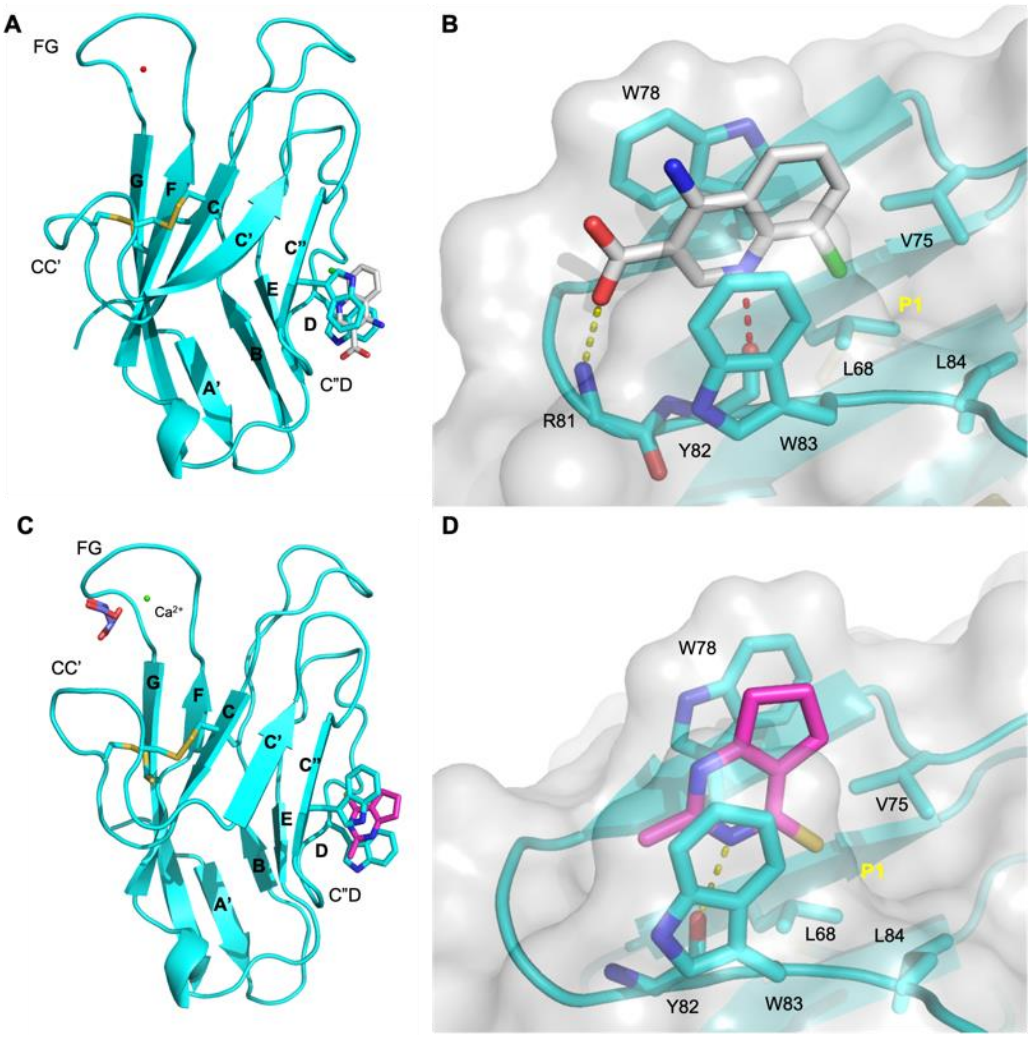

Figure 3-8. Co-crystal structures of fragment hits with TIM-3.
(A) Fragment **2** (gray-carbon capped sticks) bound to TIM-3 represented as a cartoon with labeled beta-strands and loop regions. Crystallographic water in the FG Ca^{2+} coordination site is represented as a red sphere. (B) Key hydrogen bond (yellow dashed lines), electrostatic (red dashed lines), and pi-pi stacking interaction residues of TIM-3 that interact with **2** are labeled and shown as sticks. Hydrophobic pocket (P1) is labeled. (B) Fragment **3** (magenta sticks) bound to TIM-3 represented as in (A). Ca^{2+} is represented as a green sphere in the FG-CC' cleft with bound tartrate (purple sticks). (B) Key hydrogen interaction residues of TIM-3 that interact with **3** are shown as in (B).

Similar to fragment **2**, fragment **3** binds to the same novel C"D binding site, as predicted by the shared chemical shift perturbation pattern seen in the NMR spectra. Fragment **3** co-crystals were obtained from crystallization conditions similar to **2** albeit with the addition of 10 mM $CaCl_2$. In the presence of free Ca^{2+}, the co-crystal structure of **3** contained the previously observed coordinated Ca^{2+} in the FG-CC' cleft which was also fortuitously bound to the crystallization condition component tartrate (Figure 3-8C). The

binding of **3** at the C"D site is again mediated by a dual pi-pi stacking interaction with W78 and W83 with an additional hydrogen bond formed between the backbone carbonyl of Y82 and the NH of the cyclopentapyrimidine core (Figure 3-8D). The double bonded sulfur of **3** replaces the hydrophobic space filling interaction of the chloro of **2** in P1. The C"D binding site is conformationally identical between the co-crystal structures of **2** and **3** despite the different space groups of the two structures, $C222_1$ and $P2_12_12_1$ respectively, with the one exception of a variable rotamer conformation of W78. This suggests that fragment binding at the C"D site forces this flexible loop into a lone conformation.

3.2.4 *Examining the CC' loop "down" conformation.*

The CC' loop "down" conformation seen in the co-crystal structure of fragment **2** and TIM-3 warrants a further examination as this conformation could inhibit ligand biding at the FG-CC' cleft. Comparison of the co-crystal structures of fragment **2** and **3** reveals the CC' loop down conformation significantly widens the FG-CC' cleft opening from ~15 Å to ~20 Å. If this widening is a fixed conformation due to C"D ligand biding, it could affect ligand binding at the FG-CC' cleft. The global structure of the IgV domain between structures is very similar (RMSD = 1.90 Å) aside from the position of the CC' loop (Figure 3-9A). This is noteworthy as the CC' down conformation could be an allosteric effect caused by fragment binding at the C"D site or it could be a crystallographic effect caused by crystal packing. The similarities between the two structures and the different space groups between structures suggests that the CC' loop "down" conformation may be the effect of crystal packing.

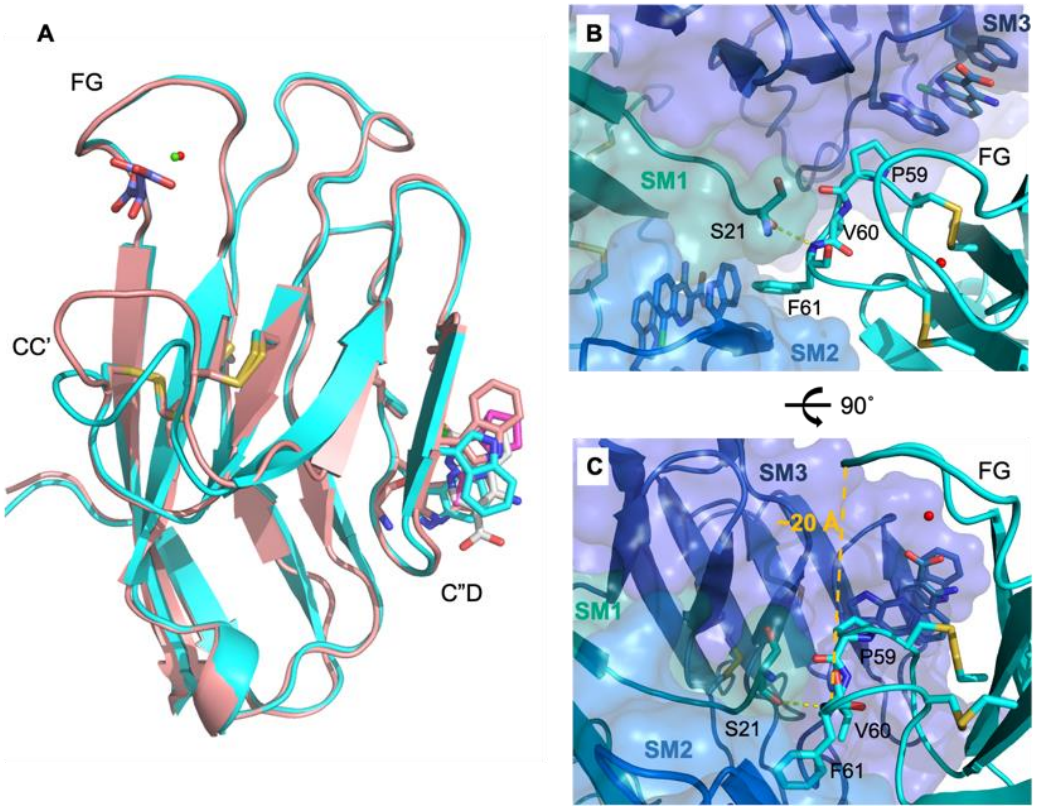

Figure 3-9. CC' loop "down" conformation is a crystallographic effect.
(A) Overlay of fragment bound structures of **2** (cyan) and **3** (peach). (B) Symmetry mates involved in crystal packing of fragment **2** co-crystal structure (cyan) are shown as ribbon cartoons with transparent surfaces in dark green (SM1), marine (SM2), and dark blue. Key interacting residues are shown as sticks and labeled. (C) 90˚ rotation of (B) showing the CC' loop "down" conformation is an effect of crystal packing. The distance between FG and CC strands is marked by an orange dashed line.

A more detailed examination of the crystal packing of the co-crystal of fragment **2** and TIM-3 reveals that symmetry mates do indeed affect the conformation of the CC' loop. Namely, the N-terminal S21 residue of one symmetry mate (SM1) forms a hydrogen bond between the backbone carbonyl and backbone amide of F61, the phenylalanine sidechain of F61 forms a face-to-edge pi-pi interaction with C"D site residue W78 of a second symmetry mate (SM2), and P59 makes forms hydrophobic interactions with the C"D site residue W83 of a third symmetry mate (SM3) (Figure 3-9B). These interactions between the CC' loop and three symmetry mates contribute to pull the CC' loop into the "down" conformation widening the FG-CC' cleft (Figue 3-9C). The CC' loop "down" structure highlights the inherent loop flexibility of the FG-CC' cleft that allows for the

accommodation of both small molecule and protein ligands alike, but is also an undesirable feature of this site for drug development.

3.2.5 *Optimization of fragment 1 triazoloquinazolinone series.*

The assignments of TIM-3's backbone resonances were not yet known at the time of our initial fragment screen, but the shared set of resonance perturbations upon fragment binding suggested a shared single binding site, which we have now identified as the C"D site. Analogs from the primary hits were synthesized or purchased and screened by NMR as previously described. Compounds that derived from the initial fragment **1** were found to be the most active. Limited medicinal chemistry resources necessitated the prioritizing of a chemical series for hit to lead optimization. Fragment **1** (2-methyl-[1,2,4]triazolo[1,5-*c*]quinazolin-5(6*H*)-one) was chosen as a chemically tractable starting point with multiple expandable substitution vectors and a combined K_d and LE in the top 10% of identified hits.

Analogs containing various hydrophobic substitutions at the 2-, 8-, and 9-positions of Fragment **1** were synthesized to probe the binding site. The K_d's of twelve representative compounds reported in Table 3-1 were determined by NMR titration experiments. Aliphatic R1 groups were tolerated at the 2-position, and the 2-isopropyl group in **12** exhibited 2-fold increased affinity compared to the methyl analog **1**. However, compound **13** containing the 2-phenyl group exhibited reduced affinity, and the K_d could not be measured reliably due to limited aqueous solubility. Substitutions at the 9-position of the triazoloquinazolinone core were highly beneficial and resulted in an affinity enhancement. A methoxy group at the 9-position of **14** was tolerated compared to **12**. The addition of the bromo group of **15**, led to a significant increase in affinity

(approximately 20-fold) over **1**, but the exact K_d determination was complicated by low aqueous solubility. The more hydrophilic pyrazolyl moiety was introduced at the 9-position (compound **16**), and its K_d was determined to be 40 μM with enhanced the aqueous solubility. The 9-(3'-methylpyridin-4-yl) analog **17** also exhibited a similar affinity to TIM-3 compared to compound **16**. We also observed that the 8-chloro substitution in compound **18** and **19** led to a 9 and 3.7-fold increase in binding affinity compared to their parent **1** and **12**, respectively.

Table 3-1. Optimization of the triazoloquinazolinone series.

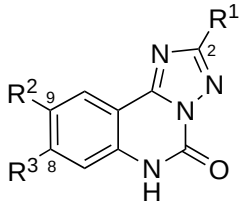

Compound	R^1	R^2	R^3	NMR K_d (μM)[a]
1	Me	H	H	810
12	*i*-Pr	H	H	330
13	Ph	H	H	> 2000[b]
14	*i*-Pr	MeO	H	250
15	Me	Br	H	~40[b]
16	Me		H	40
17	Me		H	50[b]
18	Me	H	Cl	90
19	*i*-Pr	H	Cl	90
20	*i*-Pr	Cl	Cl	40
21	Me	Br	Cl	40
22	Me		Cl	< 10[c]

[a]SOFAST NMR titration experiments were used to determine K_d.
[b]K_d determination complicated by solubility limits of compound.
[c]Compound exhibited intermediate exchange in NMR suggesting single digit µM affinity.

Affinity enhancement by an individual substitution was additive when the beneficial groups were combined. Compound **20** showed a 2-fold increase in affinity by introduction of the 9-chloro group compared to the parent **19**. The potency of compound **21** was comparable to **15**. Finally, incorporation of the 3-methylpyridin-4-yl group in **22** exhibited the intermediate exchange phenomenon in NMR indicating the binding affinity is beyond the lower limit of detection for the method (single-digit μM or better).[128] Affinity improvements through SAR by NMR represented a near 80-fold gain in potency from **1**. Compound **22** was used as an initial chemical probe to obtain X-ray structural information to guide further optimization.

3.2.6 *Co-crystal structure of **22** and TIM-3 reveal critical intermolecular contacts.*

To determine how these compounds bind to TIM-3 and guide the design of additional analogs, we obtained the co-crystal structure of **22** bound to TIM-3. Unsurprisingly, the compound binds the previously identified novel C”D loop binding site (Figure 3-10A). The binding of **22** at this location is mediated by a dual pi-pi stacking interaction with W78 and W83, where the [1,2,4]triazolo[1,5-*c*]quinazolin-5(6*H*)-one core is sandwiched between the two tryptophan indole side chains (Figure 3-10B). Additionally, the carbonyl oxygen and NH of the quinazolin-5(6*H*)-one moiety creates a hydrogen bonding network with the backbone amide of R81 and the backbone carbonyl oxygen of Y82, respectively. The dual pi-pi stacking and H-bonding network combine to constitute the critical binding elements to anchor the triazoloquinazolinone core unit. The 8-chloro substituent of **22** fills the small hydrophobic pocket, P1, on the bottom of the binding site generated by L68, V75 and L84 side chains (Figure 3-10B). The 3-methylpyridine-4-yl group at the 9-position adopts a near orthogonal conformation to the tricyclic core unit

and provides a hydrophobic shield atop the binding site. The 3-methyl substituent may provide conformational stability of the pyridine to the near perpendicular plane (torsion angle = 111.9˚). The electron density of the 3-methylpyridine-4-yl group also suggests that 3-methyl moiety prefers to orient toward to W83 (Figure 3-10C).

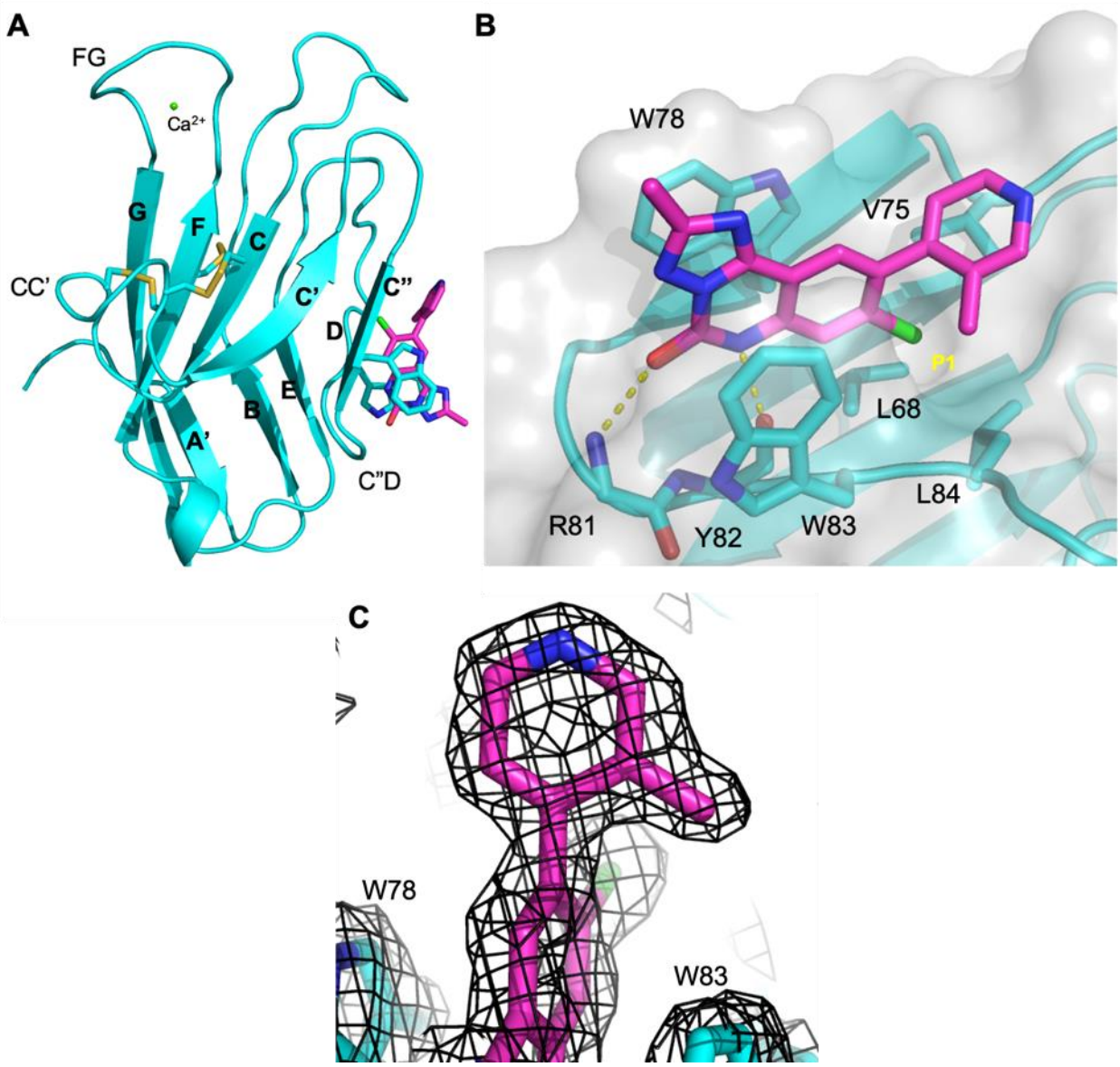

Figure 3-10. X-ray co-crystal structure of 22 bound to TIM-3.
(A) Compound **22** (magenta-carbon capped sticks) bound to TIM-3 represented as a cartoon with labeled beta-strands and loop regions (PDB ID: 7M3Y). (B) Key hydrogen bond (yellow dashed lines) and pi-pi stacking interaction residues of TIM-3 that interact with **22**. Hydrophobic pocket (P1) is labeled. (C) 2Fo-Fc electron density map (contoured to 1.5 σ) of **22** highlighting the orientation of the 3-methylpyridine-4-yl group.

3.2.7 *Development of an FPA competition assay.*

With our higher affinity compounds exhibiting intermediate exchange by NMR, it became impractical to solely rely on NMR when attempting to rank-order new analogs. Development of a new reliable biochemical assay that could measure nanomolar binding affinities was required for the advancement of SAR development at the C"D site. The new assay required a fluorescent probe with high binding affinity, but there were no known endogenous or small molecule ligands for the C"D site of TIM-3 protein. Therefore, we set out to design a probe molecule from compound **22**.

The co-crystal structure of compound **22** bound to Tim-3 reveals that the 2-methyl substitution is positioned outside of the binding pocket and appeared to be an ideal position to introduce a fluorescein label to generate a small-molecule probe for biochemical assays. Using this structural information, a small-molecule probe **23** (Figure 3-10A) was prepared by incorporating the (2-(6-hydroxy3-oxo-3H-xanthen-9-yl)benzoic acid fluorescein label through a methylamine linker, which replaces the 2-methyl moiety of parent compound **22**. Indeed, this probe exhibited a K_d = 2.0 μM in FPA-based equilibrium binding assay as a function of TIM-3 concentration (Figure 3-11A). The corresponding parent compound **22** was tested in a competitive binding experiment to test its ability to displace probe **23** from TIM-3 (Figure 3-11B). An experimental IC_{50} of 53 μM was determined from the competition assay. This IC_{50} can be converted to an estimated K_i of 4.9 μM which was in good agreement with the K_d of the labeled probe and the suggested single digit μM affinity of **22** from intermediate exchange in NMR titration.

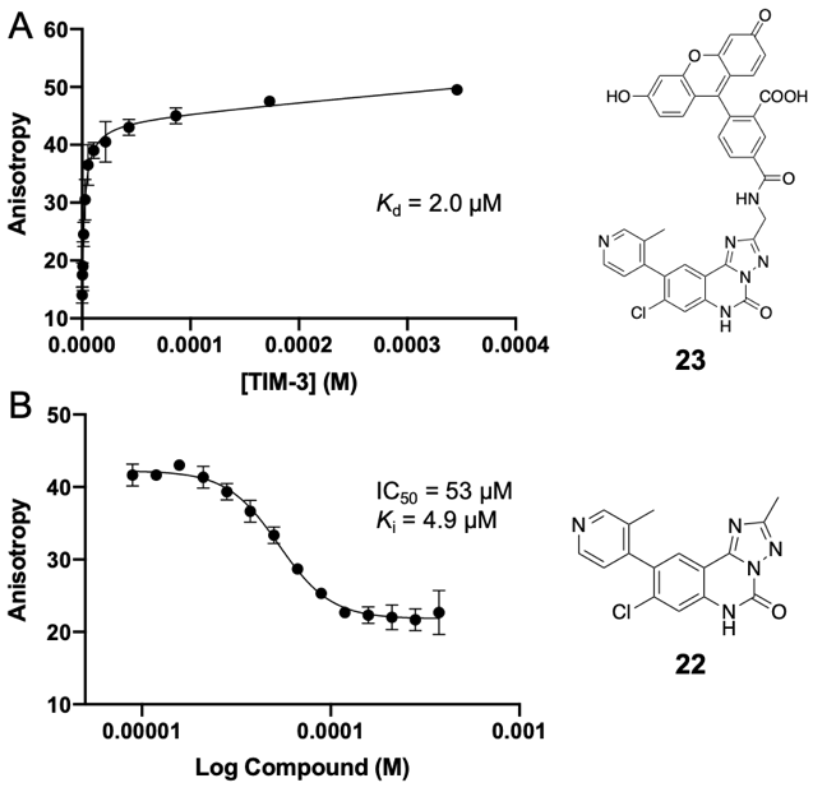

Figure 3-11. Development of FPA competition assay.
(A) Saturation binding curve of the fluorescent small-molecule probe **23** to TIM-3. (B) Displacement of probe **23** from TIM-3 by parent compound **22**.

3.2.8 *Optimization of 9-aryl group.*

To further improve the binding affinity of compound **22**, we expanded the SAR at the 9-position by introducing a variety of substituted heteroaryl groups. Thirteen representative compounds reported in Table 3-2 were evaluated by FPA using the probe **23** to determine a binding affinity (K_i) to TIM-3. The 2-methylphenyl analog **24** had a K_i = 1.6 μM, a 3-fold improvement but had reduced aqueous solubility. Substitutions at the 3-position of the pyridyl group were well tolerated and removal of the 3-methyl (**25**) and introduction of 3-methoxy (**26**) resulted in marginal improvement in binding affinity (2- and 3-fold, respectively) compared to **22**. We expanded the heterocycles to include indole and indazole classes of compounds to explore the effect of an additional H-bond donor. The 4-indole (**27**), the 1*H*-pyrrolo[2,3-*b*]pyridine (**28**) and the 5-methyl-1*H*-indazole (**29**)

analogs were well tolerated at this position exhibiting a 2.5-3-fold increase in affinity compared to **22**. These results suggest that additional H-bond donors and nitrogen atoms in **28** and **29** did not play important roles in binding interactions for these compounds. The co-crystal structure of **22** revealed the nearby charged sidechains of residues D74 and R99, for those could be reached from the 9-aryl group to elicit favorable electrostatic interactions. Compound **30** and **31** with the 4-aminophenyl and the 4-amino-2-methylphenyl group, respectively, were designed to reach the D74 residue. However, these compounds exhibited a similar affinity compared to their close analogs **25** and **24**, suggesting the added 4'-amino group played a neutral role in binding. Additional improvement in affinity was observed in analogs that contain 4-phenylmethanesulfonamide substitution, which was intended to reach both the D74 and R99 residues. The affinity of **32** improved by 2-fold compared to **30**, and the electron donating 3-methoxy group of **33** slightly improved the affinity to K_i = 0.97 μM. As previously observed, the 2-chloro and 2-methyl groups were added as conformational constraints in **34** and **35**, and the compounds had measured affinities of K_i = 0.55 μM and 0.75 μM, respectively. Compound **34** was the most potent compound from this set of analogs representing a 9-fold improvement over **22**.

Table 3-2. Optimization and SAR of the aryl-substituted triazoloquinazolinone core.

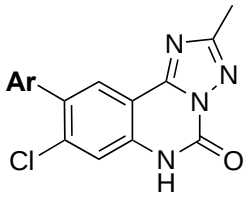

Compound	Ar Structure	FPA K_i (μM)[a]	Compound	Ar Structure	FPA K_i (μM)[a]
22	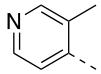	4.9 ± 0.9	**30**	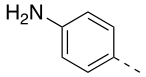	2.6 ± 0.1
24		1.6 ± 0.2	**31**	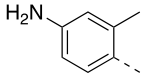	1.5 ± 0.2
25	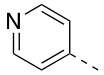	2.1 ± 0.3	**32**	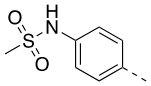	1.3 ± 0.1
26	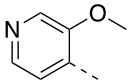	1.5 ± 0.3	**33**	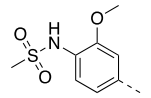	0.97 ± 0.09
27	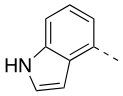	1.8 ± 0.2	**34**	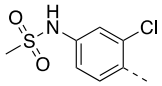	0.55 ± 0.01
28	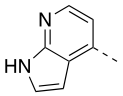	2.2 ± 0.1	**35**	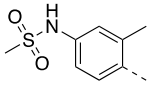	0.75 ± 0.03
29	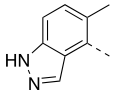	2.3 ± 0.3			

[a]FPA K_i values represent two independent replicates ± standard deviation and were evaluated by displacement of probe **23**.

3.2.9 *Improvement of the FPA competition assay.*

It was necessary to expand the lower detection limit of our competition assay as our compounds were getting more potent. A new higher affinity small-molecule probe **SP2** was prepared by using compound **34**. This probe exhibited a K_d = 250 nM in an FPA-based equilibrium binding assay as a function of TIM-3 concentration (Figure 3-12A). The corresponding parent **34** was tested in a competitive binding experiment and exhibited a K_i = 200 nM (Figure 3-12B) under the new condition using the **SP2** probe, that was in good agreement with K_d of the **SP2** probe and K_i (540 nM) determined in the initial assay.

This new higher-affinity small-molecule probe **SP2** effectively lowered total protein concentration by a 4.6-fold and expanded the low detection limit for the new FPA assay method, which was used to test subsequent potent analogs.

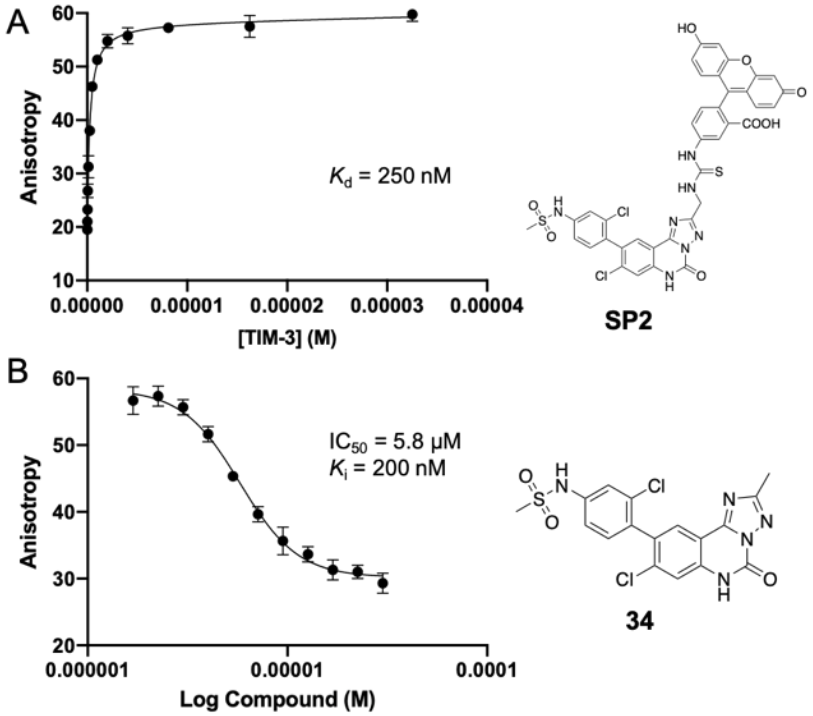

Figure 3-12. Improvement of FPA competition assay with higher affinity probe.
(A) Saturation binding curve of the fluorescent small-molecule probe **SP2** to TIM-3. (B) Displacement of probe **SP2** from TIM-3 by parent compound **34**.

3.2.10 *X-ray co-crystal structure of **34** bound to TIM-3.*

To further understand the additional binding interactions, we obtained a co-crystal structure of **34** bound to TIM-3. All the C"D binding site interactions previously discussed for the co-crystal structure of **22** are intact with **34** (Figure 3-13A). The increased binding affinity of **34** can be attributed to an additional H-bonding network at the binding site between the sulfonamide substituent with sidechains of residues C" strand residue D74 and D strand residue R99. Specifically, the sulfonamide NH and the sulfonyl oxygen are positioned within hydrogen bonding distances with the carboxylate of D74 and the guanidinium of R99, respectively (Figure 3-13B). The additional binding interactions of

sulfonamide do not significantly alter the conformation of the C”D binding site compared to other compounds and fragments.

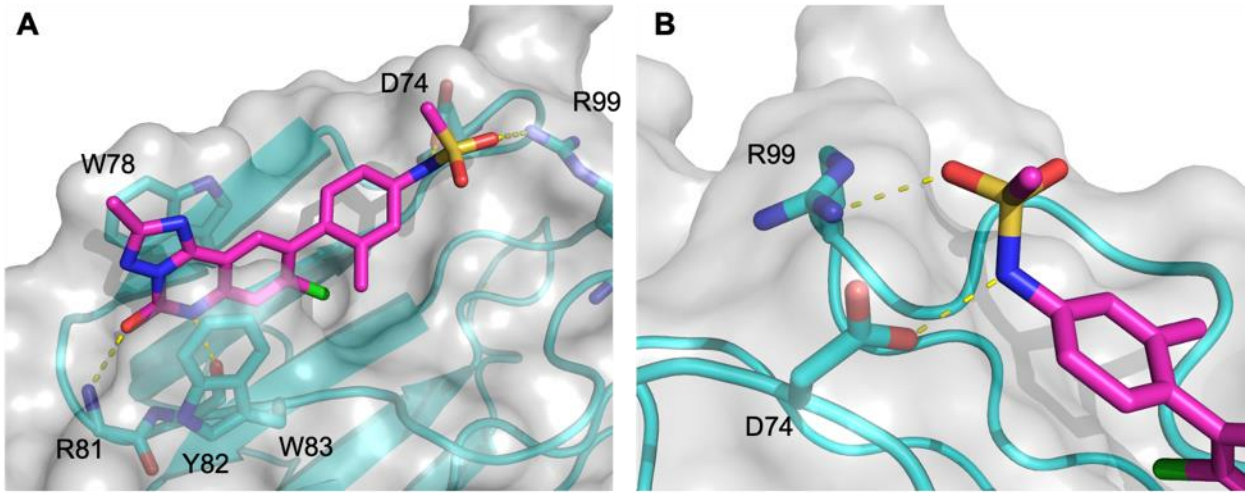

Figure 3-13. X-ray co-crystal structure of 35 bound to TIM-3 (PDB ID: 7M3Z).
(A) Compound **35** (magenta-carbon capped sticks) bound to Ca^{2+} bound TIM-3 represented as a cartoon with semi-transparent electrostatic potential surface with key H-bond (yellow dashed lines) and pi-pi stacking interaction residues of TIM-3 shown. (B) Additional H-bond network (yellow dashed lines) residues of TIM-3 that interact with **35**. Change hydrogen bond colors

3.2.11 *Optimization of sulfonamide containing compounds.*

Binding affinities of compounds **32**, **34**, and **35** along with the newly prepared 2-fluoro analog **36** were measured using the new FPA competition assay condition with the probe **SP2** to identify the optimal 2-substituent (Table 3-3). The addition of small hydrophobic groups at the 2-position of phenyl moiety was beneficial for potency, as compound **34** - **36** exhibited 1.3 to 2.4-fold higher affinity to the unsubstituted analog **32**. The smaller 2-fluoro substitution of **36** was less effective in increasing the affinity compared to **34** and **35** with 2-chloro and 2-methyl group, respectively. The 2-methyl analog **35** showed the highest affinity of K_i = 156 nM and used in the final set of compounds as a parent molecule.

Table 3-3. Optimization and SAR of sulfonamide-containing triazoloquinazolinone series.

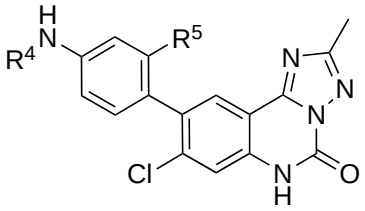

Compound	R^4	R^5	FPA K_i (nM)[a]
32		H	500 ± 100
34		Cl	204 ± 2
35		Me	156 ± 5
36		F	287 ± 7
37		Me	164 ± 2
38	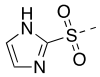	Me	70 ± 20
39	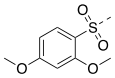	Me	110 ± 10
40		Me	440 ± 50

[a]FPA K_i values represent two independent replicates ± standard deviation and were evaluated by displacement of probe **SP2**.

The co-crystal structure of **35** bound to TIM-3 was then used to guide further compound design, in which the methyl moiety of the sulfonamide had an appropriate vector to accommodate further derivatization of the group to elicit additional interactions with nearby residues in TIM-3. The co-crystal structure also suggests that an additional H-bond interaction is feasible with the sidechain carboxylate of D74 by incorporating H-bond donor substituting the methyl group of sulfonamide. The *N*-methylsulfonylurea **37** was prepared but showed a similar affinity to parent **35**. The 1*H*-imidazole-2-sulfonamide **38** with the extended H-bond donor exhibited a near 3-fold improvement in affinity (K_i = 70 nM). The electron rich 2,4-dimethoxysulfonamide containing **39** had a modest increase in affinity compared to **35**. Compound **39** suggested that a larger substituted phenyl group

can be accommodated at the position, and increased electron density to the sulfonamide may strengthen the H-bond interactions with D74 and R99 of TIM-3. Compound **40** was made to test the contributions of the sulfonyl group to the overall affinity. Removal of the group resulted in a 5-fold loss in affinity, which was likely attributed to the loss of the H-bond interaction with R99 and modulation of the aniline NH properties for the interaction with D74.

3.2.12 *X-ray co-crystal Structure of **38** Bound to TIM-3.*

The co-crystal structure of **38** bound to TIM-3 was solved to better understand the observed gain in affinity for the compound. The critical binding elements to the C"D binding site previously observed in the co-crystal structures of **22** and **34** were maintained for **38**. The dual pi-pi stacking interaction with W78 and W83, H-bond network with R81 and Y82, and the sulfonamide induced H-bond network with D74 and R99 was observed in the co-crystal structure of **38 (**Figure 3-14A). The co-crystal structure also revealed an additional H-bond between the imidazole NH and the carboxylate side chain of D74. This additional binding interaction could further stabilize the complex (Figure 3-14B) and might contribute to the 3-fold binding affinity enhancement found in **38** compared to compound **35.** Similar to 35, the additional binding interactions of imidizaloe do not significantly alter the conformation of the C"D binding site compared to other compounds and fragments. Compound **38** is our current best-in-class compound with a K_i = 70 nM representing an 11,500-fold improvement in affinity over our initial fragment hit.

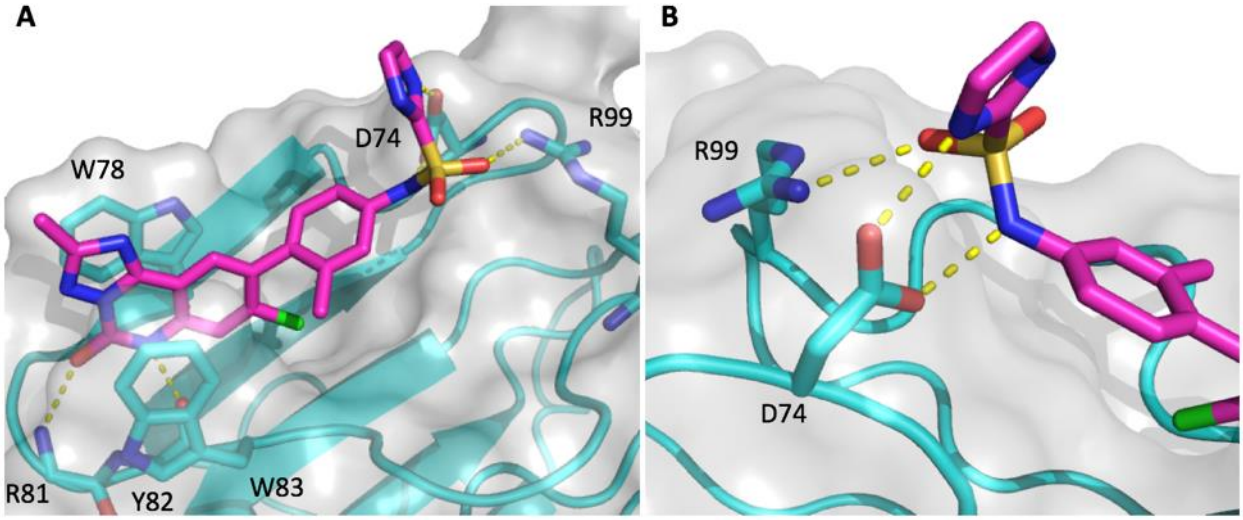

Figure 3-14. X-ray co-crystal structure of 38 bound to TIM-3 (PDB ID: 7M41).
(A) Compound **38** (magenta-carbon capped sticks) bound to Ca^{2+} bound TIM-3 represented as a cartoon with semi-transparent electrostatic potential surface with key H-bond (yellow dashed lines) and pi-pi stacking interaction residues of TIM-3 shown. (B) Additional H-bond network (yellow dashed lines) residues of TIM-3 that interact with **38**.

3.2.13 *Profiling of **35** and **38** TIM-3 ligand inhibition.*

The C"D site has previously not been directly associated with ligand binding. However, this does not preclude our compounds from having an allosteric inhibitory effect against ligand binding. We sought to assess the inhibitory capacity of **35** and **38** against natural TIM-3 ligands PtdSer, galectin-9, and CEACAM1.

We first wanted to see if compound binding at the C"D site would deter PtdSer binding at the FG-CC' cleft. We used the short acyl chain PtdSer analog 6:0 PtdSer (Avanti Polar Lipids) that interacts with the FG-CC' cleft in a Ca^{2+}-dependent manner as an analog for ligand binding at the FG-CC' cleft. With saturating levels of compound **35**, resonance peaks likely belonging to the FG-CC' cleft are perturbed upon addition of 6:0 PtdSer suggesting that the binding of **35** at the C"D site does not have an allosteric effect against PtdSer binding (Figure 3-15A). This is not a surprising outcome given the distance between the two sites and the inherent flexibility of the FG-CC' (Figure 3-15B). Furthermore, this experiment highlights that the CC' loop down seen in the crystal

structures of most C"D site compounds is in fact a crystallographic artifact due to crystal packing and not an allosteric effect due to binding.

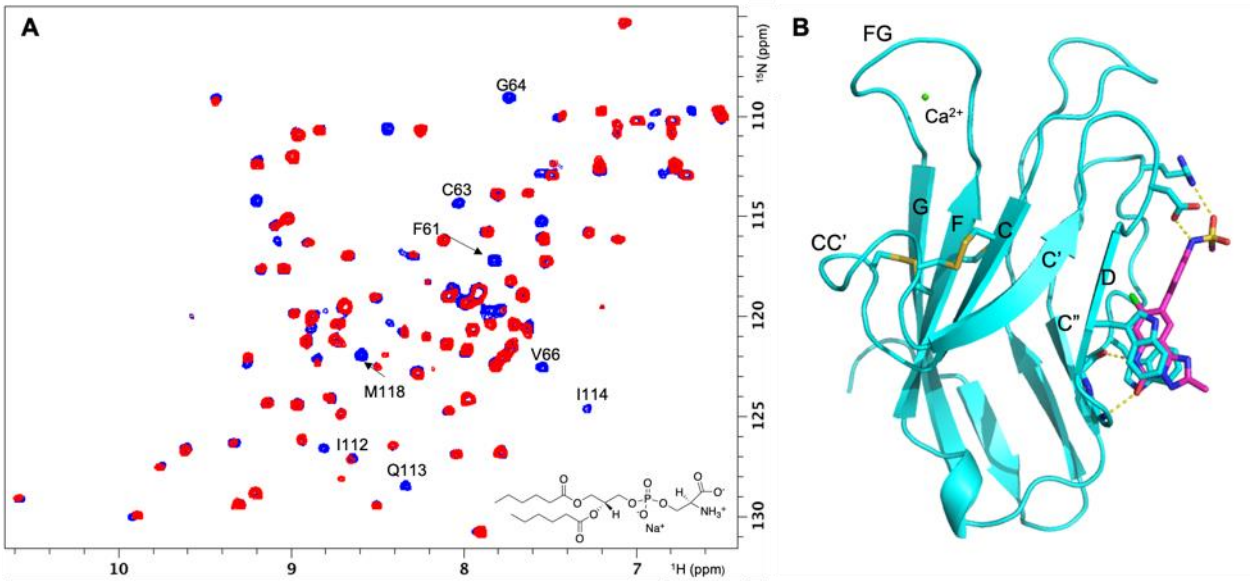

Figure 3-15. The FG-CC' cleft and C"D loop are two distinct binding sites.
(A) Overlayed ^{1}H-^{15}N SOFAST HMQC spectra of TIM-3 IgV domain with 200 µM **35** and 10 mM $CaCl_2$ (blue) and with the same conditions and 630 µM 6:0 PtdSer (red). Prominent chemical shift perturbations of FG-CC' cleft and CC' loop residue signals are labeled and the structure of 6:0 PtdSer is displayed in the inset. (B) Compound **35** (magenta-carbon capped sticks, hydrogen bonds depicted as yellow dashed lines) bound to TIM-3 represented as a cartoon with labeled beta-strands and loop regions.

Galectin-9 binding to TIM-3 leads to phosphorylation of intracellular Y256 and Y263, a release of bound HLA-B associated transcript 3 (Bat3), and promotes TIM-3-mediated inhibition of T cells. This process will cause an influx of calcium into the cell and the induction of apoptosis. Using galectin-9-induced apoptosis of activated TIM-3^{+} T cells as an assay end point, we tested our compounds' ability to disrupt TIM-3/galectin-9 binding. T cells isolated from peripheral blood monocytes (PBMC) were activated with CD3/CD28 magnetic beads and assessed for TIM-3 expression. Across experiments, we found that CD3/CD28 activation led to 40-80% TIM-3^{+} T cells (Figure 3-16A). Alone, **35** and **38** showed no signs of cytotoxic effects on activated TIM-3^{+} T cells (Figure 3-16B). Unfortunately, **35** and **38** did not rescue activated T cells from galectin-9-induced apoptosis at all tested compound concentrations (Figure 3-16C). This is not a surprising

outcome considering galectin-9 has been shown to primarily bind N-linked oligosaccharides of the IgV and not the IgV domain itself.

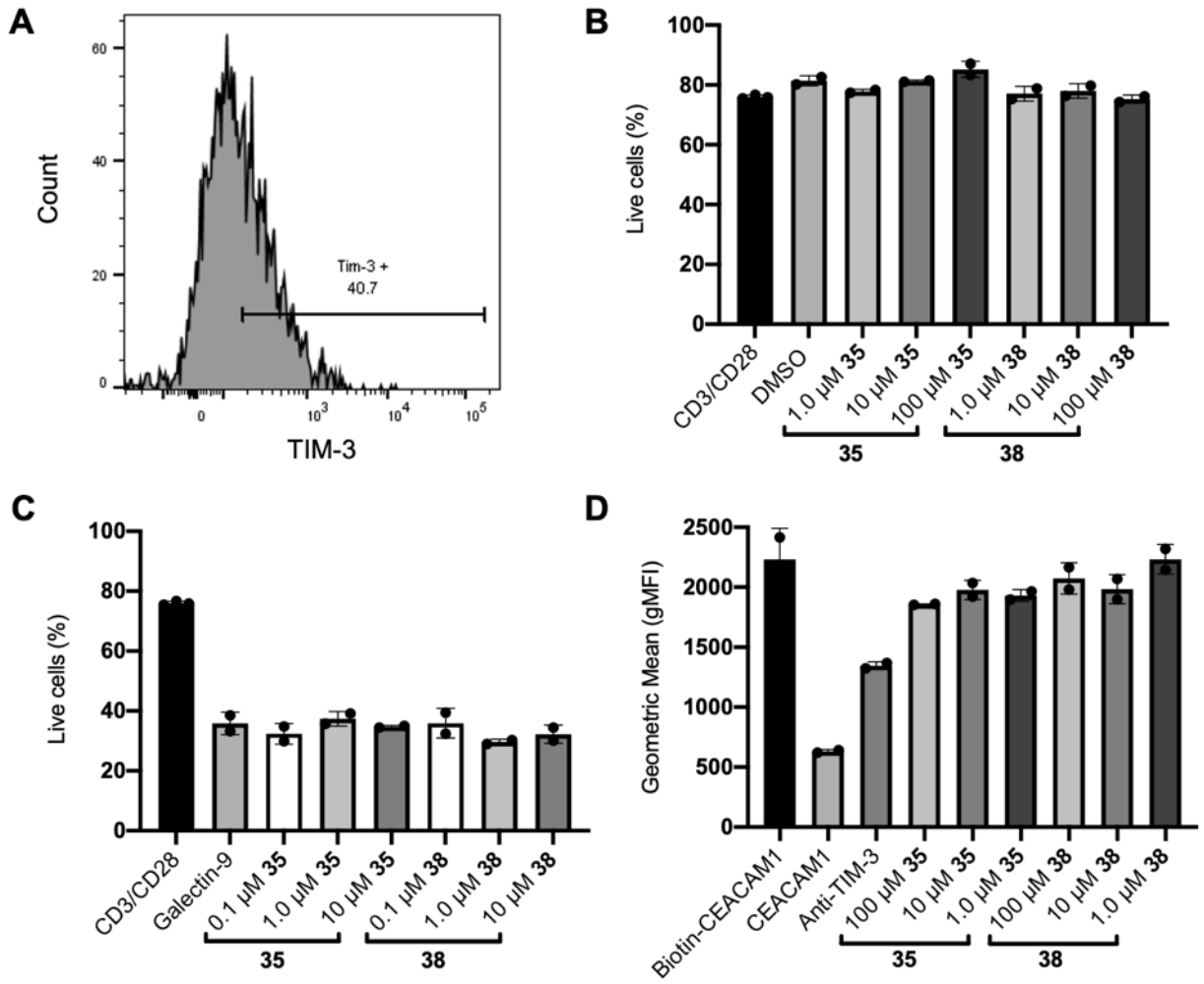

Figure 3-16. TIM-3 ligand binding inhibition assays.
(A) T cells stained with anti-TIM-3. The number above the bracketed line indicates the percentage of cells positive for TIM-3 staining. (B) Activated T cells were incubated with **35** and **38** did not display cytotoxicity. (C) Activated TIM-3$^+$ T cell galectin-9-induced apoptosis assay with various concentrations of **35** and **38** analyzing the potential for these compounds to inhibit TIM-3/galectin-9 binding and rescue activated T cells from apoptosis. (D) Biotinylated CEACAM1 binding assays with activated TIM-3$^+$ T cells testing **35** and **38** inhibition of TIM-3/CEACAM1 binding at various concentrations.

CEACAM1 binding to TIM-3 has been shown to be mediated by interaction with the FG-CC' cleft making it well suited to test our compounds' ability to inhibit protein ligands of the FG-CC' cleft. In our hands, CEACAM1 alone did not induce the Recombinant biotinylated CEACAM1 was incubated with activated TIM-3$^+$ T cells and

stained with FITC-streptavidin (Figure 3-16D). An antiTIM-3 antibody positive control reduced biotinylated CEACAM1 binding by ~40%, however a large proportion of T cells still displayed CEACAM1 engagement. This is likely due to homophilic interactions between biotinylated CEACAM1 and CEACAM1 expressed on activated T cells, which has been previously reported.[129–131] Compounds **35** and **38** did not significantly reduce biotinylated CEACAM1 engagement with activated T cells, and failed to replicate the degree of inhibition seen by the positive control anti-TIM-3 (Figure 3-16D). This experiment may have been confounded by homophilic CEACAM1 interactions, but it is clear that compounds **35** and **38** did not perform similarly to antiTIM-3. I would like to thank Gabriel Rodriguez and Dr. Michael Korrer from Dr. Young Kim's lab for their help with these experiments.

3.2.14 *Compound **38** rigidifies the C"D loop.*

Our lab and others have been unable to assign the backbone NMR resonances for the C', C", and D strands through triple resonance experiments of $^{15}N/^{13}C$ labeled TIM-3 IgV domain.[95] The lack of adequate signal intensity for these residues suggests that this region of the protein is conformationally dynamic *in vitro*. The co-crystal structure of **38** with TIM-3 shows a rigidified C"D loop and, consequently, ^{1}H-^{15}N HSQC spectra of TIM-3 with a saturation concentration of **38** (200 µM) results in the appearance of several backbone resonance signals previously unidentified and unassigned (Figure 3-17A). It can be deduced that these signals belong to residues in the C"D loop and further confirms that our compounds are capable of rigidifying C"D *in vitro*. Furthermore, NMR peak chemical shift analysis, expressed as $[(\Delta Hcs/0.1\ ppm)^2 + (\Delta Ncs/0.5\ ppm)^2]^{1/2}$, of assigned backbone resonances shows that several resonances are perturbed upon C"D ligand

binding (Figure 3-17B). More specifically, resonances belonging to the B-C loop, C strand, first helix, E strand, F strand, and G strand all showed significant combined chemical shift changes suggesting a significant protein conformational change upon C”D ligand binding (Figure 3-17C). Although the biological consequences of rigidifying the C”D loop are unknown, it is clear that the compounds designed herein engage and stabilize the C”D binding site resulting in an altered TIM-3 IgV domain conformation.

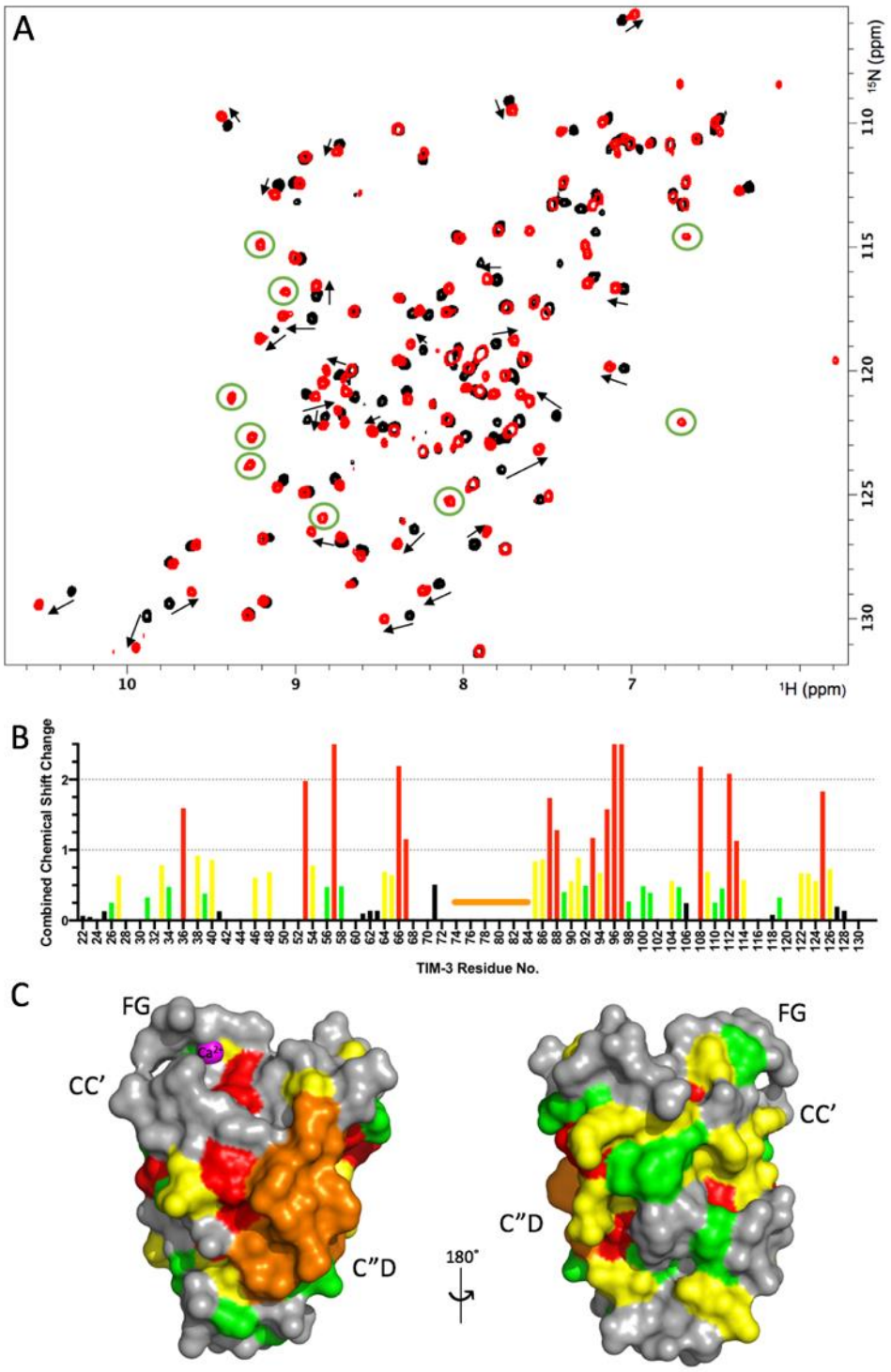

Figure 3-17. Chemical shift perturbation analysis of TIM-3 bound to 38.
(A) Overlaid ^{1}H-^{15}N HSQCs of TIM3 apo (black) and with 200 µM compound **38** (red). Resonance peak shifts (black arrows) are shown and resonance peak appearances (green circles) are highlighted upon binding of compound **38**. (B) Plot of peak shifts showing ^{1}H–^{15}N HSQC combined chemical shift changes index of TIM-3 upon binding with **38**. The data columns are colored according to degree of index changes (red > 1.0; yellow > 0.5; green > 0.25) and C"D residues that lack resonance assignments are indicated by an orange bar. (C) Chemical shift changes of TIM-3 backbone amides induced by **38** binding, mapped on

to TIM-3 crystal structure (PDB ID: 6DHB) surface and colored by degree of index changes as in (B). The opposite AGFCC′C″ and BED faces are shown in the left and right panels, respectively, with the FG, CC′, and C”D loops labeled. Ca^{2+} bound in the FG-CC’ cleft is colored magenta.

3.3 Conclusions

Here we demonstrated the fragment-based discovery and design of compounds that bind to TIM-3 with 70 nM affinity. From an analysis of SAR and structure-based design, we substantially improved the affinity from a high µM initial weak-binding fragment hit to a double-digit nM binding drug-like compound. These studies resulted in a small-molecule ligand for TIM-3 that exhibited a binding affinity increase of 11,500-fold from the initial fragment hit.

Structural studies were important to identify a novel binding site on TIM-3 involving the C”D loop and to guide the design of analogs. Our efforts resulted in a high-affinity ligand for TIM-3, however all avenues for triazoloquinazolinone series optimization were not exhausted. In particular, substitution of the 2-position on 4-phenylmethanesulfonamide was limited and an examination of structural data would identify this as a potential site for further ligand-protein interaction. Compound solubility was a consistent problem during NMR and FPA analysis. Structural data shows that the 2-position of the triazoloquinazolinone core is directly solvent accessible and has no binding interaction, therefore, this position can be utilized to make physicochemical property modifications when needed. The structural and SAR data obtained on this series can be used to design more potent TIM-3 ligands with better pharmaceutical properties.

With a high-affinity compound, we can now investigate the pharmacological relevance of the C”D binding site. As previously mentioned, the majority of natural TIM-3 ligands interact with the FG-CC’ cleft and, therefore, this would be the most likely site to target to achieve inhibition of TIM-3 activity. Indeed, a recent study suggested that

therapeutic antibodies capable of exhibiting optimal anti-tumor responses target TIM-3 at the FG-CC' cleft.[132] The C"D site has previously not been directly associated with ligand binding or a significant role in TIM-3 activation. However, this does not preclude our compounds from having an allosteric inhibitory effect against ligand binding. Furthermore, the specific structural dynamics that underlie TIM-3 activation upon natural ligand binding remain elusive. It has been established that ligand binding leads to the phosphorylation of Y265 and Y272 on the cytoplasmic tail and further downstream signaling that promotes T cell inhibition.[119,120] However, it is still unclear if activation is the result of conformational changes in the IgV domain, or receptor oligomerization, or a combination of these events. Our experiments did not show signs of significant ligand inhibition, however these studies were not exhaustive and, given the complicated biology of TIM-3, further analysis of ligand interruption is warranted.

Rigidification of the C"D loop upon compound binding results in a conformational change of the IgV domain that could allosterically inhibit ligand binding or directly induce an inactive or active state. Further studies are needed to analyze downstream signaling events upon compound binding that may lead to TIM-3 inhibition or activation. The compounds presented here and future analogs will be important tool compounds to further probe the C"D site for TIM-3 immune modulation.

3.4 Methods

3.4.1 *Protein expression and purification.*

The gene encoding the IgV domain of human Tim-3 (residues 22-130) was synthesized with codon optimization for *E. coli* overexpression (GenScript). The construct was inserted into a vector (pET-28b+) for a tagless expression of the IgV domain. The

IgV domain was overexpressed from BL21 (DE3) Gold strain *E. coli* into inclusion bodies. Protein production was induced with 1 mM IPTG when cultures reached an OD600 of 0.8 and harvested after 4 h at 37˚C or overnight expression at 25˚C. Isotopically-labeled Tim-3 was prepared in M9 minimal media containing $^{15}NH_4Cl$. For resonance assignments, ^{13}C-glucose was used at 0.2 (w/v)% final concentration. The TIM-3 IgV domain was purified as previously described.[95] Briefly, cell pellets containing expressed human TIM-3 IgV were thawed and suspended in buffer before lysis by high pressure homogenizer. The lysate was centrifuged and TIM-3 was retained in inclusion bodies in the insoluble fraction. The pellet was washed by resuspension in buffer plus 0.1% Triton X-100, homogenized by sonication, and centrifuged. The insoluble fraction was washed and pelleted as described above in a high salt buffer containing 1.5 M NaCl, and then once more in the original buffer. The washed inclusion body pellet was weighed and dissolved in a buffer containing 8 M urea at room temperature for 1 hour before centrifugation to remove debris. Refolding of Tim-3 IgV was done by rapid dilution by drop-wise (~1 mL/min) addition of solubilized inclusion bodies into 10-25 volumes of refolding buffer containing 100 mM Tris pH 8.3, 0.4 M L-arginine, 2 mM EDTA, 2 mM reduced glutathione, and 0.2 mM oxidized glutathione. After incubating the refolding mixture overnight at 4˚C, it was dialyzed into a buffer of 20 mM Tris pH 7.5, 200 mM NaCl, and 1 mM EDTA. The dialysate was clarified by centrifugation and filtration before concentrated and loaded onto a HiPrep 26/300 Sephacryl S-75 column for size exclusion chromatography in an NMR buffer of 50 mM phosphate pH 7 and 25 mM NaCl for NMR-based screening.

The gene encoding the IgV domain of human CEACAM1 (residues 34-141) was synthesized with codon optimization for *E. coli* overexpression (GenScript). The construct

was inserted into a vector (pET-28b+) for a tagless expression of the IgV domain. The IgV domain was overexpressed from BL21 (DE3) Gold strain *E. coli* into inclusion bodies. Protein production was induced with 1 mM IPTG when cultures reached an OD600 of 0.8 and harvested after 4 h at 37˚C or overnight expression at 25˚C. The CEACAM-1 IgV domain was purified as previously described with slight alterations.[127] Cell pellets were homogenized and isolated inclusion bodies were washed as described above. The washed inclusion bodies were dissolved in a denaturing buffer containing 8 M urea at room temperature before centrifugation to remove debris. Refolding of human CEACAM IgV and IgV-cys were performed by drop-wise (~0.1 mL/min) addition of solubilized inclusion bodies into 10-25-fold their volume of a buffer containing 0.5 M L-arginine and 50 mM CHES pH 9.2 at 4°C while stirring, and incubated overnight. Refolded CEACAM1 IgV and IgV-cys were dialyzed against 4-8 L of 5 mM Tris pH 8.0 over 24 hours and the dialysis buffer was changed at least 3 times during dialysis. CEACAM1 IgV and IgV-cys dialysates were clarified by centrifugation and filtration then loaded over a MonoQ 10-100 GL ion exchange column that was pre-equilibrated in a buffer of 10 mM Tris pH 8.0. Bound protein was separated via NaCl gradient (0 mM to 200 mM NaCl). CEACAM1 IgV bind to a MonoQ ion-exchange column at 0 mM NaCl and elutes at 100-170 mM NaCl. Peak fractions were concentrated and loaded onto a HiPrep 26/300 Sephacryl S-75 column for size-exclusion chromatography in a buffer of 150 mM NaCl and 50 mM Tris pH 7.5. Biotinylation of purified CEACAM1 IgV domain was carried out using an EZ-Link Sulfo-HNS-Biotinylation kit (Thermo). Biotinylation reactions were performed with a 10-fold concentration of Sulfo-NHS-Biotin relative to protein. Successful biotinylation of lysine

residues was determined by HABA assay and resulted in ~2 biotin molecules per CEACAM1 molecule.

3.4.2 *NMR experiments.*

Nuclear magnetic resonance (NMR) screening experiments were performed at 25 °C using a 600 MHz Bruker Avance-III spectrometer equipped with a 5 mm single-axis x-gradient cryoprobe and a Bruker Sample Jet. Gradient enhanced, two-dimensional ^{1}H-^{15}N heteronuclear multiple-quantum coherence spectra (SOFAST-HMQC) spectra were recorded on TIM-3 (24 scans, ~12 min).[133] Spectra were processed and analyzed using Topspin (Bruker). Our in-house fragment library of ~13,800 compounds was screened as mixtures of 12 fragments in a 96-sample format using 16 μM of ^{15}N-labeled TIM-3, 800 μM of each fragment, and 4% DMSO-d6 for spectrometer locking purposes. Hit mixtures were identified by comparing the chemical shifts of backbone resonances to a ligand-free TIM-3 reference spectrum. Because fragments were screened as mixtures, deconvolution of hit mixtures was necessary to isolate individual hit fragments. Deconvolution was accomplished by screening each twelve-compound mixture hit as a series of twelve singleton samples.

SOFAST-HMQC titration experiments were used to quantify the binding affinity of the best hits identified from the screen. The change in ^{1}H-^{15}N chemical shifts of backbone resonances upon stepwise addition of fragment was measured and fit by an in-house script.[128]

^{15}N and ^{13}C double-labeled TIM-3 IgV domain protein was expressed from *E. coli* in M9 minimal media containing $^{15}NH_4Cl$ and ^{13}C-glucose as the sole nitrogen and carbon sources, as described above. Triple resonance experiments HNCA and HNCO using

$^{15}N/^{13}C$-TIM-3-IgV (0.8 mM) in 10 mM HEPES, 50 mM NaCl, pH 7.4 with 4% DMSO-d6, was performed at 25 ˚C on an 800 MHz Bruker Avance-III spectrometer equipped with a cryogenic probe. The data were processed using Topspin (Bruker) and analyzed by CcpNmr Analysis V2.

3.4.3 *Protein crystallization, data collection, and structure refinement.*

TIM-3 IgV domain was concentrated to 3-5 mg/mL and mixed with DMSO stock of desired ligand at a concentration of 4 mM-600 µM and 2-5% DMSO. A commercial screen of crystallization conditions (IndexHT, Hampton Research) was used to generate initial ligand-bound crystals. Ligand-free and ligand-bound crystals grew at 18 ˚C after 5-35 days in crystallization conditions containing 0.8 M potassium sodium tartrate tetrahydrate, 0.1 M Tris pH 8.5, and 0.5% w/v polyethylene glycol monomethyl ether 5,000. Ligand-bound crystals were found to grow more readily in crystallization conditions containing 0.8 M sodium tartrate dibasic dihydrate supplemented with 10 mM $CaCl_2$. Ligand-bound crystals for analog binding visualization were grown in crystallization conditions containing 0.8 M sodium tartrate dibasic dihydrate, 0.1 M HEPES pH 6.8-8.2, and 10 mM $CaCl_2$. Crystals were cryoprotected in mother liquor supplemented with 20% glycerol prior to freezing in liquid nitrogen. X-ray data were collected on the Life Sciences Collaborative Access Team (LS-CAT) Sector-21 beamlines at the Advanced Photon Source (APS), Argonne National Labs. Data were indexed, integrated, and scaled with HKL2000.[92] Molecular replacement with Phaser[93] was accomplished using Phenix[94] and the ligand-free TIM-3 structure previously determined (PDB code 6DHB) as the search model.[95] Structure refinement was accomplished with Phenix and included several rounds of

manual model building with COOT. Final refinement and X-ray data collection statistics are provided below in Table 3-4. Figures have been prepared using PyMOL.[96]

Table 3-4. X-ray data collection and refinement statistics for TIM-3 co-crystal structures with **2**, **3**, **22**, **35** and **38**.

Compound	**2**	**3**	**22**	**35**	**38**
PDB ID	NA	NA	7M3Y	7M3Z	7M41
Data Collection					
Space Group	C 2 2 2_1	P 2_1 2_1 2_1	C 2 2 2_1	C 2 2 2_1	C 1 2 1
Cell Dimensions					
a, b, c (Å)	47.149, 85.564, 53.515	30.890, 93.309, 96.321	46.958, 85.343, 53.697	46.928, 85.168, 53.476	85.215, 46.828, 53.905
α, β, γ (˚)	90, 90, 90	90, 90, 90	90, 90, 90	90, 90, 90	90, 93.05, 90
Resolution (Å)	26.76 – 1.80 (1.83 – 2.00)	29.40 – 2.00 (2.03 – 2.00)	26.85 – 1.69 (1.82 – 1.69)	26.74 – 1.40 (1.47 – 1.40)	26.91 – 1.79 (1.89 – 1.79)
Rmerge (%)	16.0 (62.9)	16.6 (97.7)	9.7 (76.3)	5.7 (41.6)	8.8 (28.9)
Mean I / σI	17.2 (3.43)	14.0 (2.12)	21.9 (2.18)	42.1 (2.55)	38.4 (10.8)
Completeness (%)	100 (100)	99.0 (97.7)	99.8 (99.5)	100 (100)	97.8 (95.0)
Redundancy	8.0 (8.0)	7.5 (7.3)	8.0 (7.9)	8.0 (7.2)	7.6 (7.8)
Structure Refinement					
No. Reflections	10350	19355	12384	21523	19564
R_{work} / R_{free}	0.1680 / 0.2079	0.2035 / 0.2465	0.1867 / 0.2131	0.1831 / 0.1954	0.1698 / 0.2127
R.m.s deviations					
Bond lengths (%)	0.007	0.008	0.006	0.006	0.007
Bond angles (˚)	0.930	0.996	0.918	1.024	1.052
Ramachandran					
Preferred regions (%)	93.46	94.34	94.39	96.26	93.93
Allowed regions (%)	6.54	5.66	6.61	3.74	5.61
Disallowed regions (%)	0	0	0	0	0.47

Related to Figures 3-8, 3-9, 3-10, 3-13, and 3-14. Highest resolution shell are in parenthesis.

3.4.4 *FPA saturation binding assays for **23** and **SP2**.*

FITC-labeled small-molecule probes **23** and **SP2** were synthesized as described above and titrated with TIM-3 IgV protein. FPA measurements were carried out in 384-well, black, flat-bottom plates (Greiner Bio-One) using the BioTek Cytation 3 plate reader. All assays were conducted in assay buffer containing 20 mM HEPES pH 7.4, 150 mM NaCl, 0.05% pluronic acid, and 5% final DMSO concentration. To measure the association of the probe to TIM-3, 1 µM of **23** or **SP2** was incubated with varying concentration of the TIM-3 protein prepared by a 12-point, 50% serial dilution with the top concentration equaling 350 µM and a final volume of 50 µL. The anisotropy data collected were plotted and fit to binding saturation kinetics in the Prism graphical software to determine the K_d.

3.4.5 *FPA competition assays.*

FITC-labeled probes **23** and **SP2** were used for analog competition assay. FPA measurements were conducted buffer and working conditions as described above. To measure the displacement of the **23** from TIM-3, a working condition of 2 µM **23** with 15 µM TIM-3 in assay buffer was used before the addition of compound. To measure the displacement of **SP2** from TIM-3, a working condition of 100 nM of **SP2** with 3.25 µM TIM-3 in assay buffer was used before addition of compound. For IC_{50} determination, compounds were diluted in DMSO in a 11-point, 75% serial dilution scheme, added to assay plates, and incubated for 1.5 h at room temperature. The highest final compound concentrations were 100 µM and 30 µM for competition against **23** and **SP2**, respectively. The change in anisotropy was measured and used to calculate an IC_{50} (inhibitor concentration at which 50% of bound probe is displaced) by fitting the anisotropy data

using Prism to a four-parameter dose–response (variable slope) equation. This was converted into a binding dissociation constant (K_i) according to the formula:[134]

$$K_i = [IC]_{50}/([L]_{50}/K_d + [P]_0/K_d + 1)$$

where $[IC]_{50}$ is the concentration of the free inhibitor at 50% inhibition, $[L]_{50}$ is the concentration of the free labeled ligand at 50% inhibition, $[P]_0$ is the concentration of the free protein at 0% inhibition, and K_d represents the dissociation constant of the FITC-labeled peptide probe. Compounds were evaluated using technical replicate measurements in triplicate and K_i values shown are the average of those triplicates.

3.4.6 *Cellular assays.*

For all cellular experiments, CD3+ T cells were isolated from the PBMC of a healthy donor using MojoSort(TM) Human CD3 T Cell Isolation Kit from BioLegend (480022). These T cells were activated with CD3/CD28 magnetic beads (Gibco) for 6 days in RPMI media. Cells were stained with monoclonal antibodies against PD-1 (BioLegend) and Tim-3 (BioLegend). TIM-3 expression was measured by flow cytometry using a BD FACSCelesta and expression ranged from 40-80% of TIM-3+ T cells across experiments. For galectin-9 experiments, activated T cells were cultured with 2.5 µg/mL of galectin-9 and 1 µg/mL of IL-7 for 24 h along with the testing conditions of 5 µg/mL anti-TIM3 (ab185703, Abcam) or 0.1-10 µM of **35** or **38**. Cells were stained with Zombie Aqua™ Fixable Viability Kit and viability was measured by flow cytometry using a BD FACSCelesta. For CEACAM1 binding experiments, activated T cells were incubated with 1-100 µM **35** or **38** for 30 min before the addition of CEACAM1 or biotinylated CEACAM1 at 80 µg/mL for 4 h. FITC conjugated streptavidin (Thermo) was used to stain the cells before measuring geometric mean fluorescence intensity (gMFI)

by flow cytometry. I would like to thank Gabriel Rodriguez and Dr. Michael Korrer from Dr. Young Kim's lab for their work on these experiments.

Chapter 4 - Fragment screen of T cell immunoglobulin mucin receptor 3 (TIM-3) with calcium bound in FG-CC' binding cleft.

4.1 Introduction

4.1.1 *The FG-CC' binding cleft is a potential therapeutic "hot spot."*

We have previously discussed in Chapter 3 that TIM-3 has four known ligands that interact with the IgV domain: phosphatidylserine (PtdSer), carcinoembryonic antigen-related cell adhesion molecule 1 (CEACAM1), high mobility group box 1 (HMGB1), and galectin-9.[113–116] Galectin-9 has been shown to bind TIM-3 through two carbohydrate recognition domains of galectin-9 and N-linked oligosaccharides of the IgV domain while the remaining ligands have all been shown to bind to the FG-CC' cleft in a Ca^{2+} dependent manner.[113,114,116]. The FG-CC' cleft represents a potential therapeutic "hot spot" to target for small molecule inhibition. Indeed, a recent study suggested that therapeutic antibodies capable of exhibiting optimal anti-tumor responses target TIM-3 at the FG-CC' cleft confirming that this is the most likely site to target to achieve inhibition of TIM-3 activity.[132]

A recent structure of TIM-3 IgV domain revealed the conserved metal ion-dependent ligand binding site that coordinates a single calcium cation (Ca^{2+}) within the FG-CC' binding cleft (PDB ID: 6DHB, Figure 4-1).[95] Octahedral coordination contacts are made with Ca^{2+} and the backbone carbonyls of I114 and G116 and side chains of N119 and D120 leaving two additional coordination sites for bulk solvent or ligand binding. Furthermore, this structure revealed that a single benzoic acid molecule from the cryoprotectant used was coordinating with Ca^{2+} in the FG-CC' cleft while also appearing to be stabilized by a face to edge pi-pi interaction with F61 and neighboring hydrophobic side chains of V60, I117, and M118 suggesting this site is accessible by small molecule

ligands. The accessibility of the FG-CC' cleft to protein and small molecule binding alike highlights the flexibility of the cleft to accommodate various ligands.

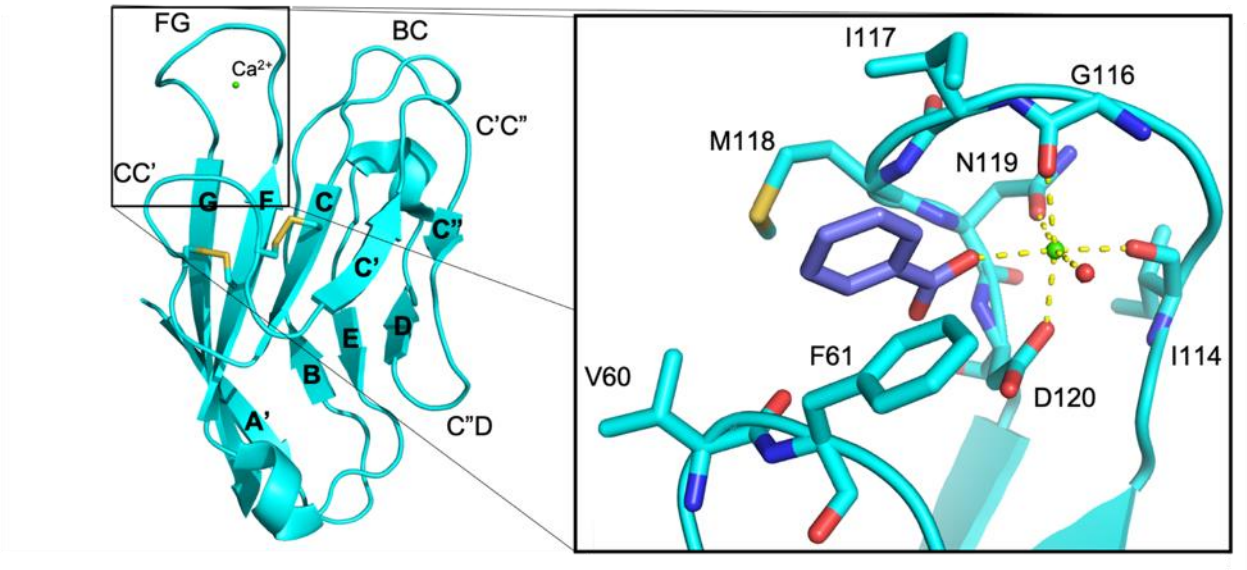

Figure 4-1. The TIM-3 FG-CC' binding cleft.
The TIM-3 IgV domain (PDB 6DHB) is shown to left with β-strands and loops labeled. The highlighted inset is a close-up view of the FG-CC' cleft. FG and CC' loop residues are shown as sticks and labeled accordingly. Coordination contacts with Ca^{2+} (green sphere) are displayed as yellow dashed lines. The cryo-protectant benzoic acid coordinated with Ca^{2+} is shown as purple sticks and crystallographic water is depicted as a red sphere.

A second Ca^{2+} free structure of the IgV domain has also been elucidated (PDB ID: 5F71).[125] This structure is considered to be less biologically relevant compared to the Ca^{2+}-bound structure and also introduced a second potential metal binding site where the C"-D loop adopts a helix turn to allow coordination of a single sodium ion (Na^{+}, Figure 4-2C). Regardless of biological relevance, a SiteMap (Maestro, Schrodinger) analysis of both 6DHB and 5F71 structures identify the FG-CC' cleft as a potentially druggable site (Figure 4-2B,D). SiteMap analysis provided these potential binding sites with SiteScores of 0.62 and 0.73, respectively, both of which are below the 0.8 threshold which distinguishes a site to be classically "druggable." Regardless of the low SiteScores, the

FG-CC’ cleft appears to be the most druggable region of TIM-3 and should be targeted for inhibitor development.

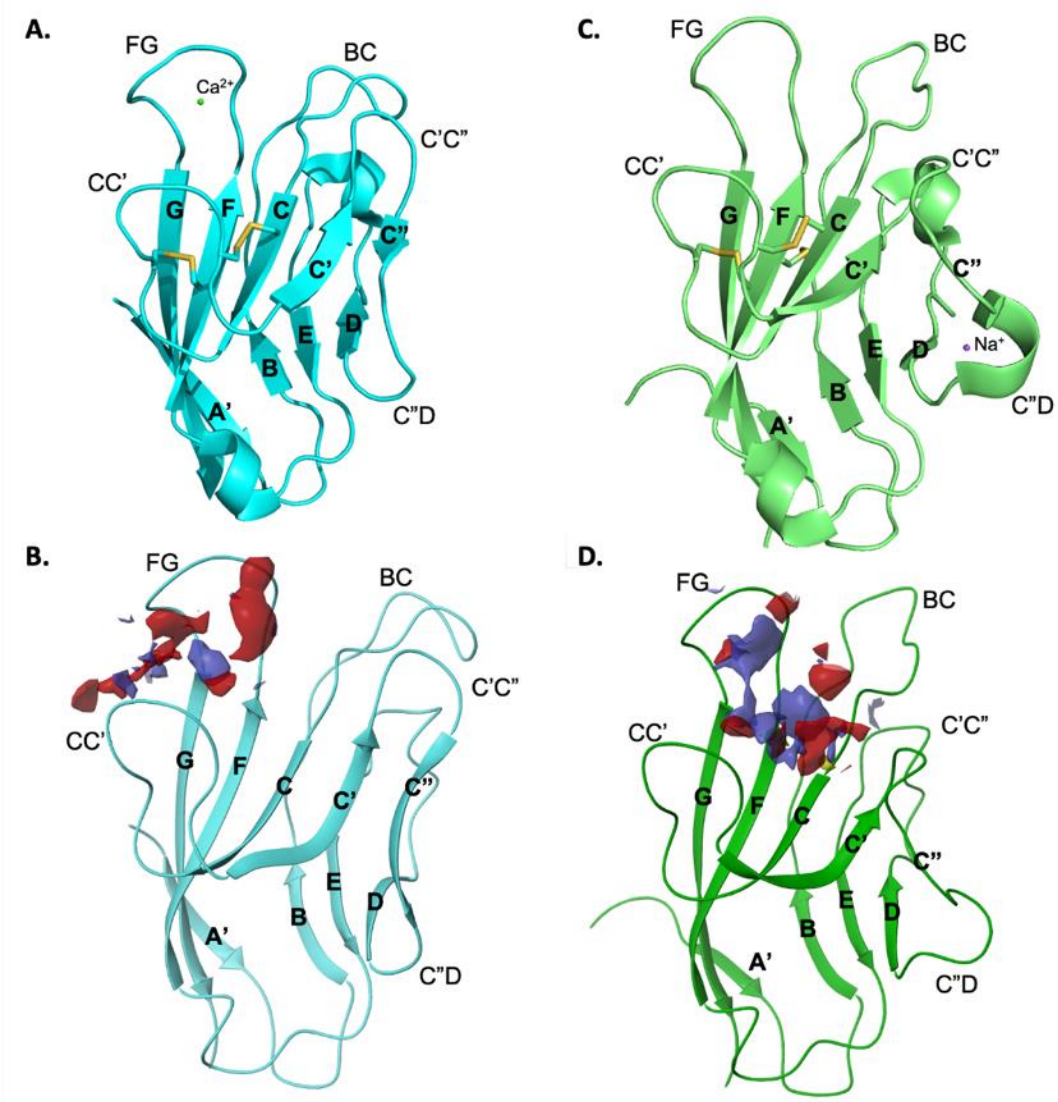

Figure 4-2. SiteMap analysis of TIM-3 IgV domain structures.
(A,C) The Ca^{2+}-bound and unbound TIM-3 IgV domains structures (A-PDB ID: 6DHB (cyan); C-PDB ID: 5F71 (green)) with β-strands and loops labeled. Bound metals are shown as colored spheres (Ca^{2+}, green; Na^{+}, purple). (B,D) Druggable sites as proposed by SiteMap analysis are shown as H-bond acceptor (red), H-bond donor (blue), and hydrophobic (yellow) surfaces.

There have been no ligand-bound structures of hTIM-3 IgV domain deposited into the protein databank to further aid the mapping of the critical interactions in the FG-CC’ cleft therapeutic hot spot. However, all previous interaction studies have identified through mutational analysis that Ca^{2+} coordination is necessary for ligand interaction at the FG-

CC' cleft. Furthermore, the benzoic acid bound structure (PDB ID:6DHB) revealed carboxylate coordination with Ca^{2+} and the FG-CC' accommodates PtdSer binding in a Ca^{2+}-dependent manner providing evidence that this site is indeed amenable to small molecule binding. Importantly, recent studies have suggested that therapeutic antibodies capable of exhibiting optimal anti-tumor responses target TIM-3 at the FG-CC' cleft where most known ligands bind.[132] Taken together, these findings suggest that small molecules found to bind the FG-CC' cleft will have ligand inhibiting capabilities ultimately leading to functional inhibition of TIM-3.

4.2 Results

4.2.1 *Fragment screen of TIM-3 FG-CC' binding cleft.*

We sought to conduct a protein-observed fragment screen that would specifically target the FG-CC' binding cleft. Uniformly ^{15}N-labeled TIM-3 IgV domain purified as previously described (Chapter 3) provides a suitable ^{1}H-^{15}N SOFAST HMQC spectra for protein-observed fragment screening (0.2 mg/mL TIM-3 IgV, 24 scans, ~12min). Our lab and others have assigned the amino acid backbone resonances of the TIM-3 IgV domain through triple resonance NMR experiments.[95] Supplementation of $CaCl_2$ to the NMR buffer resulted in chemical shift perturbations in signals assigned to residues in the FG loop that coordinate with the Ca^{2+} cation, consistent with the crystal structure of Ca^{2+}-bound TIM-3 IgV domain (Figure 4-3A). Furthermore, upon addition of 6:0 PtdSer (Avanti Polar Lipids), a short acyl chain derivative of PtdSer, in the presence of Ca^{2+} results in additional peak shifts or broadening observed at resonances assigned to the FG and CC' loop regions (Figure 4-3B). Mapping these residue shifts to the IgV domain suggests that PtdSer binding results in a conformational change of the CC' loop to accommodate the

ligand (Figure 4-3C). Chemical shifts are not observed upon addition of 6:0 PtdSer alone confirming that PtdSer binding is Ca^{2+}-dependent. These experiments lay the groundwork to explore other small-molecule compounds that bind to the FG-CC' cleft in a Ca^{2+}-dependent manner via protein-observed NMR screening.

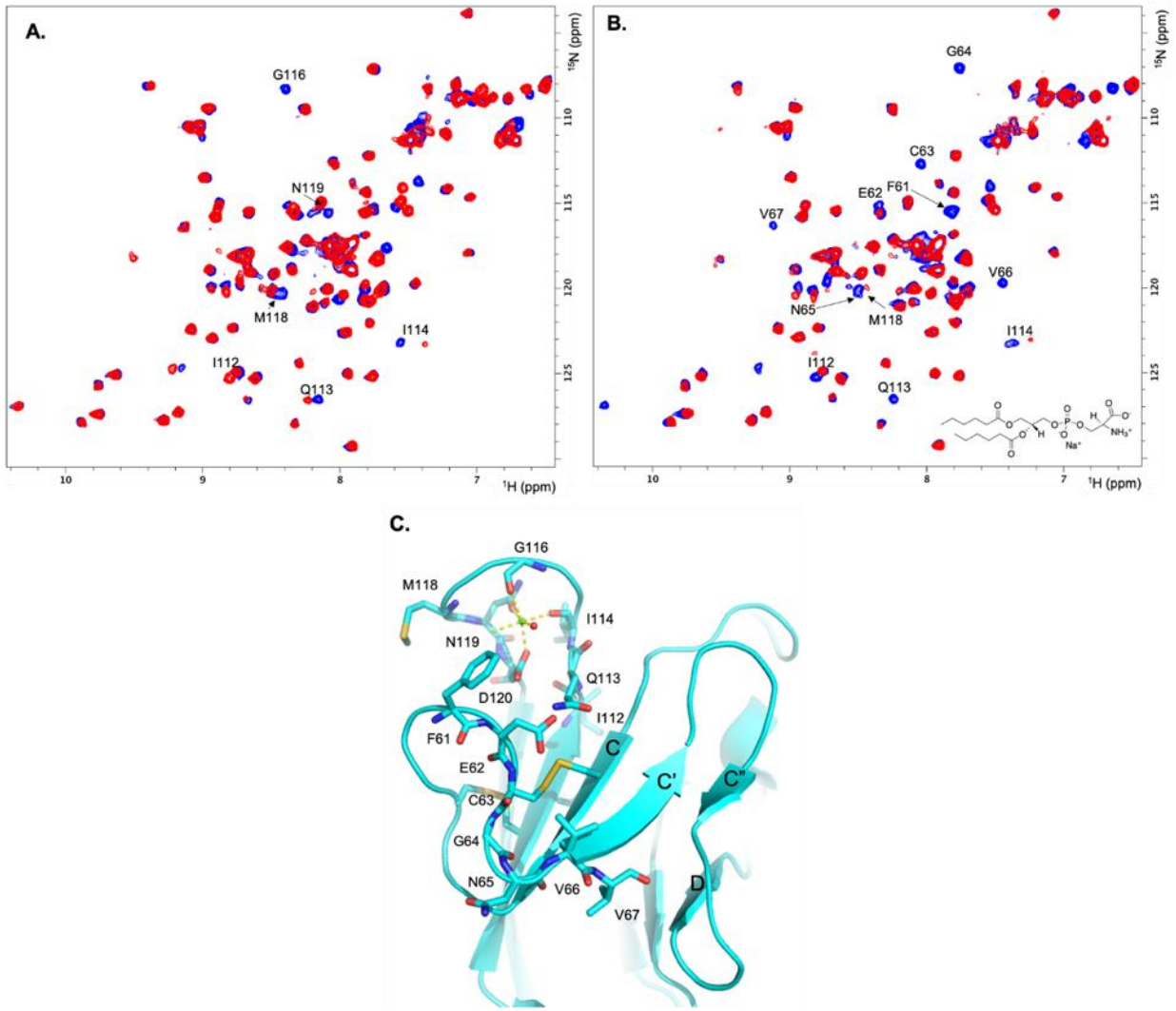

Figure 4-3. Recapitulation of FG-CC' binding events through 2D NMR experiments.
(A) Overlayed ^{1}H-^{15}N SOFAST HMQC spectra of TIM-3 IgV domain alone (blue) and with 10 mM $CaCl_2$. Chemical shift perturbations of FG-CC' cleft residues are labeled. (B) Overlayed ^{1}H-^{15}N SOFAST HMQC spectra of TIM-3 IgV domain with 10 mM $CaCl_2$ alone (blue) and with 830 µM 6:0 PtdSer (red). Chemical shift perturbations of FG-CC' cleft and CC' loop residue signals are labeled and the structure of 6:0 PtdSer is displayed in the inset. (C) Residues that exhibited chemical shift perturbations are mapped and labeled onto the structure of TIM-3 IgV domain.

Screening of an unbiased fragment library of 13,824 molecules has been completed by collecting protein-observed ^{1}H-^{15}N SOFAST-HMQC NMR spectra of uniformly ^{15}N-labeled TIM-3 IgV domain (22-130) in mixtures containing 12 fragments. Mixture samples were considered a hit if, relative to the absence of fragments, chemical shift changes were observed for the backbone resonances associated with the FG-CC' cleft in the presence of fragments (Figure 4-4). Hit mixtures were then deconvoluted as singletons to identify the fragment that binds the FG-CC' cleft. A total of 61 fragments were found to produce chemical shift changes in FG-CC' residues, resulting in a final hit rate of 0.5%. Previous statistical analyses suggest that a protein target with a greater than 0.1% fragment hit rate is considered to be druggable by small molecule.[72] Our results suggest that the discovery of a potent small molecule TIM-3 inhibitor is feasible using fragment-based methods.

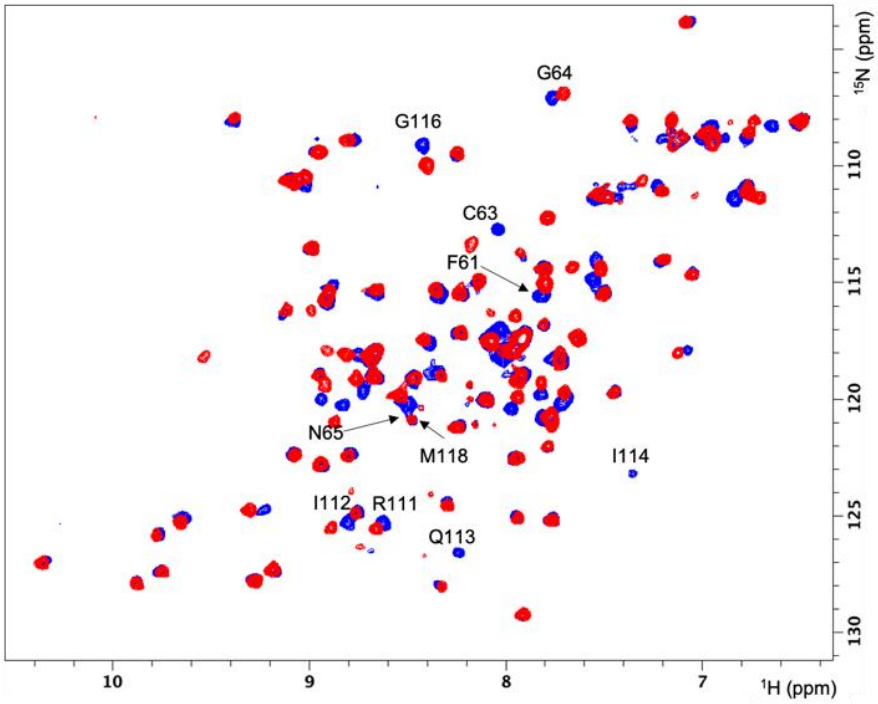

Figure 4-4. Representative fragment hit identified by NMR-based screen.
Representative example of SOFAST HMQC spectra of TIM-3 alone (blue) and with 800 µM fragment hit (red) as identified through fragment screening. Chemical shift perturbations of residues belonging to the FG-CC' cleft are labeled.

4.2.2 *Hit clusters from fragment screen.*

The 61 hits identified have been clustered into 3 chemical clusters (Figure 4-5). Binding affinities were determined by SOFAST HMQC titration experiments and ranged from 100 μM to >2 mM for all hits, with 10 fragments having a K_d less than 1 mM. Cluster 1 fragment hits (**1**-**6**) represent carboxylic acid containing 5,5- and 5,6-fused ring chemotypes including, but not limited to, several substituted indoles. Cluster 1 was the most represented chemotype within the identified hits, consisting of over half of all hits. Chemical shift perturbations seen with cluster 1 fragment **1** closely resemble the shift pattern seen upon PtdSer binding with the notable additional shift of R111 whose side chain forms the bottom of the FG-CC' binding cleft (Figure 4-4). Cluster 2 hits (**7**-**9**) represent 6,6-fused ring chemotypes, including several quinolines and quinolones. The least represented cluster 3 consists of 3 fragment hits (**10**-**12**) with carboxylic acid containing tricyclic carbazole-like 6,5,6-fused ring systems. Together, the majority of hits are homologous and share the general chemical architecture of a variously substituted planar heterocyclic core with at least one carboxyl substitution. The similarities among the clusters suggest Ca^{2+} coordinates with the carboxyl group and the planar core makes additional interactions with the FG and CC' loop residues similar to benzoic acid in PDB 6DHB (Figure 4-1).

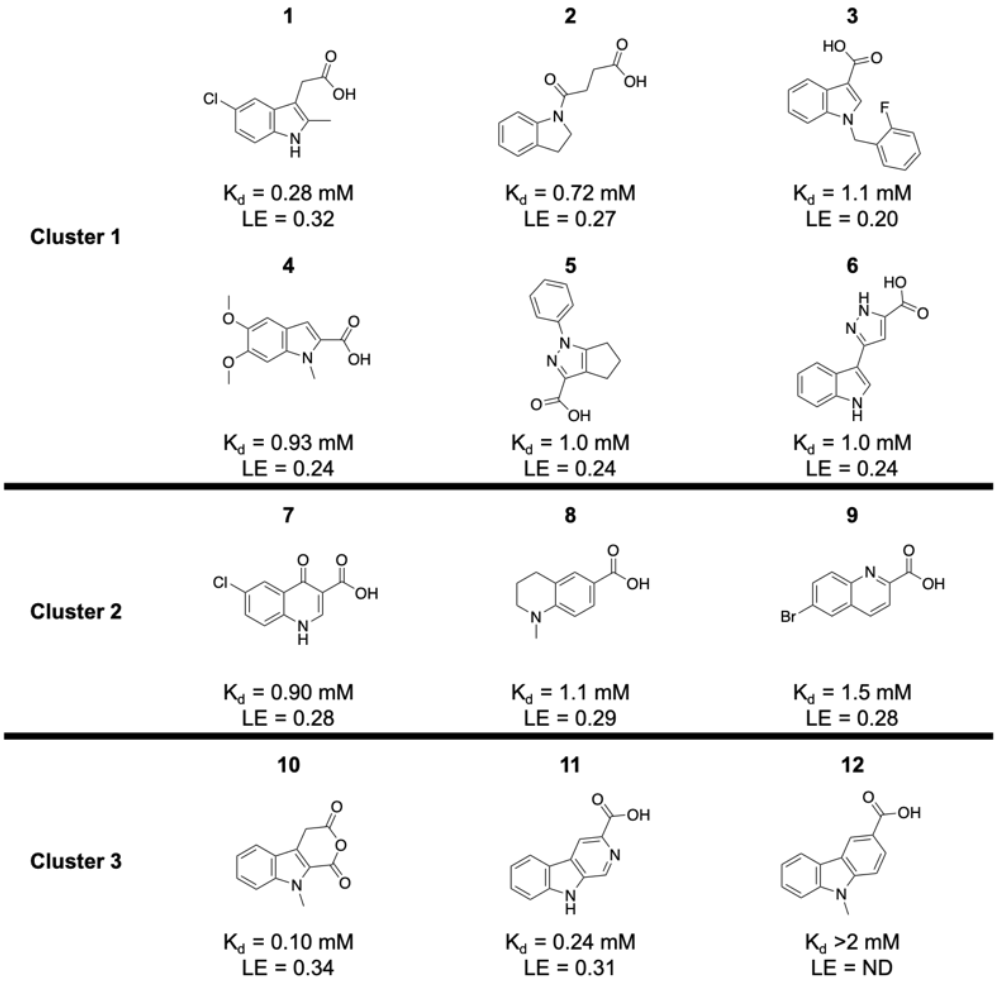

Figure 4-5. TIM-3 FG-CC' fragment hits clustered by chemotype.
Chemical structures of different fragment hits identified through NMR screening are labeled and clustered by chemotype. K_d values were determined by SOFAST HMQC titration experiments.

4.2.3 *Co-crystal structures of fragment hits bound to TIM-3.*

It was important to understand how these molecules bind to the FG-CC' cleft. To obtain this information, we sought to co-crystallize representative hits from each cluster and determine the X-ray structures of TIM-3 when complexed. We determined the X-ray structure of TIM-3 complexed with the cluster 1 hit 2-(2,5-dimethyl-1*H*-indol-3-yl)acetic acid (**13**) (Figure 4-6A). Fragment **13** is a matched-pair 5-methyl analog with the cluster 1 fragment **1** with comparable affinity, K_d = 360 µM and 280 µM respectively. The interaction of **13** with the FG-CC' binding cleft is anchored by coordination of the acetic

acid with Ca^{2+} in a monodentate fashion. Monodentate carboxylate coordination is preferred over the bidentate mode when the metal-free carboxylate oxygen atom is involved in hydrogen bonding.[135] The carboxylate of **13** likely forms a salt bridge with the R111 guanidino group at the bottom the FG-CC' cleft, an interaction that is likely unique to our fragments compared to PtdSer binding based on the additional R111 resonance shift seen in NMR spectra. Furthermore, additional hydrogen bonding interactions are made between the carboxylate of **13** and the backbone amide of N119 and D120. The CC' loop residues V60 and F61 and the FG loop residues I117 and M118 are extended towards solvent but create a hydrophobic clamp which the indole core is sandwiched between. Methyl substitution off either end of the indole core span across the hydrophobic clamp maximizing the hydrophobic interaction. The indole core is further stabilized by a face-to-edge pi-pi interaction with F61 (Figure 4-6B).

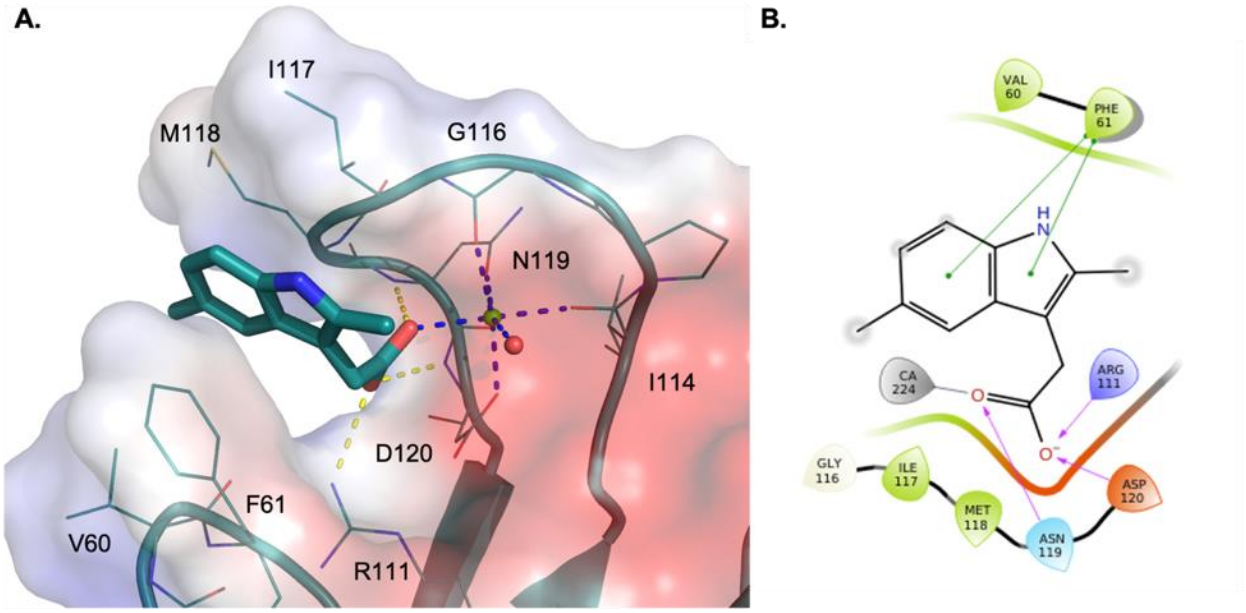

Figure 4-6. X-ray structure of TIM-3 bound to fragment 13.
(A) View of the FG-CC' binding cleft with fragment **1** bound. Residues in contact with **13** (sticks) or coordinated Ca^{2+} (green sphere) are shown as lines. Dashed blue lines depict coordination contacts and dashed yellow lines depict polar contacts. TIM-3 is shown with a transparent electrostatic potential surface with electronegative (red) and electropositive (blue) surfaces displayed. (B) 2D interaction diagram of **13** with TIM-3. Pink arrows depict hydrogen bonds, grey lines depict metal coordination, and green lines depict pi-pi stacking.

It should be noted that the co-crystal structure of TIM-3 and **13** revealed that symmetry mates made crystal contacts with ligands bound in the FG-CC' cleft. Namely, the side chain of D92 of a neighboring symmetry mate forms a hydrogen bond with the indole core nitrogen (Figure 4-7A). This was concerning because this crystal packing contact could be artificially affecting the observed binding pose of **13**. Therefore, we sought further structural information to confirm this binding pose.

We determined the X-ray structure of TIM-3 complexed with a the matched-pair analog of **13** 2-(5-fluoro-2-methyl-1*H*-indol-3-yl)acetic acid (**14**). The new co-crystal structure with **14** provided a different crystal packing and space group compared to **13**, $P2_1\ 2_1\ 2_1$ and $P2_1\ 2_1\ 2$ respectively, and resulted in a single ligand-bound protein monomer in the asymmetric unit uninfluenced by neighboring symmetry mates. The alignment and overlay of the two structures revealed near identical binding poses in which **14** makes the same Ca^{2+} coordination, hydrogen bonding, and hydrophobic interactions as **13** (Figure 4-7B). The conformations of the FG-CC' cleft residues F61 and I117 were not identical, however, highlighting the flexibility of the hydrophobic clamp which is composed solely of solvent exposed hydrophobic side chains. These two structures provided confidence in the illustrated binding pose and critical intermolecular interactions in the FG-CC' binding cleft of 2- and 5- substituted 2-(1*H*-indol-3-yl)acetic acid analogs.

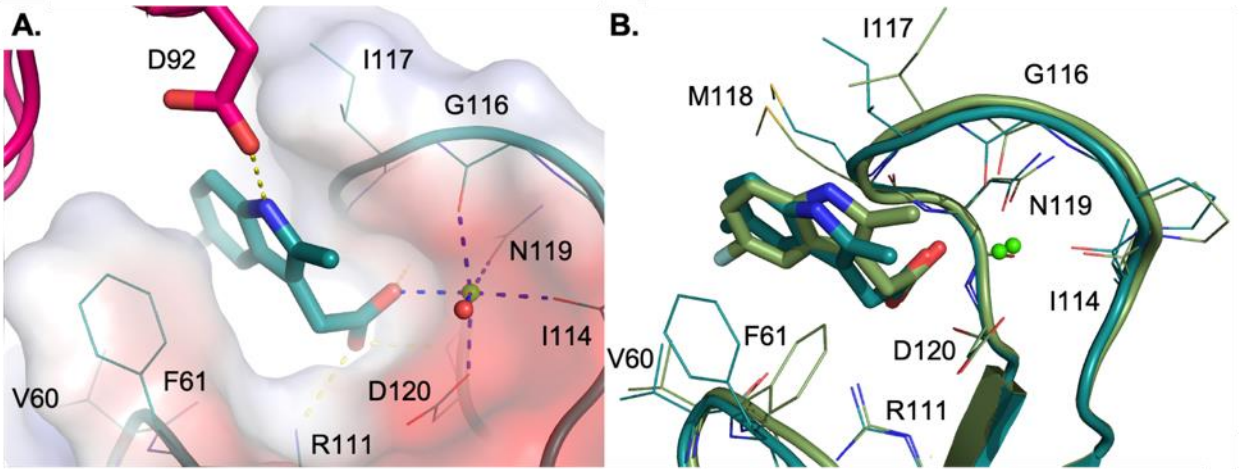

Figure 4-7. Confirmation of indole acetic acid analogs binding pose.
(A) Co-crystal structure of TIM-3 and **13** showing the intermolecular stabilization of binding by D92 of a crystal packing symmetry mate (pink). (B) Aligned FG-CC' binding sites of the co-crystal structure of TIM-3 with **13** (dark green) and a matched-pair 5-fluoro analog, **14** (olive green).

A third cluster 1 fragment hit co-crystal structure was obtained with 4-(indolin-1-yl)-4-oxobutanoic acid (**2**). Similar to **13** and **14**, the carboxyl group of **2** coordinated with Ca^{2+} in a monodentate fashion (Figure 4-8A). Additional carboxylate hydrogen bonding exists between the metal-free carboxyl oxygen and the backbone amide of N119 and D120. The metal-free carboxyl oxygen appears to be outside of optimal hydrogen bonding distance with R111 guanidino group (3.7 Å), but close enough to suggest and electrostatic interaction between the negatively charged carboxyl and positively charged guanidino. The carbonyl of **2** also makes a hydrogen bond with the backbone amide of M118. The indoline core make is sandwiched between the hydrophobic clamp of CC' loop residues V60 and F61 and the FG loop residues I117 and M118 (Figure 4-8A,B).

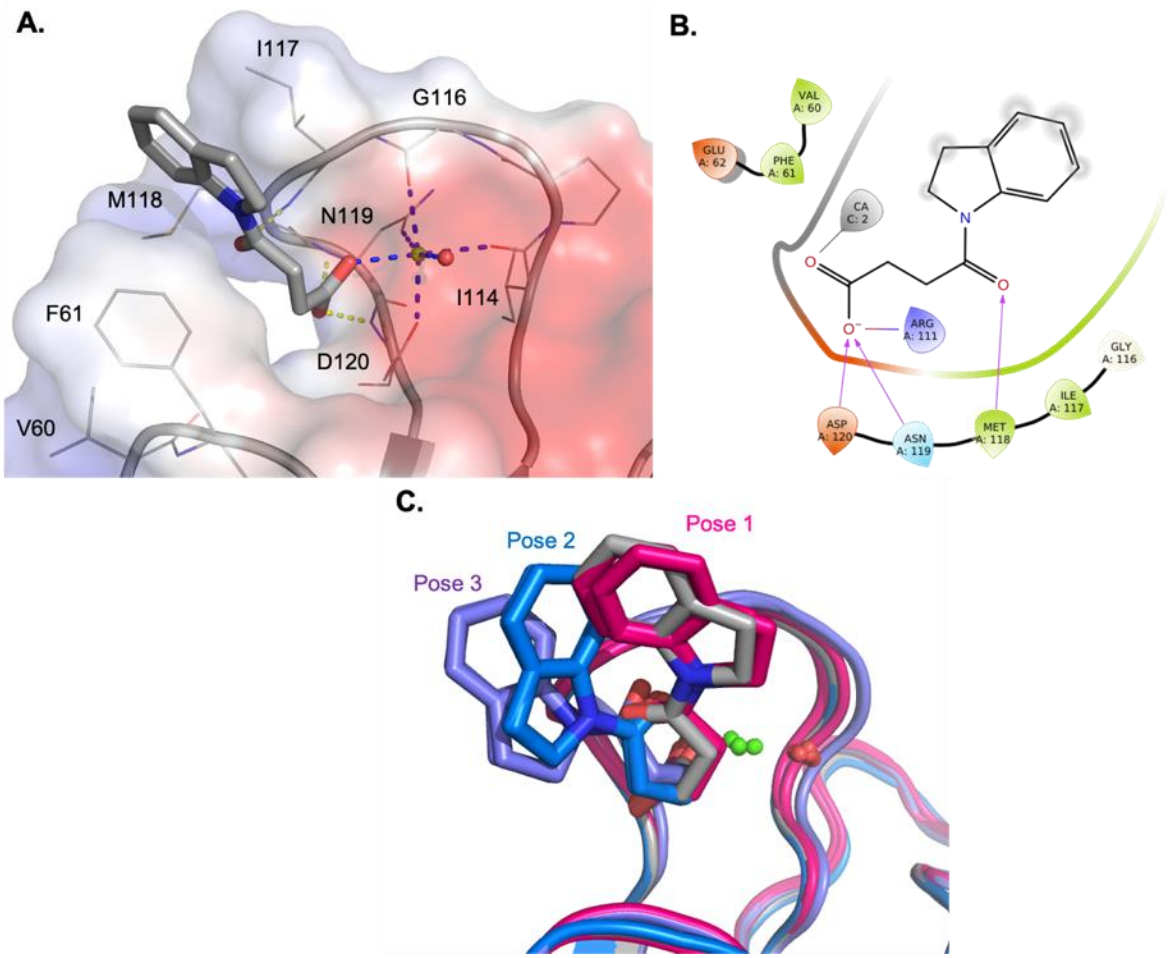

Figure 4-8. X-ray structure of TIM-3 bound to fragment 2.
(A) A view of the FG-CC' binding site with fragment **2** bound. (B) 2D interaction diagram of **2** with TIM-3. Pink arrows depict hydrogen bonds, grey lines depict metal coordination, and blue-red lines depict electrostatic interaction. (C) Overlay of fragment **2** binding poses solved in space group C121 (grey) and P1 (pink, blue, purple).

The indexed reflections collected from the TIM-3 co-crystal with **2** suggested a C121 space group that allowed for two protein monomers in the asymmetric unit. During refinement, the electron density for one ligand bound to the first monomer was clearly defined, however the electron density for the second ligand bound to the second monomer was more ambiguous. Although electron density existed for the second ligand in the second monomer FG-CC' cleft, a single binding pose could not be defined suggesting that multiple binding poses may exist. For this reason, the reflections were re-indexed in the lowest symmetry primitive monoclinic (P1) space group which expanded

the asymmetric unit to include eight protein monomers. When the data were refined in this space group, three distinct binding poses were revealed (Figure 4-8C). The predominant binding pose, pose 1, was found in four monomers and is consistent with the pose seen when the data were indexed in the higher C121 space group. The lesser represented poses 2 and 3 were each found in two monomers each and shared the oxobutanoic acid intermolecular interactions seen in pose 1 although in a slightly different conformation. Poses 2 and 3 predominantly differ in the position of the indoline core that is hydrophobically attracted to two different side chain conformations of I117 and M118. Collectively, the three poses suggest a binding interaction anchored by carboxyl coordination with Ca^{2+} and hydrogen bonding with the FG loop backbone with weak hydrophobic interactions between indoline and the hydrophobic clamp side chains that are not strong enough to adopt a single conformation.

Exhaustive attempts to co-crystalize TIM-3 with hits from cluster 2 and 3 in the presence of Ca^{2+} were unsuccessful. Commercial and focused crystallization condition screening of two protein constructs (residues 22-130 and 24-130) that had previously been successfully crystalized consistently produced unbound protein structures. This may be attributable to the weak binding affinities, particularly for cluster 2 hits which would be expected to reach saturation levels only above 10 mM. In most cases, the FG-CC' site was found to be free of coordinated Ca^{2+} similar to a previously reported TIM-3 structure (PDB 5F71). Although Ca^{2+}-bound TIM-3 is considered to be the most biologically relevant conformation of the protein, the binding constant of Ca^{2+} has been reported to be very weak, 27.2 mM when assayed by NMR titration.[95] Coordination of Ca^{2+} is likely further stabilized by fragment binding, however, weakly coordinating Ca^{2+} in

addition to weak fragment binding likely leads to a low proportion of the coordinated and ligand-bound protein in solution ultimately making fragment-bound crystallization difficult. Cluster 3 hits had better or equivalent binding affinities to fragments in cluster 1 that proved to be crystallizable. In this circumstance, it is probable that the fragment-bound protein with cluster 3 hits adopts a conformation that disrupts crystal packing and is not favorable for crystallization.

4.2.4 *Molecular modeling of cluster 3 fragment hits.*

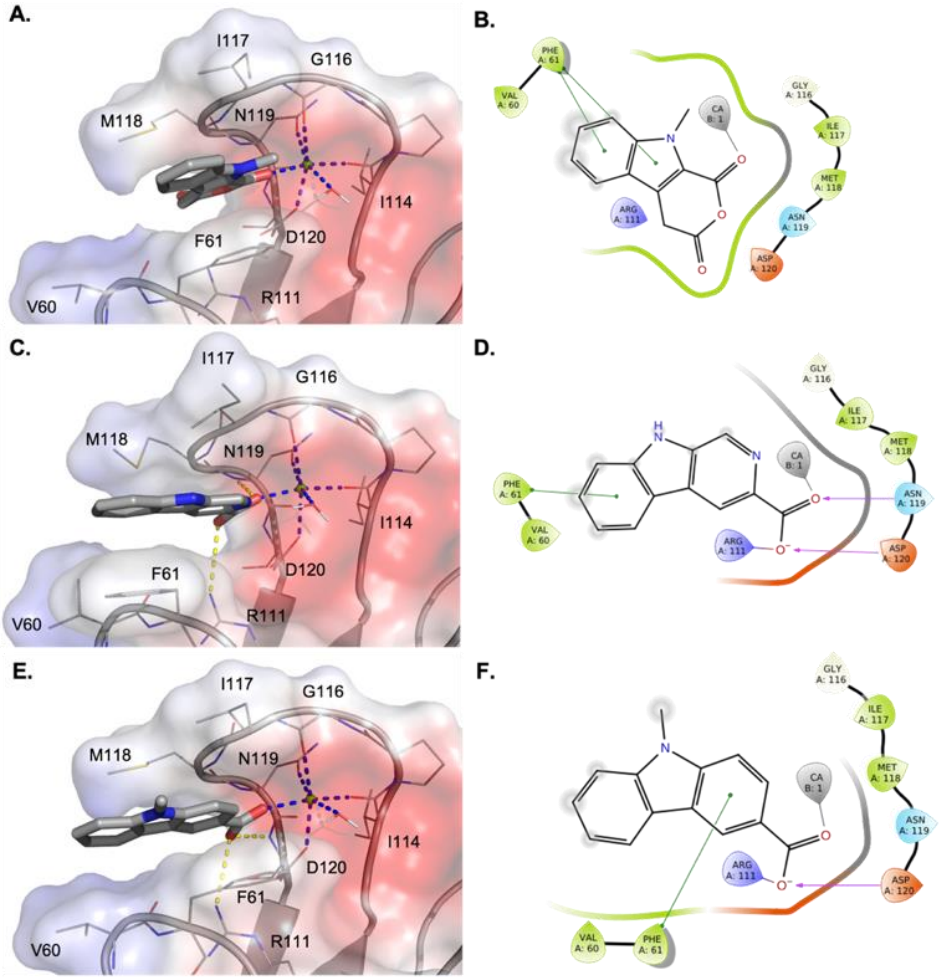

Figure 4-9. Molecular modeling of cluster 3 fragment hits.
Top scored FG-CC' cleft binding poses of **10** (A), **11** (C), and **12** (E) suggested by InducedFit docking. 2D interaction diagrams of **10** (B), **11** (D), and **12** (F) with TIM-3. Pink arrows depict hydrogen bonds, grey lines depict metal coordination, blue-red lines depict salt bridge formation, and green lines depict pi-pi stacking.

To generate a model of how cluster 3 fragments may bind to the TIM-3 FG-CC' cleft molecular docking experiments were utilized; cluster 2 hits were not analyzed in this manner due to weak starting binding affinities. Maestro InducedFit (IDF) docking experiments were run to account for the high degree of flexibility seen in the hydrophobic side chains of FG loop residues I117 and M118 and CC' loop residue F61 as exemplified in crystal structures from cluster 1 hits. Docking was constrained to include metal coordination of Ca^{2+} as to avoid ambiguous ligand fitting in the FG-CC' cleft. The best docking score binding pose for each cluster 3 compound, 9-methyl-4,9-dihydropyrano[3,4-*b*]indole-1,3-dione (**10**), 9*H*-pyrido[3,4-*b*]indole-3-carboxylic acid (**11**), and 9-methyl-9*H*-carbazole-3-carboxylic acid (**12**), are shown in Figure 3-12.

The binding pose suggested by IDF docking for compound **10** shows only two primary intermolecular interactions within in the FG-CC' cleft: pyrandione coordination with Ca^{2+} and pi-pi stacking between the compound indole core and F61 (Figure 4-9A,B). It is noteworthy that this docking pose of **10** is the scored the lowest of the 3 shown in Figure 4-9 which is inconsistent with the measured binding affinities by NMR (Figure 4-5). This inconsistency may suggest the binding pose is not a reliable representation of compound **10** binding. We have previously seen that cluster 1 fragment binding events are stabilized by additional hydrogen bonding with the FG loop backbone. Given the strong binding affinity measured by NMR, it is likely that the pyrandione of **10**, which contains several available oxygen lone pairs for hydrogen bonding, participates in similar interactions with the FG loop backbone although they are not illustrated in the binding pose suggested by IDF docking.

The binding poses suggested by IDF docking for compounds **11** and **12** are very similar, which one might expect considering the chemical similarity between the compounds (Figure 4-9C,E). The Ca^{2+}-coordinating carboxyl of both compounds closely mimic the interactions seen in the co-crystal structures of **13** and **14**: coordination with Ca^{2+}, additional hydrogen bonding with the backbone nitrogen of N119 (**11**) and D120 (**11** and **12**), and salt bridge formation with R111 (Figure 4-9E,F). F61 participates in parallel displaced pi-pi stacking with the carbazole cores of each compound, however in different side chain conformations. With **11**, F61 appears to favor and side chain "out" conformation which places the side chain out of the FG-CC' cleft towards solvent. The fused pyridine nitrogen of **11** may participate in a hydrogen bond with the crystallographic water that is coordinated with Ca^{2+}; this potential interaction is not illustrated in Figure 4-9.

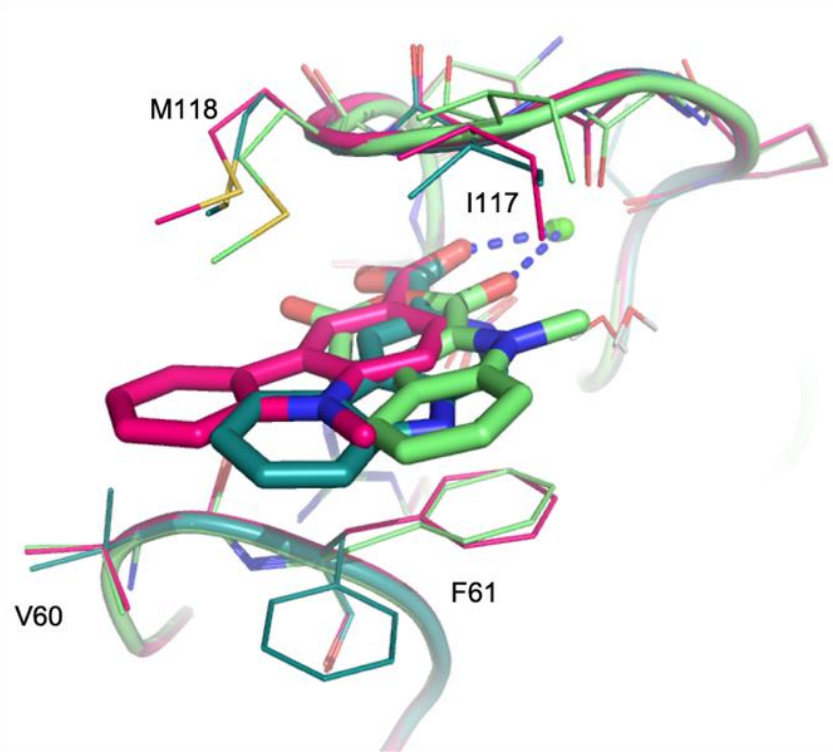

Figure 4-10. Overlay of fragment 10, 11, and 12 molecular modeling binding poses.
Binding poses of **10** (lime green), **11** (dark green), and **12** (pink) are aligned and overlayed. Coordination contacts with Ca^{2+} are depicted as blue dashed lines.

Collectively, the binding poses of cluster 3 hits suggested by IDF docking indicate an anchoring Ca^{2+} coordinating interaction stabilized by additional hydrogen bonding between the carboxylic acid and the FG loop backbone while the carbazole core is sandwiched between the hydrophobic FG-CC' side chains and pi-pi stacks with F61. Overlay of the distinct poses illustrates that the planar carbazole core is capable of sliding between the hydrophobic clamp depending on the conformation of the solvent exposed FG-CC' loop side chains (Figure 4-10). It is possible that the position of the carbazole core varies upon binding and potentially pivots around the anchoring carboxyl interactions. This variable binding along with an F61 "out" conformation might contribute to the disruption of crystal packing leading to difficulties in crystallization.

4.3 Conclusions

Eleven anti-TIM3 reagents are currently undergoing clinical trials in either monotherapy or in combination with antibodies that target other immune checkpoint receptors. It has previously been suggested that the most efficacious TIM-3 antibodies engage portions of the FG-CC' cleft and disrupt interactions with natural ligands at that site. It would therefore follow that small molecule compounds that engage the FG-CC' site would inhibit TIM-3 activity similarly to the most effective antibodies. We conducted an NMR-based fragment screen to probe the biologically relevant Ca^{2+}-bound form of TIM-3 and isolated 61 fragment hits that bind to the Ca^{2+}-bound FG-CC' cleft. The binding affinities of the isolated hits ranged from 100 μM to >2 mM, with 10 fragments having a K_d less than 1 mM. The hits were clustered into 3 chemotype groups but the hits also shared chemical similarities between groups, including a planar aromatic core and carboxylic acid substitution. Co-crystal structures of TIM-3 were determined for three

cluster 1 fragments revealing critical contacts between carboxyl groups coordinating with Ca^{2+} and making additional hydrogen bonding interactions with FG-CC' cleft backbone and side chains while the aromatic core hydrophobically interacts with solvent-exposed, flexible side chains. We were unable to generate co-crystal structures of cluster 2 and 3 hits to confirm their binding poses and further aid structure-based design of higher affinity analogs.

These results provide a reasonable starting point to pursue further compound optimization, in particular if those efforts were to focus on cluster 1 fragment hits. However, after careful binding site analysis, it was decided that medicinal chemistry efforts would be better allocated on different projects. The FG-CC' binding cleft has inherent flexibility that allows for the binding of both small molecule and protein natural ligands. This flexibility can confound medicinal chemistry efforts as binding poses can shift between iterations of compound optimization, complicating the design of higher affinity compounds. Although it is unclear what affinity threshold would be needed to achieve TIM-3 inhibition, this binding site did not provide sufficient optimism to warrant an expanded medicinal chemistry effort.

4.4 Methods

4.4.1 *Protein expression and purification.*

The gene encoding the IgV domain of human Tim-3 (residues 22-130 and 24-130) was synthesized with codon optimization for *E. coli* overexpression (GenScript). The construct was inserted into a vector (pET-28b+) for a tagless expression of the IgV domain. The IgV domain was overexpressed from BL21 (DE3) Gold strain *E. coli* into inclusion bodies. Protein production was induced with 1 mM IPTG when cultures reached

an OD600 of 0.8 and harvested after 4 h at 37˚C or overnight expression at 25˚C. Isotopically-labeled Tim-3 was prepared in M9 minimal media containing $^{15}NH_4Cl$. For resonance assignments, ^{13}C-glucose was used at 0.2 (w/v)% final concentration. The TIM-3 IgV domain was purified as previously described.[95] Briefly, cell pellets containing expressed human TIM-3 IgV were thawed and suspended in buffer before lysis by high pressure homogenizer. The lysate was centrifuged and TIM-3 was retained in inclusion bodies in the insoluble fraction. The pellet was washed by resuspension in buffer plus 0.1% Triton X-100, homogenized by sonication, and centrifuged. The insoluble fraction was washed and pelleted as described above in a high salt buffer containing 1.5 M NaCl, and then once more in the original buffer. The washed inclusion body pellet was weighed and dissolved in a buffer containing 8 M urea at room temperature for 1 hour before centrifugation to remove debris. Refolding of Tim-3 IgV was done by rapid dilution by drop-wise (~1 mL/min) addition of solubilized inclusion bodies into 10-25 volumes of refolding buffer containing 100 mM Tris pH 8.3, 0.4 M L-arginine, 2 mM EDTA, 2 mM reduced glutathione, and 0.2 mM oxidized glutathione. After incubating the refolding mixture overnight at 4˚C, it was dialyzed into a buffer of 20 mM Tris pH 7.5, 200 mM NaCl, and 1 mM EDTA. The dialysate was clarified by centrifugation and filtration before concentrated and loaded onto a HiPrep 26/300 Sephacryl S-75 column for size exclusion chromatography in an NMR buffer of 10 mM HEPES pH 7.4, 50 mM NaCl. Protein prepared for NMR screening was supplemented with 10 mM $CaCl_2$.

4.4.2 *NMR experiments.*

Nuclear magnetic resonance (NMR) screening experiments were performed at 25 °C using a 600 MHz Bruker Avance-III spectrometer equipped with a 5 mm single-axis x-

gradient cryoprobe and a Bruker Sample Jet. Gradient enhanced, two-dimensional ^{1}H-^{15}N heteronuclear multiple-quantum coherence spectra (SOFAST-HMQC) spectra were recorded on TIM-3 IgV domain (redidues 22-130; 24 scans, ~12 min).[133] Spectra were processed and analyzed using Topspin (Bruker). Our in-house fragment library of ~13,800 compounds was screened as mixtures of 12 fragments in a 96-sample format using 16 μM of ^{15}N-labeled TIM-3, 800 μM of each fragment, and 4% DMSO-d6 for spectrometer locking purposes. Hit mixtures were identified by comparing the chemical shifts of backbone resonances to a ligand-free TIM-3 reference spectrum. Because fragments were screened as mixtures, deconvolution of hit mixtures was necessary to isolate individual hit fragments. Deconvolution was accomplished by screening each twelve-compound mixture hit as a series of twelve singleton samples.

SOFAST-HMQC titration experiments were used to quantify the binding affinity of the best hits identified from the screen. The change in ^{1}H-^{15}N chemical shifts of backbone resonances upon stepwise addition of fragment was measured and fit by an in-house script.[128]

^{15}N and ^{13}C double-labeled TIM-3 IgV domain protein was expressed from *E. coli* in M9 minimal media containing $^{15}NH_4Cl$ and ^{13}C-glucose as the sole nitrogen and carbon sources, as described above. Triple resonance experiments HNCA, HNCO, HNCACO, and HNCOCA using $^{15}N/^{13}C$-TIM-3-IgV (0.8 mM) in 10 mM HEPES, 50 mM NaCl, pH 7.4 with 4% DMSO-d6, was performed at 25 ˚C on an 800 MHz Bruker Avance-III spectrometer equipped with a cryogenic probe. The data were processed using Topspin (Bruker) and analyzed by CcpNmr Analysis V2.4. Our assignments were in agreement with those published by Gandhi et al. soon after our assignment efforts were completed.

4.4.3 *Protein crystallization, data collection, and structure refinement.*

TIM-3 IgV domain (residues 24-130) was concentrated to 7-10 mg/mL and mixed with DMSO stock of desired ligand at a concentration of 4 mM and 4% DMSO and incubated on ice for 1h. FG-CC' cleft fragment-bound crystals were obtained in conditions containing 0.1 M TRIS pH 7.0-8.0 and 25% PEG 4000 or PEG 3350. Attempts to co-crystalize cluster 2 and 3 hits included screening around the above conditions varying buffer pH, PEG length, and concentration as well as commercially available sparse-matrix screens Index HT (Hampton) and JCSG Plus (Molecular Dimensions). Crystals were cryoprotected in mother liquor supplemented with 20% glycerol prior to freezing in liquid nitrogen. X-ray data were collected on the Life Sciences Collaborative Access Team (LS-CAT) Sector-21 beamlines at the Advanced Photon Source (APS), Argonne National Labs. Data were indexed, integrated, and scaled with HKL2000.[92] Molecular replacement with Phaser[93] was accomplished using Phenix[94] and the ligand-free TIM-3 structure previously determined (PDB ID: 6DHB) as the search model.[95] Structure refinement was accomplished with Phenix and included several rounds of manual model building with COOT. Final refinement and X-ray data collection statistics are provided below in Table 4-1. Figures have been prepared using PyMOL unless otherwise stated.[96]

4.4.4 *Molecular modeling: SiteMap and InducedFit docking.*

Maestro (Schrodinger) was used for molecular modeling, SiteMap, and InducedFit docking runs. TIM-3 structures 6DHB, 5F71, and the co-crystal structure of TIM-3 with **13** were prepared for modeling and docking using the Protein Prep Wizard by adding missing side chains, preparing charges in a pH 7 buffer, removing unbound waters, and conducting a restrained energy minimization. SiteMap analysis of the prepared proteins

was run under default conditions. A docking grid was generated around the bound **13** molecule in the FG-CC’ cleft. Hydrophobic residues F61, I117, and M118 were trimmed in the docking grid to allow for residue side chain flexibility. Cluster 3 fragments **10**-**12** were drawn in the 2D ligand builder and prepared for ligand docking using LigPrep. InducedFit docking was run under default conditions with a Ca^{2+} metal interaction constraint to avoid ambiguous ligand fitting in the FG-CC’ cleft.

Table 4-1. X-ray data collection and refinement statistics for TIM-3 co-crystal structures with **13**, **14**, and **2**.

Compound	**13**	**14**	**2**	**2**
VU #	VU0162042	VU0405931	VU0117985	VU0117985
Data Collection				
Space Group	P 21 21 2	P 21 21 21	C 1 21	P1
Cell Dimensions				
a, b, c (Å)	81.627, 84.860, 28.922	42.146, 44.523, 51.897	93.052, 52.066, 46.497	46.480, 52.049, 85.948
α, β, γ (˚)	90, 90, 90	90, 90, 90	90, 113.4, 90	90, 83.6, 90.1
Resolution (Å)	28.92 – 1.62 (1.68 – 1.62)	26.36 – 1.80 (1.83 – 1.80)	28.04 – 1.70 (1.73 – 1.70)	28.03 – 1.40 (1.42 – 1.40)
Rmerge (%)	9.0 (85.1)	6.5 (34.4)	5.7 (20.8)	8.0 (138)
Mean I / σI	29.5 (2.2)	54.0 (8.7)	47.3 (7.4)	17.8 (0.64)
Completeness (%)	100 (100)	98.9 (99.1)	99.2 (97.7)	91.1 (87.9)
Redundancy	11.0 (9.4)	11.9 (12.0)	6.2 (6.4)	3.0 (2.1)
Structure Refinement				
No. Reflections	26431	9373	22496	142650
R_{work} / R_{free}	0.2035 / 0.2260	0.1834 / 0.2343	0.2186 / 0.2621	0.2323 / 0.2609
R.m.s deviations				
Bond lengths (%)	0.006	0.006	0.007	0.010
Bond angles (˚)	0.938	0.860	0.951	1.688
Ramachandran				
Preferred regions (%)	92.45	92.45	93.81	93.23
Allowed regions (%)	7.55	7.55	5.24	6.65
Disallowed regions (%)	0	0	0.95	0.12

Related to Figures 4-6, 4-7, and 4-8. Highest resolution shell is in parentheses.

Chapter 5 - General Conclusions, Discussion, and Future Outlook

5.1 Goals addressed in this work.

Cancer immunotherapeutics capable of reversing immune evasion, an emerging hallmark of cancer, have recently revolutionized the way we treat cancer. Several monoclonal antibody (mAb) therapeutics targeting immune checkpoint proteins have been successful in trials and the clinic against a number of cancer types. These successes have been appropriately heralded within and beyond the immuno-oncology community, however there are specific concerning aspects related to the intrinsic properties of mAbs that have been under addressed. Namely, mAbs generally have suboptimal tissue and tumor penetration, can present unwanted immunogenicity issues, are associated with higher production and treatment costs, and have displayed a high frequency of immune-related adverse events (irAEs). Addressing these intrinsic drawbacks through alternative therapeutic modalities will offer oncologists better options for treating their patients.

We sought to address the concerns of treating patients with immune checkpoint targeting mAbs by discovering and designing small molecule inhibitors that can achieve inhibition of immune checkpoint cognate receptor binding. Small molecule inhibitors present potential advantages over therapeutic mAbs including improved tissue and tumor penetration, reduced production costs, and oral bioavailability. Furthermore, the pharmaceutical and pharmacokinetic properties of small molecule inhibitors are more readily modulated compared to their mAb counterparts, allowing for the design of a compound that clears more rapidly than mAbs minimizing irAEs. The report of small molecules that target immune checkpoints has been limited to date, despite the potential

advantages outlined, likely due to the consideration that immune checkpoint proteins rely on protein-protein interaction interfaces that are difficult to target with small molecules and may be “undruggable.” The goal of this dissertation was to utilize fragment-based methods to assess the druggability of the immune checkpoint proteins TIGIT and TIM-3 and to discover novel hit-to-lead compounds that can serve as starting points for the design of potent inhibitors.

5.2 TIGIT is undruggable by small molecules.

We screened TIGIT against our fragment library and identified 67 weakly binding hits. These hits were identified against a TIGIT C69S screening construct designed to reduce potential covalent adduct false positives. Upon further testing of these hits against TIGIT WT, it was found that all but one of the identified fragments did not bind suggesting we unintentionally introduced a fragment binding site in the C69S screening construct. The lone hit that bound to TIGIT WT induced extensive resonance peak broadening that suggests compound-mediated dimerization or oligomerization. This dimerization could lead to inhibition of the TIGIT-PVR interaction *in vivo*, however the lone hit without structural information of binding presents a problematic starting point that was deemed not worthy of further exploration by our lab. We concluded that a rescreen of TIGIT WT was not necessary given the structural similarities between WT and C69S constructs.

From a broader perspective, the TIGIT-PVR immune checkpoint signaling pathway could be inhibited by targeting PVR instead of TIGIT. The TIGIT-PVR lock-and-key interaction hinges on each partner providing a C’C” loop hydrophobic “lock” and an aromatic “key” residue in the FG loop. Based on the lack of fragment hits found against the TIGIT lock-and-key motifs, it may follow that the PVR lock-and-key motifs are similarly

difficult to target by small molecule. While this is a speculative assumption, it is a potentiality that was taken into consideration when our lab decided to not pursue further investigation to develop inhibitors for the TIGIT-PVR axis. It is our belief that further investigation in inhibiting the TIGIT-PVR signaling pathway with small molecules would be better focused on downstream signaling proteins.

5.3 TIM-3 C”D-binding compounds have several potential utilities.

5.3.1 *Summary of work on TIM-3 C”D-binding compounds.*

Fragment screening of TIM-3 resulted in a diverse set of confirmed fragment hits that were found to bind to two different binding sites. An unbiased screen of the TIM-3 IgV domain identified 101 fragments hits and subsequent crystallography revealed a novel binding site located in the C”D loop region distal from the accepted FG-CC’ active site. The C”D binding site consists of two non-conserved tryptophan residues that orient in a dual pi-pi stacking interaction with binding fragments sandwiched between the indole side chains. The starting chemical matter found in the screen was of good affinity and a triazoloquinasolinone fragment was chosen as a chemically tractable starting point for hit-to-lead optimization. Iterative rounds of medicinal chemistry informed by both SAR by NMR and structure-based design were successful in vastly improving the binding affinity of compounds in this series. Our lead compound has an affinity of 70 nM, representing an 11,500-fold increase in affinity over our starting fragment hit.

With a high-affinity ligand in hand, we briefly explored the significance of compound binding at the C”D site. In summary, our compounds did not show allosteric inhibition of PtdSer, galectin-9, or CEACAM-1 binding. While these results are discouraging, we do not believe the battery of experiments conducted provide conclusive

evidence to rule out allosteric inhibition of TIM-3 binding to its ligands galectin-9 and CEACAM-1 and hope to further explore this idea through future collaborations. However, it is clear to us that compound binding does rigidify the structural dynamic C"D loop region.

5.3.2 *Potential for allosteric TIM-3 modulation.*

Our compounds that bind the C"D binding site were unable to block natural ligand binding, however this does not exclude this site from being potentially important for activation or inhibition of TIM-3. As mentioned previously, the specific structural dynamics that underlie TIM-3 activation upon natural ligand binding remain elusive, though it is thought that ligand binding causes a conformational change that will eventually lead to the phosphorylation of two tyrosine residues (Y265 and Y272) on the cytoplasmic tail.[119,120] A recent *in silico* molecular dynamics study of the IgV domain upon PtdSer binding revealed an interesting conformational change in the C"D loop region.[136] Their proposed mechanism for PtdSer -induced conformational change in the IgV domain proceeds via two stages. The first stage involves the opening of the FG-CC' cleft and formation of a salt bridge between E62 and R69 resulting in the freed C" strand residue Y77 from the internal hydrophobic core of the protein. The second stage proceeds with the solvent exposed Y77 collapsing back into a hydrophobic pocket centered at W83. Although it is unclear if these specific conformational dynamics trigger TIM-3 activation, these results suggest that conformationally rigidifying the C"D allosteric site with our compounds could lead to a modification of typical TIM-3 activity.

5.3.3 *Relevance of TIM-3 flexible loops.*

Considering that the demonstrated flexible regions of the TIM-3 IgV domain are all loops, an examination of the relevance of these regions is warranted. A functional

relevance for the BC loop has been suggested in mouse TIM family members that are bind to PtdSer. In mice, it has been demonstrated that mTIM-3 recognizes PtdSer -presenting apoptotic cells through the Ca^{2+} coordinated FG loop and is crucial for the clearance of these cells by phagocytes.[137] A model for binding of mTIM-4 to membrane-associated PtdSer suggests that the BC loop would be proximal to the membrane surface mediated by electrostatic interaction with charged phosphate head of membrane phospholipids (Figure 5-1A). Indeed, mutation of an arginine residue in the BC loop of mTIM-1 and mTIM-4 to alanine, R22A and R25A respectively, decreased PtdSer liposome binding by ~50% (Figure 5-1B).[113] The BC loop of mTIM-3 is does not contain positively charged residues, but contains **uncharged polar** side chains (42-LP**TS**G**T**-47) that can stabilize BC loop interaction with membrane phospholipid phosphate heads. The BC loop of human TIM-3 is almost completely devoid of **polar** residues (42-PAAPG**N**-47) and would likely not significantly contribute to the stabilizing TIM-3 binding to membrane-associated PtdSer (Figure 5-1C). The crystal structure of mTIM-3 and PtdSer revealed that the tip of the CC' loop (60-WSQ-62) directly interacts with PtdSer during binding (Figure 5-1D). Interestingly, substitution of these residues with the hTIM-3 residues (60-VFE-62) significantly decreased PtdSer binding activity (Figure 5-1E).[113] Both of the non-conserved BC loop and CC' tip regions in hTIM-3 appear to reduce overall affinity for PtdSer compared to mTIM-3.

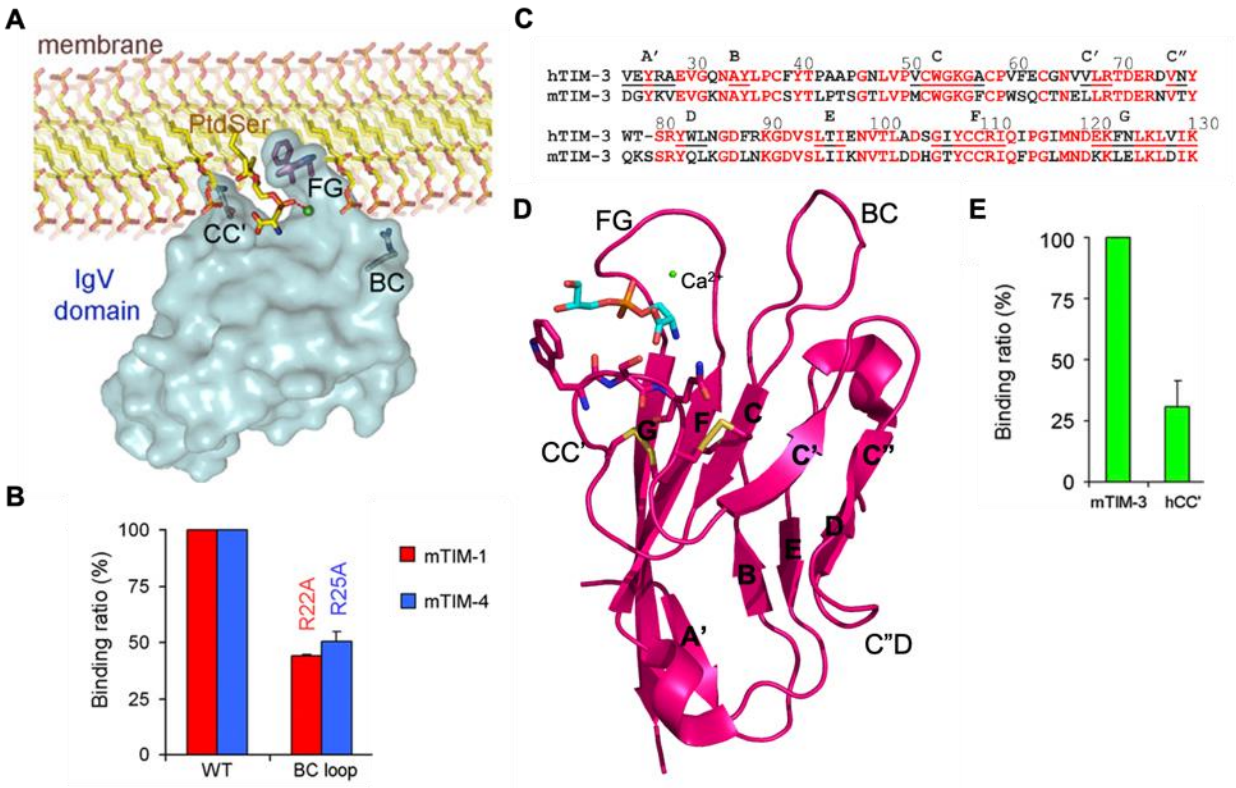

Figure 5-1. Contributions of BC and CC' loops to PtdSer binding in mouse TIM proteins.
(A) Model of the IgV domain of mTIM-4 bound to PtdSer (surface, PDB ID 3BIB) within a phospholipid bilayer membrane. BC loop residue R25 is shown as sticks making an electrostatic interaction with the headgroups of phospholipids. (B) Relative binding to the wild-type mTIM-1 and mTIM-4 proteins of mutants with the indicated residue substitution in the BC loop. (C) Sequence alignment of human and mouse TIM-3 IgV domains. Conserved residues are red the β-strands are labeled above the sequences and underlined in red and black for conserved and no-conserved, respectively. (D) Co-crystal structure of mTIM-3 (magenta, PDB ID 3KAA) bound to PtdSer (cyan sticks). CC' loop tip residues (60-WSQ-62) are shown as sticks. (e) Relative binding of the mutant hCC' (WSQ → VFE) to PtdSer liposomes compared with that of the wild-type mTIM-3. Adapted from DeKruyff et al, 2010.[113]

A functional relevance for the C"D loop has yet to be identified. While the sequences of mTIM-3 and hTIM-3 are largely conserved, it is noteworthy that the C"D region is the least conserved region (Figure 5-1C) and mTIM-3 does not contain the two tryptophan residues that facilitate compound binding at the C"D site. Furthermore, it is unclear if mTIM-3 would have a similar flexibility in the C"D region exhibited by hTIM-3. An overlay of high resolution mTIM-3 and hTIM-3 reveals a largely shared global fold and similar loop positions (Figure 5-2). The only notable exception to the shared fold is in the C"D loop where mTIM-3 has an additional nonconservced lysine residue (K79). This

additional residue introduces a kink in the loop that separates the main chain loop position from hTIM-3 by ~4 Å. A closer examination of the mTIM-3 C”D loop region shows that K79 backbone carbonyl makes a water-mediated hydrogen bond with Y77 not present in hTIM-3 despite nearly identical Y77 positioning. This mTIM-3-specific interaction may confer more rigidity into the C”D loop of mTIM-3 compared to hTIM-3.

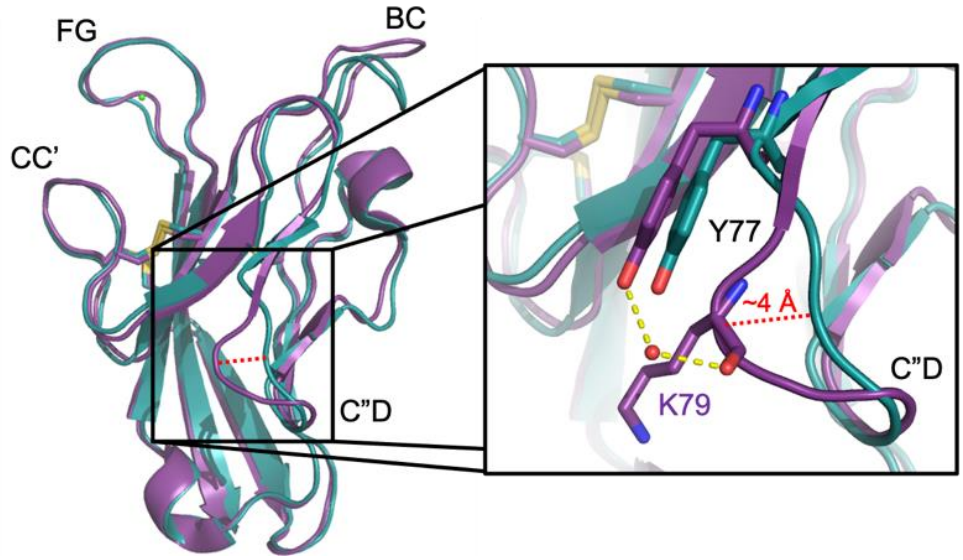

Figure 5-2. Structural comparison of mTIM-3 and hTIM-3 IgV domains.
Aligned and overlayed structures of mTIM-3 (purple) and hTIM-3 (dark green) IgV domains displaying similar global folds with loops labeled. C”D loop repositioning from mTIM-3 and hTIM-3 is labeled with a red dotted line. The inset contains a close-up look at the differences between the two C”D loop positions. Notable residues are shown as sticks and labeled, hydrogen bonds are shown as yellow dashed lines, and crystallographic water is shown as a red sphere.

Collectively, the non-conserved and flexible regions in hTIM-3 seem to represent a divergence away from PtdSer binding and phagocytotic function towards an expanded immuno-modulatory role with multiple binding partners which has only been demonstrated in hTIM-3 models. Given the demonstrated flexibility of the non-conserved hTIM-3 C”D loop, it seems logical that this region may represent an adaptation away from mTIM-3 that contributes to hTIM-3 immuno-regulatory functions. These insights help justify an exploration into the consequences of rigidification of the C”D loop as rigidification may result in an active, inactive, or neutral conformational state. To this end,

the effects of compound binding at the C”D binding site on downstream signaling pathways is a particularly interesting area of future investigation.

5.3.4 *Alternative methods of receptor inhibition.*

The primary focus of most drug discovery efforts is ligand or substrate inhibition either directly at the target’s active site or through an allosteric site that can affect the conformation of the active site and disrupt ligand binding. However, these efforts are not all encompassing of the different routes to inhibition. Although ligand inhibition remains the primary focus of our efforts to inhibit TIM-3, below I will discuss two potential alternative inhibition methods that rely on removing TIM-3 receptors from the cell surface and do not require inhibitor binding to the active site or allosteric modulation.

Receptor endocytosis can occur through different pathways and many, but not all receptors, undergo endocytosis upon ligand or antibody binding. Immune checkpoint receptors PD-1, PD-L1, and CTLA-4 have all been previously shown to be internalized after antibody binding and suggesting this internalization contributes to their immune modulation.[138–140] Similarly, a recent report identifies a novel blocking antibody for TIM-3 that blocks interaction with PtdSer but not galectin-9 and induces the potent internalization of TIM-3. In activated T cells, antibody-induced endocytosis was robust enough to shut down the entire TIM-3 mediated signaling pathway regardless of ligands.[141] While reports of antibodies that induce receptor endocytosis may be more prevalent and not surprising, reports of small molecules that achieve the same result are rare. One such small molecule has been identified that induces the dimerization and subsequent internalization of PD-L1. The mirrored symmetrical compound ARB-272572 (compound A) was identified from a small molecule screen of PD-1/PD-L1 interaction

(Figure 5-3A).[142] Further crystallographic analysis of this compound led to identifying that compound A stabilizes the formation of a PD-L1 homodimer (Figure 5-3B). Ultimately, homodimerization of PD-L1 induces rapid internalization of the receptors which are not recycled back to the cell surface (Figure 5-3C). Compound A provides a proof of concept that small molecule induced endocytosis is possible with immune checkpoint inhibitors.

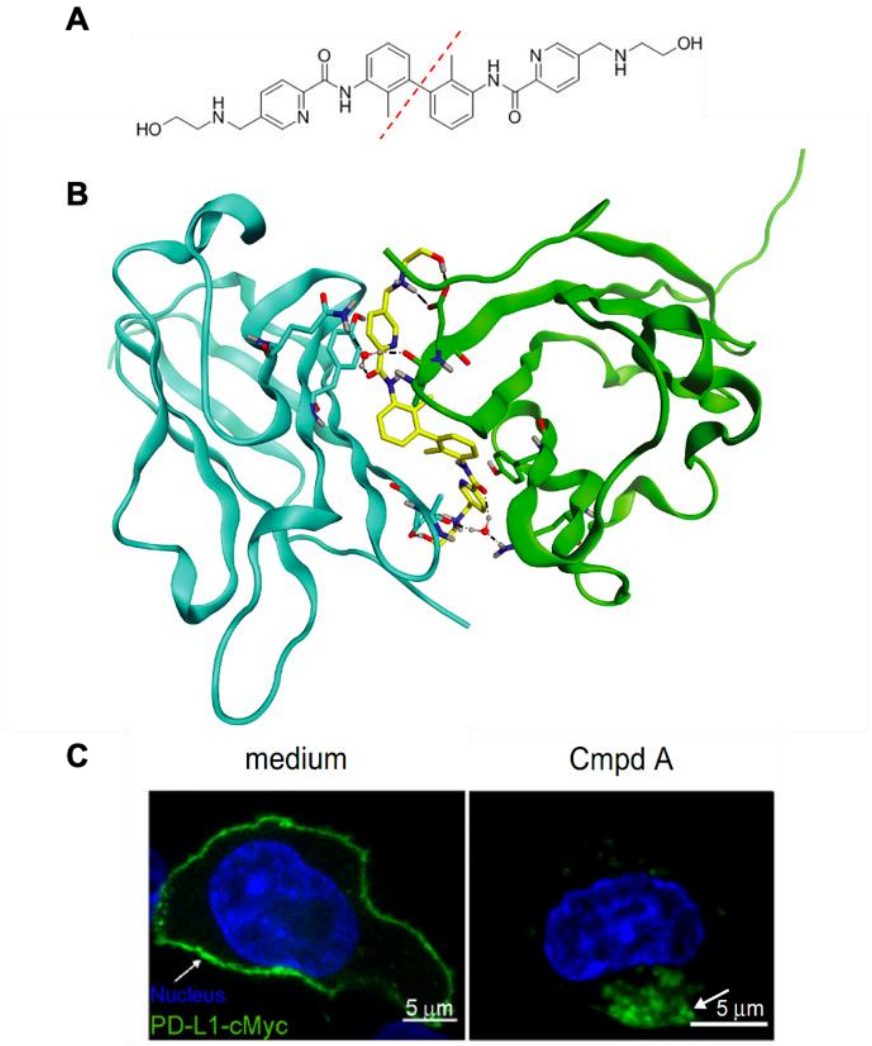

Figure 5-3. Small molecule induced endocytosis of PD-L1.
(A) Structure of compound A with a red dashed line indicating mirrored symmetry. (B) Co-crystal structure of compound A (yellow sticks) at the dimeric PD-L1 interface. PD-L1 in ribbon are colored cyan and green for chains A and B, respectively. (C) CHO-K1 cells transfected with cMyc-PD-L1 and labeled with anti-cMyc Alexa Fluor 488-conjugated antibody followed by incubation with compound A. The confocal fluorescence microscopy detects PD-L1-cMyc (green) and nucleus (blue). The right panel depicts internalized PD-L1 in the cytosol after 1 h of treatment with compound A. Adapted from Park et al., 2021.[142]

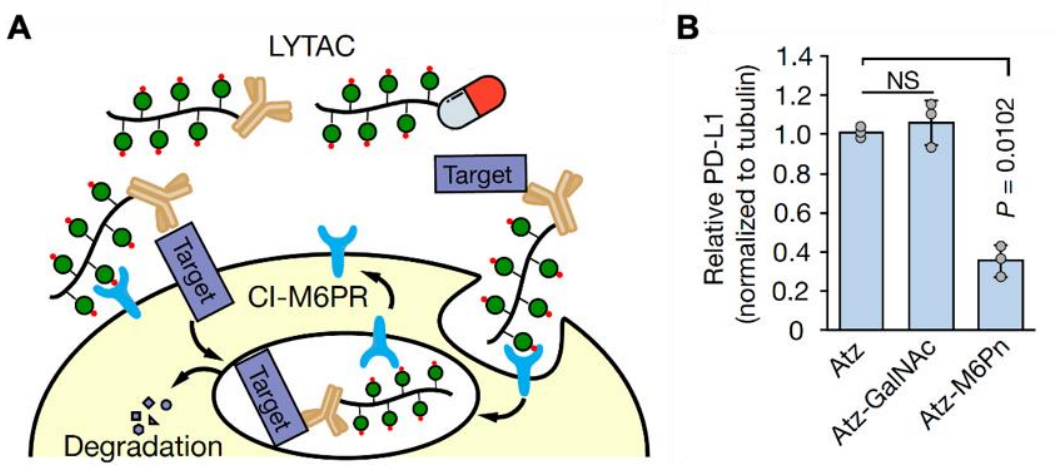

Figure 5-4. LYTACs traffic extracellular targets to lysosomes for degradation via CI-M6PR. (A) The concept of LYTACs, in which a glycopeptide ligand for CI-M6PR is conjugated to an antibody or small molecule ligand to traffic secreted and membrane-associated proteins to lysosomes. (B) PD-L1 levels in HDLM-2 cells after treatment with 25 nM Atz, Atz-GalNAc (negative glycopolypeptide control), or atz-LYTAC for 48 h. Adapted from Banik et al., 2020.[143]

Proteolysis targeting chimeras (PROTACs) are heterobifunctional degraders that bring together a protein of interest and an E3 ubiquitin ligase to induce ubiquitination and subsequent degradation of the ubiquitinated protein. This chemical knockdown strategy for regulating protein levels through hijacking the ubiquitin-proteasome system has been successful in both academic and clinical settings.[144,145] However, the PROTAC strategy is limited to intracellular proteins that can access the ubiquitin-proteasome system, excluding extracellular and membrane-associated proteins. Recently, this hurdle was overcome with lysosome targeting chimeras (LYTACs), which consist of a small molecule or antibody fused to a chemically synthesized glycopeptide ligands that are agonist of the lysosome-targeting receptor cation-independent mannose-6-phopate receptor (CI-M6PR) (Figure 5-4A). They demonstrated that glycopeptides bearing multiple serine-*O*-mannose-6-phosphonate (M6Pn) residues could be conjugated to biotin and membrane protein antibodies, including antiPD-L1 atezolizumab (Atz), and the glycopolypeptides would efficiently traffic the target proteins to CI-M6PR for lysosomal degradation (Figure 5-4B).[143] This work has been recently expanded upon to show that alternative lysosome-

targeted receptors can be used to introduce cell-specificity. A LYTAC conjugated with triantenerrary *N*-acetylgalactosamine engages the liver-specifc asialoglycoprotien receptor to degrade extracellular proteins in a cell-specific manner.[146] These proof of concept studies show that LYTACs can mediate the degradation of membrane-associated proteins of therapeutic interest.

One important feature of both small molecule induced endocytosis and LYTAC strategies is that they are not dependent upon ligands that bind the active site of a membrane protein. Both methods only require ligands of sufficient affinity that can be conjugated to potentially induce dimerization or with a glycopeptide to facilitate recruitment to a lysosome-targeting receptor. In the context of TIM-3, disruption of ligand binding through direct or allosteric effects is the primary goal, however, the proof of concepts discussed above may offer favorable secondary strategies. The compounds described in Chapter 3 provide an important starting point for the design of analogs to explore TIM-3's potential for small molecule induced dimerization and endocytosis or receptor degradation through a LYTAC strategy. One can imagine a symmetrical compound of two copies of **38** chemically linked through the solvent exposed 2-position of the triazoloquinazolinone core (Figure 5-5A). Such a compound could engage the C"D sites of two TIM-3 IgV domains and bring them within close proximity. The binding of this compound itself may induce receptor internalization, but could also introduce steric hindrances to ligand binding. Similarly, the 2-position of the triazoloquinazolinone core could be conjugated with a lysosome targeting receptor ligand, like glycopolypeptide M6Pn, to asses if TIM-3 could be trafficked to lysosome degradation pathways (Figure 5-5B). Our C"D binding compounds provide an important starting point for the design of

analogs to explore TIM-3's potential for small molecule induced dimerization and endocytosis or receptor degradation through a LYTAC strategy.

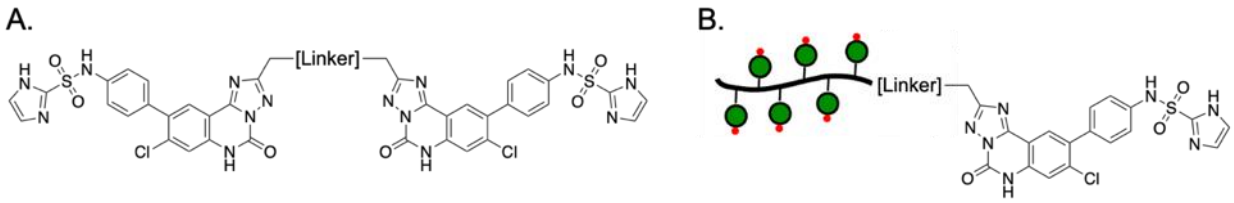

Figure 5-5. Proposed TIM-3 dimerizing and LYTAC compounds.
(A) A mirrored symmetrical compound composed of two copies of compound **38** that could theoretically engage two TIM-3 receptors simultaneously and induce receptor internalization. (B) Glycopeptide M6Pn could be linked to **38** creating a heterobifunctional compound that could direct TIM-3 into lysozyme degradation pathways via M6Pn interaction with CI-M6PR.

5.4 Developing TIM-3 FG-CC' small molecule inhibitors will be difficult

5.4.1 *Summary of work on TIM-3 FG-CC'-binding compounds.*

A targeted fragment screen of the FG-CC' binding cleft coordinated with calcium was conducted to identify chemical matter that directly binds to the more pharmacologically relevant FG-CC' active site. Our targeted screen designed to identify fragments that interact with the TIM-3 FG-CC' cleft in a calcium-dependent manner found 61 mostly carboxylic acid containing fragment hits that were grouped into three differenent chemotype clusters. NMR titrations were used to obtain the binding affinities of these fragments and revealed only 3 hits had an affinity better than 0.5 mM. Despite the collective lower affinity of these fragments, co-crystal structures of TIM-3 and fragment hits revealed critical contacts between carboxyl groups coordinating with Ca^{2+} and making additional hydrogen bonding interactions with FG-CC' cleft backbone and side chains while the aromatic fragment cores hydrophobically interact with solvent-exposed, flexible side chains. We decided to forgo further medicinal chemistry on these compounds based on limited allocatable chemistry resources, but I will discuss the potential for cluster 1 fragment expansion below.

5.4.2 *Potential expansion of cluster 1 fragments.*

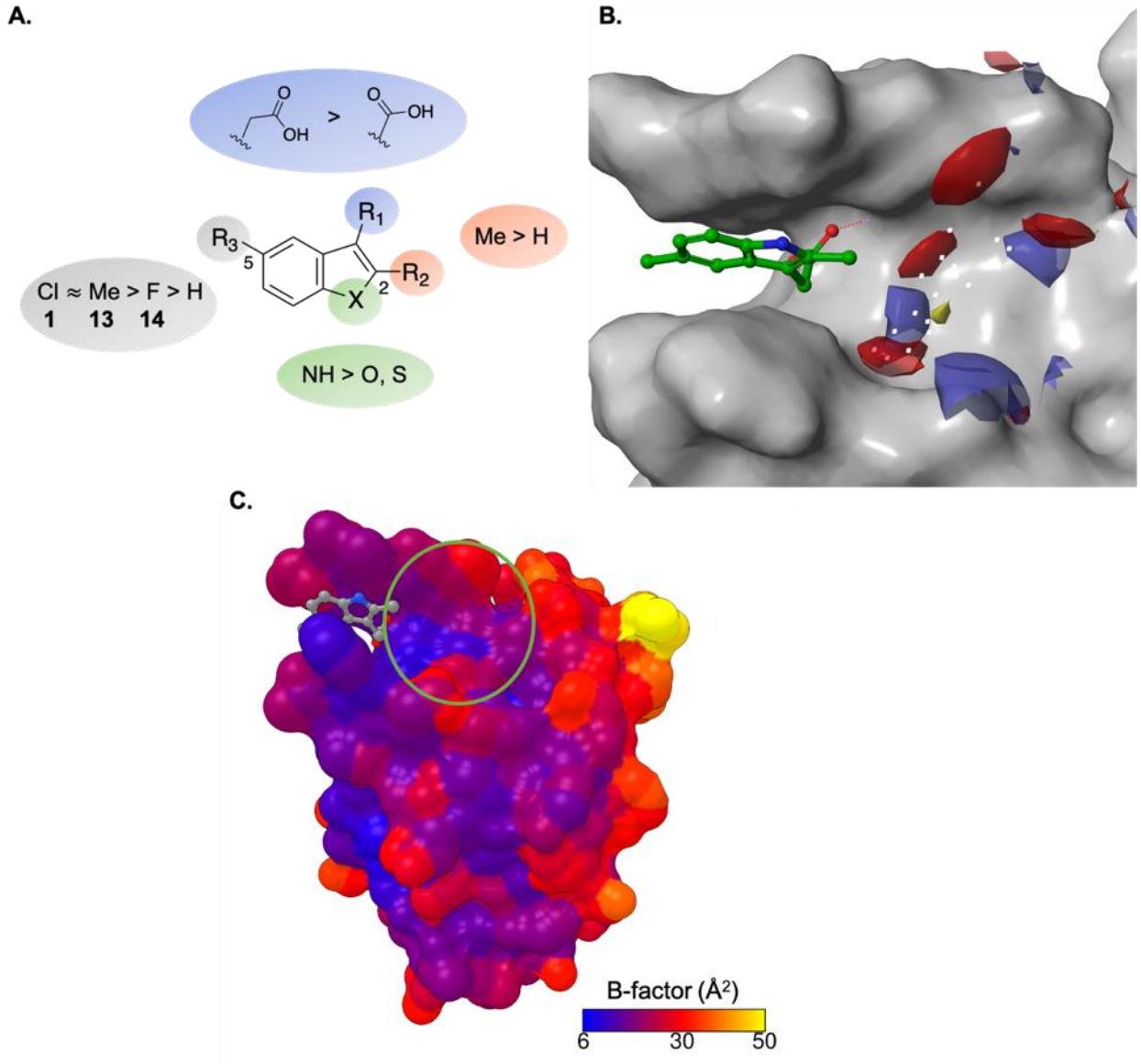

Figure 5-6. Cluster 1 analysis for potential medicinal chemistry expansion.
(A) SAR of cluster 1 fragment hits. (B) Potential druggable expansion site as defined by SiteMap shown as H-bond acceptor (red), H-bond donor (blue), and hydrophobic (yellow) surfaces (image prepared in Maestro). (C) Co-crystal structure of TIM-3 and **13** represented with surface maps colored with atomic B-factor values (scale in inset, image prepared in UCSF Chimera). The proposed expansion site by SiteMap adjacent to **13** is highlighted with a green circle.

Cluster 1 fragments were chosen for a characterization of potential expansion based on a combination of superior binding affinities, ligand efficiencies, and availability of structural information making them more favorable as starting points for optimization by medicinal chemistry. Although few matched pairs exist within the cluster 1 hits, general

SAR observations can be made by comparing the binding affinities of 5,6-fused fragments (Figure 5-6A, Appendix II). Acid substitution is preferred on the 5-member ring over the 6-member ring and acetic acid is favored over carboxylic acid. Indole cores appear to be favorable to benzofuran and benzothiophene cores. Methyl substitution at 2- and 5-positions resulted in improved binding affinities. Furthermore, the matched set of compounds **1**, **13**, and **14** with 5-chloro, methyl, and fluoro substitutions, respectively, revealed that the bulkier substituents of chloro and methyl are preferred to smaller substitutions at the 5-position.

A SiteMap analysis of the TIM-3/**13** co-crystal structure revealed a potentially druggable site adjacent to the 5-methyl of **13** (Figure 5-6B). This site was given a SiteScore of 0.66, below the 0.8 threshold that is suggested to distinguish between a drug-binding and a non-drug-binding site. This site could be characterized as a largely hydrophilic, shallow expanse consisting of the portions of the F and C strands. There is very little hydrophobic space in this binding site which would limit affinity-boosting expansion moieties on the 5-position to various hydrogen bond accepting or donating substitutions. Low B-factors in the proposed expansion site suggest a highly structured region, which may correspond with limited side chain flexibility (Figure 5-6C). A highly structured expansion site may be beneficial in designing new compounds as limited flexibility confers fixed side chain positions to target for new intermolecular contacts, however, this can also limit the potential vectors and interactions achievable without ligand-induced changes in this site.

A medicinal chemistry strategy to improve the compound binding affinity with cluster 1 fragments would focus on two facets. Firstly, substitutions of the indole core and

core modifications should be explored to expand the hydrophobic interface with the FG-CC' hydrophobic clamp. Hydrophobic space is limited at this site and potential for hydrophobic interaction should be maximized within the clamp. Aromatic core swapping or core substitution can be used to optimize the pi-electronics for pi-pi stacking. For instance, electron-withdrawing substituents are predicted to strengthen pi-pi interactions when introduced to one of its partners by decreasing the repulsion between the two pi systems.[147] Secondly, exploratory substitution off the 5-position of the indole core should focus on various hydrogen bond donors or acceptors that could interact with backbone or side chains in the SiteMap proposed expansion site. It is also feasible that compounds could be designed to displace or engage the Ca^{2+}-coordinated water. Although a chemically tractable path forward is presented here, it was ultimately decided that medicinal chemistry resources would not be allocated to this site based on concerns of highly flexible side chains in the FG-CC' binding site, the flexibility of the CC' loop that can accommodate small molecule and protein ligand alike, limited hydrophobic space for expandability, an expansion site that would predominantly rely on additional hydrogen bonding interactions for affinity improvement, and the difficulties previously outlined in obtaining consistent and reliable crystal structures to guide compound design.

Direct inhibition of ligand binding at the FG-CC' site would be the preferred method to inhibit TIM-3 activity. However, our studies have established that this site is likely highly difficult to target with small molecules. The discovery and design of larger peptidomimetics capable of coordinating calcium and engaging a larger interaction face within the FG-CC' cleft and surrounding protein surface could be a fruitful path forward in

targeting the active site. To this end, the fragment hits identified in our screen could serve as useful starting points to aid the design of peptidomimetic libraries for screening.

5.5 Concluding Remarks

In conclusion, these results represent the first reported examples of using fragment-based methods to assess druggability and identify small molecule ligands for the immune checkpoint proteins TIGIT and TIM-3. Immune checkpoint proteins are predicted to be challenging targets for small molecule inhibition. We have shown that this is true for TIGIT, however, we were able to identify and optimize compounds that bind to TIM-3 with nanomolar affinity. While the ultimate utility of our high affinity TIM-3 compounds has yet to materialize, the compounds described herein represent important tool compounds to explore the pharmacological relevance of the C”D site and critical starting points for the further design of potential inhibitors using an allosteric, dimerization, or LYTAC strategy. These results collectively suggest that although immune checkpoint proteins are difficult drug targets, they could be druggable with small molecules and deserve experimental validation.

APPENDIX I – Fragment hit clustering from unbiased TIM-3 NMR screen

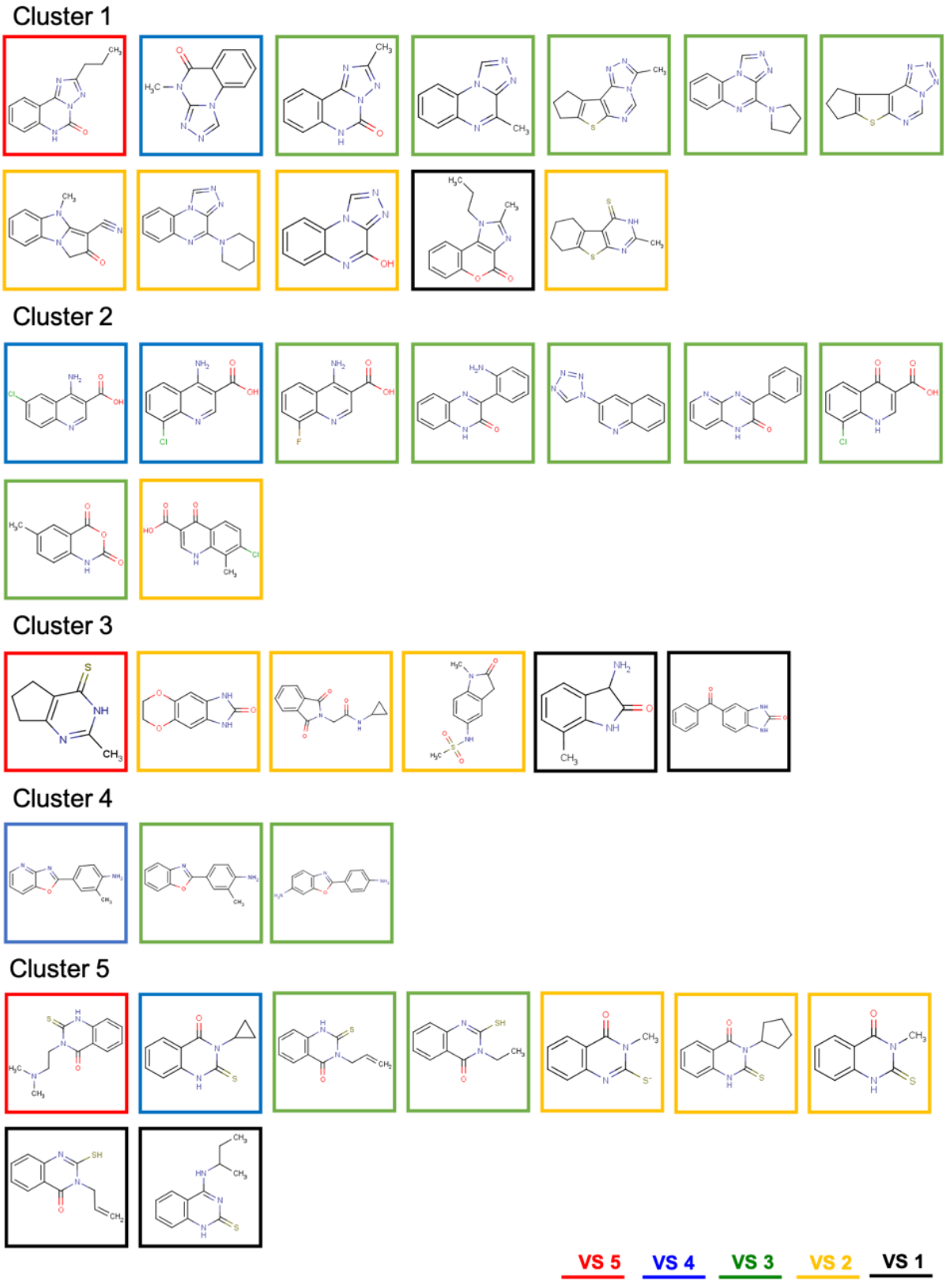

Cluster 6

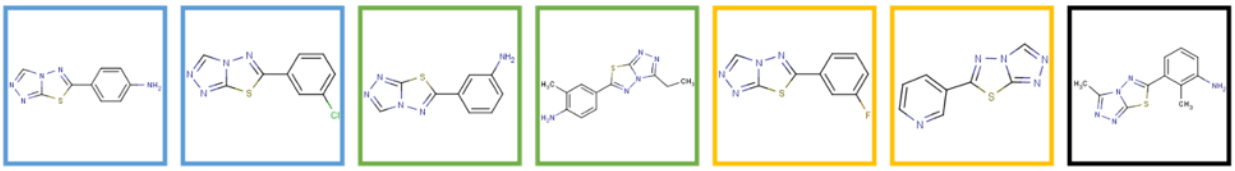

Cluster 7

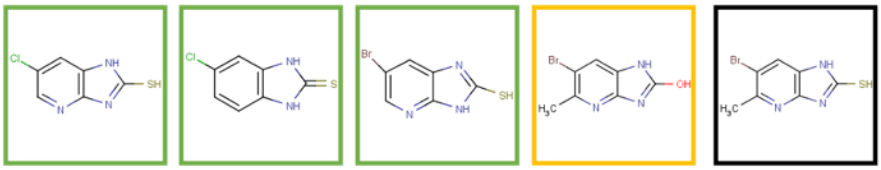

Cluster 8

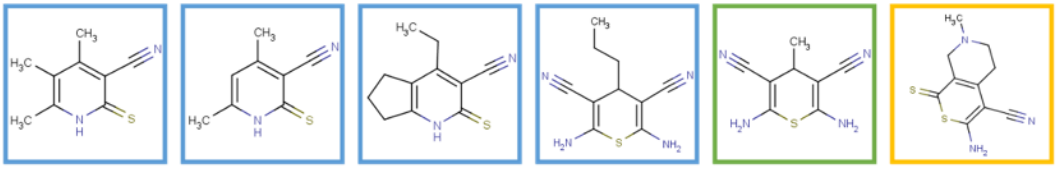

Cluster 9

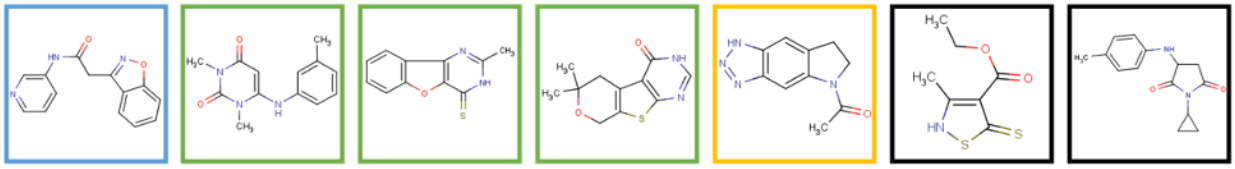

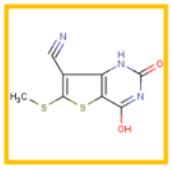

Cluster 10

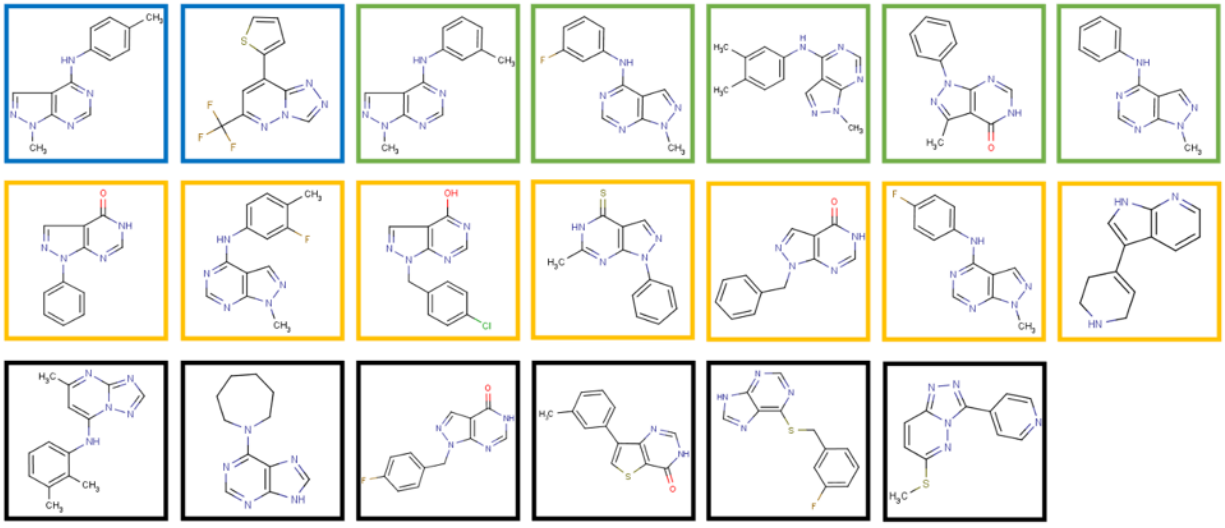

VS 5 VS 4 VS 3 VS 2 VS 1

Cluster 11

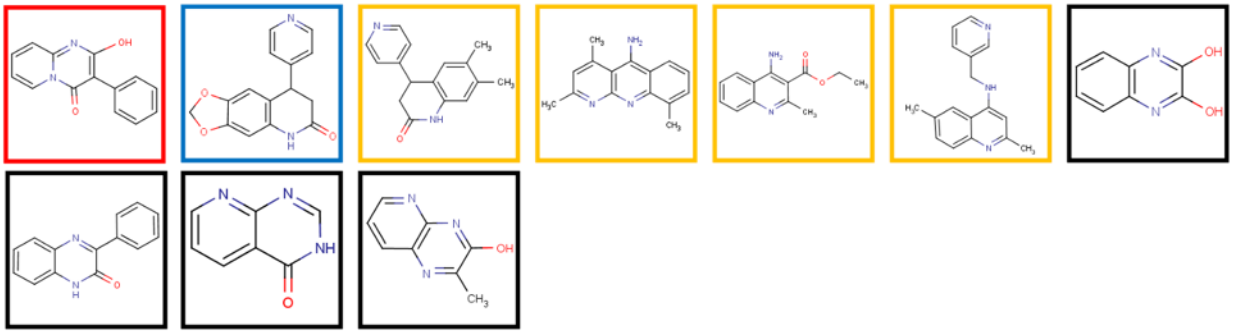

Cluster 12

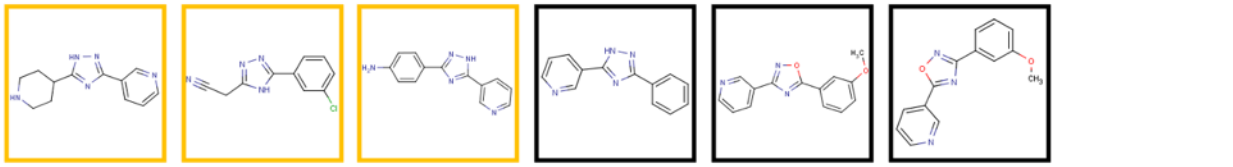

VS 5 VS 4 VS 3 VS 2 VS 1

APPENDIX II – Cluster 1 fragment hits from targeted NMR screen for SAR analysis

Compound	Structure	NMR Kd (mM)	Ligand Efficancy
1	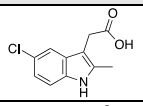	0.28	0.32
13	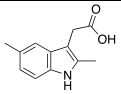	0.36	0.31
14	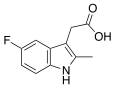	0.58	0.29
2	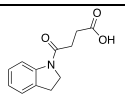	0.72	0.27
15		0.73	0.29
4	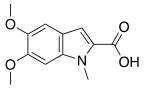	0.93	0.24
6		1.06	0.24
3		1.09	0.20
16	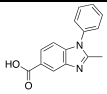	1.35	0.21
17	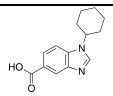	1.44	0.20
18	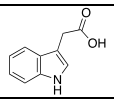	1.59	0.29
19	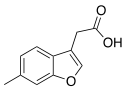	1.59	0.27
20	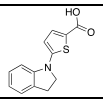	> 2.0	ND
21	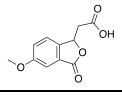	> 2.0	ND
22	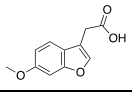	> 2.0	ND
23	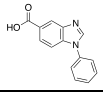	> 2.0	ND
24	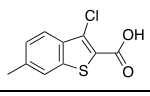	> 2.0	ND

Compound	Structure	NMR Kd (mM)	Ligand Efficancy
25	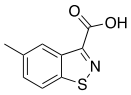	> 2.0	ND
26	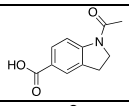	> 2.0	ND
27	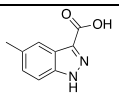	> 2.0	ND
28	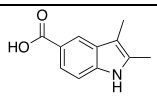	> 2.0	ND
29	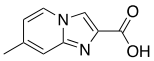	> 2.0	ND
30	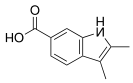	> 2.0	ND
31	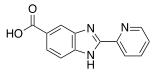	> 2.0	ND
32	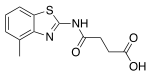	> 2.0	ND
33	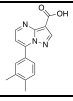	> 2.0	ND
34	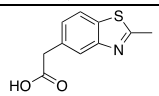	> 2.0	ND
35	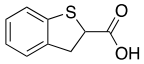	> 2.0	ND
36	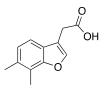	> 2.0	ND
37	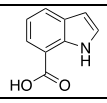	> 2.0	ND
38	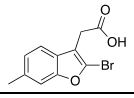	> 2.0	ND
39	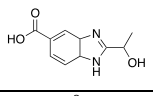	> 2.0	ND
40	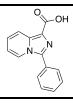	> 2.0	ND
41	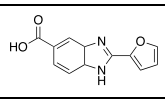	> 2.0	ND

REFERENCES

1. Siegel, R. L., Miller, K. D., Fuchs, H. E. & Jemal, A. Cancer statistics, 2022. *CA. Cancer J. Clin.* **72**, 7–33 (2022).
2. Financial Burden of Cancer Care | Cancer Trends Progress Report. Available at: https://progressreport.cancer.gov/after/economic_burden. (Accessed: 21st February 2022)
3. AACR. Cancer Progress Report 2018. (2018).
4. Hanahan, D. & Weinberg, R. A. The Hallmarks of Cancer. *Cell* **100**, 57–70 (2000).
5. Mardis, E. R. & Wilson, R. K. Cancer genome sequencing: A review. *Hum. Mol. Genet.* (2009). doi:10.1093/hmg/ddp396
6. Dugger, S. A., Platt, A. & Goldstein, D. B. Drug development in the era of precision medicine. *Nat. Publ. Gr.* **17**, (2017).
7. Schilsky, R. L., Allen, J., Benner, J., Sigal, E. & McClellan, M. Commentary: Tackling the Challenges of Developing Targeted Therapies for Cancer. *Oncologist* **15**, 484–487 (2010).
8. Fisher, R., Pusztai, L. & Swanton, C. Cancer heterogeneity: Implications for targeted therapeutics. *Nature* **509**, 479–485 (2014).
9. Housman, G. *et al.* Drug resistance in cancer: an overview. *Cancers (Basel).* **6**, 1769–92 (2014).
10. Hanahan, D. & Weinberg, R. A. Hallmarks of cancer: the next generation. *Cell* **144**, 646–74 (2011).
11. Sharma, P. & Allison, J. P. Immune checkpoint targeting in cancer therapy: Toward combination strategies with curative potential. *Cell* **161**, 205–214 (2015).

12. Swann, J. B. & Smyth, M. J. Immune surveillance of tumors. *Journal of Clinical Investigation* **117**, 1137–1146 (2007).

13. Gonzalez, H., Hagerling, C. & Werb, Z. Roles of the immune system in cancer: From tumor initiation to metastatic progression. *Genes and Development* **32**, 1267–1284 (2018).

14. Pardoll, D. M. The blockade of immune checkpoints in cancer immunotherapy. *Nature Reviews Cancer* **12**, 252–264 (2012).

15. Chen, D. S. & Mellman, I. Oncology Meets Immunology: The Cancer-Immunity Cycle. *Immunity* **39**, 1–10 (2013).

16. Wherry, E. J. & Kurachi, M. Molecular and cellular insights into T cell exhaustion. *Nat. Rev. Immunol.* **15**, 486–499 (2015).

17. Pauken, K. E. & Wherry, E. J. Overcoming T cell exhaustion in infection and cancer. *Trends in Immunology* **36**, 265–276 (2015).

18. Leach, D. R., Krummel, M. F. & Allison, J. P. Enhancement of antitumor immunity by CTLA-4 blockade. *Science (80-.).* (1996). doi:10.1126/science.271.5256.1734

19. Ribas, A. & Wolchok, J. D. Cancer immunotherapy using checkpoint blockade. *Science* (2018). doi:10.1126/science.aar4060

20. Zarour, H. M. Reversing T-cell dysfunction and exhaustion in cancer. *Clin. Cancer Res.* **22**, 1856–1864 (2016).

21. Parakh, S., King, D., Gan, H. K. & Scott, A. M. Current development of monoclonal antibodies in cancer therapy. in *Recent Results in Cancer Research* **214**, 1–70 (Springer New York LLC, 2020).

22. Couzin-Frankel, J. Breakthrough of the year 2013. Cancer immunotherapy.

Science (2013). doi:10.1126/science.342.6165.1432

23. Maleki Vareki, S., Garrigós, C. & Duran, I. Biomarkers of response to PD-1/PD-L1 inhibition. *Critical Reviews in Oncology/Hematology* **116**, 116–124 (2017).
24. Larkin, J. *et al.* Combined nivolumab and ipilimumab or monotherapy in untreated Melanoma. *N. Engl. J. Med.* (2015). doi:10.1056/NEJMoa1504030
25. Michot, J. M. *et al.* Immune-related adverse events with immune checkpoint blockade: A comprehensive review. *European Journal of Cancer* (2016). doi:10.1016/j.ejca.2015.11.016
26. Callahan, M. K., Postow, M. A. & Wolchok, J. D. Targeting T Cell Co-receptors for Cancer Therapy. *Immunity* **44**, 1069–1078 (2016).
27. Sosa, A., Lopez Cadena, E., Simon Olive, C., Karachaliou, N. & Rosell, R. Clinical assessment of immune-related adverse events. *Therapeutic Advances in Medical Oncology* **10**, (2018).
28. Lemiale, V. *et al.* Severe toxicity from checkpoint protein inhibitors: What intensive care physicians need to know? *Annals of Intensive Care* (2019). doi:10.1186/s13613-019-0487-x
29. Sharma, P., Hu-Lieskovan, S., Wargo, J. A. & Ribas, A. Primary, Adaptive, and Acquired Resistance to Cancer Immunotherapy. *Cell* **168**, 707–723 (2017).
30. Ribas, A. Adaptive immune resistance: How cancer protects from immune attack. *Cancer Discovery* **5**, 915–919 (2015).
31. Yu, X. *et al.* The surface protein TIGIT suppresses T cell activation by promoting the generation of mature immunoregulatory dendritic cells. *Nat. Immunol.* **10**, 48–57 (2009).

32. Levin, S. D. *et al.* Vstm3 is a member of the CD28 family and an important modulator of T-cell function. *Eur. J. Immunol.* **41**, 902–915 (2011).

33. Boles, K. S. *et al.* A novel molecular interaction for the adhesion of follicular CD4 T cells to follicular DC. *Eur. J. Immunol.* **39**, 695–703 (2009).

34. Lozano, E., Dominguez-Villar, M., Kuchroo, V. & Hafler, D. A. The TIGIT/CD226 Axis Regulates Human T Cell Function. *J. Immunol.* **188**, 3869–3875 (2012).

35. Johnston, R. J. *et al.* The Immunoreceptor TIGIT Regulates Antitumor and Antiviral CD8+ T Cell Effector Function. *Cancer Cell* **26**, 923–937 (2014).

36. Joller, N. *et al.* Treg cells expressing the coinhibitory molecule TIGIT selectively inhibit proinflammatory Th1 and Th17 cell responses. *Immunity* (2014). doi:10.1016/j.immuni.2014.02.012

37. Rodriguez-Abreu, D. *et al.* Primary analysis of a randomized, double-blind, phase II study of the anti-TIGIT antibody tiragolumab (tira) plus atezolizumab (atezo) versus placebo plus atezo as first-line (1L) treatment in patients with PD-L1-selected NSCLC (CITYSCAPE). *J. Clin. Oncol.* **38**, 9503–9503 (2020).

38. Monney, L. *et al.* Th1-specific cell surface protein Tim-3 regulates macrophage activation and severity of an autoimmune disease. *Nature* **415**, 536–541 (2002).

39. Fourcade, J. *et al.* Upregulation of Tim-3 and PD-1 expression is associated with tumor antigen-specific CD8+ T cell dysfunction in melanoma patients. *J. Exp. Med.* **207**, 2175–2186 (2010).

40. Sakuishi, K. *et al.* Targeting Tim-3 and PD-1 pathways to reverse T cell exhaustion and restore anti-tumor immunity. *J. Exp. Med.* (2010). doi:10.1084/jem.20100643

41. Fourcade, J. *et al.* Upregulation of Tim-3 and PD-1 expression is associated with tumor antigen–specific CD8 + T cell dysfunction in melanoma patients. *J. Exp. Med.* **207**, 2175–2186 (2010).

42. Zhou, Q. *et al.* Coexpression of Tim-3 and PD-1 identifies a CD8+ T-cell exhaustion phenotype in mice with disseminated acute myelogenous leukemia. *Blood* (2011). doi:10.1182/blood-2010-10-310425

43. Ngiow, S. F. *et al.* Anti-TIM3 antibody promotes T cell IFN-γ-mediated antitumor immunity and suppresses established tumors. *Cancer Res.* (2011). doi:10.1158/0008-5472.CAN-11-0096

44. Koyama, S. *et al.* Adaptive resistance to therapeutic PD-1 blockade is associated with upregulation of alternative immune checkpoints. *Nat. Commun.* **7**, 10501 (2016).

45. Acharya, N., Acharya, N., Sabatos-Peyton, C., Anderson, A. C. & Anderson, A. C. Tim-3 finds its place in the cancer immunotherapy landscape. *J. Immunother. Cancer* **8**, 911 (2020).

46. Imai, K. & Takaoka, A. Comparing antibody and small-molecule therapies for cancer. *Nature Reviews Cancer* **6**, 714–727 (2006).

47. Lee, C. M. & Tannock, I. F. The distribution of the therapeutic monoclonal antibodies cetuximab and trastuzumab within solid tumors. *BMC Cancer* **10**, (2010).

48. Teng, M. W. L., Ngiow, S. F., Ribas, A. & Smyth, M. J. Classifying cancers basedon T-cell infiltration and PD-L1. *Cancer Research* **75**, 2139–2145 (2015).

49. Centanni, M., Moes, D. J. A. R., Trocóniz, I. F., Ciccolini, J. & van Hasselt, J. G.

C. Clinical Pharmacokinetics and Pharmacodynamics of Immune Checkpoint Inhibitors. *Clinical Pharmacokinetics* **58**, 835–857 (2019).

50. Patnaik, A. *et al.* Phase i study of pembrolizumab (MK-3475; Anti-PD-1 monoclonal antibody) in patients with advanced solid tumors. *Clin. Cancer Res.* (2015). doi:10.1158/1078-0432.CCR-14-2607

51. Brahmer, J. R. *et al.* Phase I study of single-agent anti-programmed death-1 (MDX-1106) in refractory solid tumors: Safety, clinical activity, pharmacodynamics, and immunologic correlates. *J. Clin. Oncol.* (2010). doi:10.1200/JCO.2009.26.7609

52. Wang, Y. M. C. *et al.* Evaluating and Reporting the Immunogenicity Impacts for Biological Products—a Clinical Pharmacology Perspective. *AAPS J.* **18**, 395–403 (2016).

53. Brummelen, E. M. J., Ros, W., Wolbink, G., Beijnen, J. H. & Schellens, J. H. M. Antidrug Antibody Formation in Oncology: Clinical Relevance and Challenges. *Oncologist* **21**, 1260–1268 (2016).

54. Bloem, K., Hernández-Breijo, B., Martínez-Feito, A. & Rispens, T. Immunogenicity of Therapeutic Antibodies: Monitoring Antidrug Antibodies in a Clinical Context. *Ther. Drug Monit.* **39**, 327–332 (2017).

55. Sailstad, J. M. *et al.* A white paper-consensus and recommendations of a global harmonization team on assessing the impact of immunogenicity on pharmacokinetic measurements. *AAPS Journal* **16**, 488–498 (2014).

56. Opdivo (nivolumab) Prescribing Information. (2018). Available at: https://packageinserts.bms.com/pi/pi_opdivo.pdf. (Accessed: 1st April 2020)

57. Beasley, D. The cost of cancer: new drugs show success at a steep price - Reuters. (2017). Available at: https://www.reuters.com/article/us-usa-healthcare-cancer-costs/the-cost-of-cancer-new-drugs-show-success-at-a-steep-price-idUSKBN1750FU. (Accessed: 1st April 2020)

58. Elvidge, S. NICE opts not to recommend Opdivo for head and neck cancer | BioPharma Dive. (2017). Available at: https://www.biopharmadive.com/news/nice-opts-not-to-recommend-opdivo-for-head-and-neck-cancer/440344/. (Accessed: 1st April 2020)

59. Smith, W. M. *et al.* Therapeutic targeting of immune checkpoints with small molecule inhibitors. *American Journal of Translational Research* **11**, 529–541 (2019).

60. Musielak, B. *et al.* CA-170 - A Potent Small-Molecule PD-L1 Inhibitor or Not? *Molecules* **24**, (2019).

61. Perry, E. Discovery of small molecule inhibitors of immune checkpoint proteins. (Vanderbilt University, 2019).

62. Perry, E. *et al.* Fragment-based screening of programmed death ligand 1 (PD-L1). *Bioorganic Med. Chem. Lett.* **29**, 786–790 (2019).

63. Shuker, S. B., Hajduk, P. J., Meadows, R. P. & Fesik, S. W. Discovering high-affinity ligands for proteins: SAR by NMR. *Science (80-.).* **274**, 1531–1534 (1996).

64. Erlanson, D. A., Fesik, S. W., Hubbard, R. E., Jahnke, W. & Jhoti, H. Twenty years on: the impact of fragments on drug discovery. *Nat. Rev. Drug Discov.* **15**, 605–19 (2016).

65. Hall, R. J., Mortenson, P. N. & Murray, C. W. Efficient exploration of chemical space by fragment-based screening. *Prog. Biophys. Mol. Biol.* (2014). doi:10.1016/j.pbiomolbio.2014.09.007

66. Scott, D. E., Coyne, A. G., Hudson, S. A. & Abell, C. Fragment-Based Approaches in Drug Discovery and Chemical Biology. (2012). doi:10.1021/bi3005126

67. Harner, M. J., Frank, A. O. & Fesik, S. W. Fragment-based drug discovery using NMR spectroscopy. *Journal of Biomolecular NMR* **56**, 65–75 (2013).

68. Schanda, P., Kupĉe, E. & Brutscher, B. SOFAST-HMQC experiments for recording two-dimensional deteronuclear correlation spectra of proteins within a few seconds. *J. Biomol. NMR* (2005). doi:10.1007/s10858-005-4425-x

69. Harner, M. J., Mueller, L., Robbins, K. J. & Reily, M. D. NMR in drug design. *Arch. Biochem. Biophys.* (2017). doi:10.1016/j.abb.2017.06.005

70. Patschull, A. O. M., Gooptu, B., Ashford, P., Daviter, T. & Nobeli, I. In silico assessment of potential druggable pockets on the surface of α1-antitrypsin conformers. *PLoS One* (2012). doi:10.1371/journal.pone.0036612

71. Schmidtke, P. & Barril, X. Understanding and predicting druggability. A high-throughput method for detection of drug binding sites. *J. Med. Chem.* (2010). doi:10.1021/jm100574m

72. Hajduk, P. J., Huth, J. R. & Fesik, S. W. Druggability indices for protein targets derived from NMr-based screening data. *J. Med. Chem.* **48**, 2518–2525 (2005).

73. Aretz, J. *et al.* Chemical fragment arrays for rapid druggability assessment. *Chem. Commun.* **52**, 9067–9070 (2016).

74. Stanietsky, N. *et al.* The interaction of TIGIT with PVR and PVRL2 inhibits human NK cell cytotoxicity. *Proc. Natl. Acad. Sci.* **106**, 17858–17863 (2009).

75. Stengel, K. F. *et al.* Structure of TIGIT immunoreceptor bound to poliovirus receptor reveals a cell-cell adhesion and signaling mechanism that requires cis-trans receptor clustering. *Proc. Natl. Acad. Sci.* **109**, 5399–5404 (2012).

76. Kurtulus, S. *et al.* TIGIT predominantly regulates the immune response via regulatory T cells. *J. Clin. Invest.* **125**, 4053–4062 (2015).

77. Chauvin, J.-M. *et al.* TIGIT and PD-1 impair tumor antigen – specific CD8 + T cells in melanoma patients. *J. Clin. Invest.* **125**, 1–13 (2015).

78. Stanietsky, N. *et al.* Mouse TIGIT inhibits NK-cell cytotoxicity upon interaction with PVR. *Eur. J. Immunol.* **43**, 2138–2150 (2013).

79. Liu, S. *et al.* Recruitment of Grb2 and SHIP1 by the ITT-like motif of TIGIT suppresses granule polarization and cytotoxicity of NK cells. *Cell Death Differ.* **20**, 456–464 (2013).

80. Li, M. *et al.* T-cell immunoglobulin and ITIM domain (TIGIT) receptor/poliovirus receptor (PVR) ligand engagement suppresses interferon-γ production of natural killer cells via β-arrestin 2-mediated negative signaling. *J. Biol. Chem.* **289**, 17647–17657 (2014).

81. Manieri, N. A., Chiang, E. Y. & Grogan, J. L. TIGIT: A Key Inhibitor of the Cancer Immunity Cycle. *Trends Immunol.* **38**, 20–28 (2017).

82. Joller, N. *et al.* Cutting Edge: TIGIT Has T Cell-Intrinsic Inhibitory Functions. *J. Immunol.* **186**, 1338–1342 (2011).

83. Kourepini, E. *et al.* TIGIT Enhances Antigen-Specific Th2 Recall Responses and

Allergic Disease. *J. Immunol.* **196**, 3570–3580 (2016).

84. Fuhrman, C. A. *et al.* Divergent Phenotypes of Human Regulatory T Cells Expressing the Receptors TIGIT and CD226. *J. Immunol.* (2015). doi:10.4049/jimmunol.1402381

85. Kong, Y. *et al.* T-cell immunoglobulin and ITIM domain (TIGIT) associates with CD8+ T-cell exhaustion and poor clinical outcome in AML patients. *Clin. Cancer Res.* **22**, 3057–3066 (2016).

86. Inozume, T. *et al.* Melanoma cells control antimelanoma CTL responses via interaction between TIGIT and CD155 in the effector phase. *J. Invest. Dermatol.* (2016). doi:10.1038/JID.2015.404

87. Casado, J. G. *et al.* Expression of adhesion molecules and ligands for activating and costimulatory receptors involved in cell-mediated cytotoxicity in a large panel of human melanoma cell lines. *Cancer Immunology, Immunotherapy* **58**, 1517–1526 (2009).

88. Mendelsohn, C. L., Wimmer, E. & Racaniello, V. R. Cellular receptor for poliovirus: Molecular cloning, nucleotide sequence, and expression of a new member of the immunoglobulin superfamily. *Cell* **56**, 855–865 (1989).

89. Dougall, W. C., Kurtulus, S., Smyth, M. J. & Anderson, A. C. TIGIT and CD96: new checkpoint receptor targets for cancer immunotherapy. *Immunol. Rev.* **276**, 112–120 (2017).

90. Bancet, A. *et al.* Fragment Linking Strategies for Structure-Based Drug Design. *J. Med. Chem.* **63**, 11420–11435 (2020).

91. Miyake, Y. *et al.* Identification of novel lysine demethylase 5-selective inhibitors by

inhibitor-based fragment merging strategy. *Bioorganic Med. Chem.* **27**, 1119–1129 (2019).

92. Otwinowski, Z. & Minor, W. Processing of X-ray diffraction data collected in oscillation mode. *Methods Enzymol.* **276**, 307–326 (1997).

93. McCoy, A. J. *et al.* Phaser crystallographic software. *J. Appl. Crystallogr.* **40**, 658–674 (2007).

94. Adams, P. D. *et al.* PHENIX: Building new software for automated crystallographic structure determination. in *Acta Crystallographica Section D: Biological Crystallography* **58**, 1948–1954 (International Union of Crystallography, 2002).

95. Gandhi, A. K. *et al.* High resolution X-ray and NMR structural study of human T-cell immunoglobulin and mucin domain containing protein-3. *Sci. Rep.* **8**, 17512 (2018).

96. Schrödinger, LLC. *The {PyMOL} Molecular Graphics System, Version~1.8*. (2015).

97. Anderson, A. C. Tim-3: An Emerging Target in the Cancer Immunotherapy Landscape. *Cancer Immunol. Res.* (2014). doi:10.1158/2326-6066.cir-14-0039

98. Li, H. *et al.* Tim-3/galectin-9 signaling pathway mediates T-cell dysfunction and predicts poor prognosis in patients with hepatitis B virus-associated hepatocellular carcinoma. *Hepatology* **56**, 1342–1351 (2012).

99. Japp, A. S. *et al.* Dysfunction of PSA-specific CD8+ T cells in prostate cancer patients correlates with CD38 and Tim-3 expression. *Cancer Immunol. Immunother.* **64**, 1487–1494 (2015).

100. Gao, X. *et al.* TIM-3 expression characterizes regulatory T cells in tumor tissues

and is associated with lung cancer progression. *PLoS One* (2012). doi:10.1371/journal.pone.0030676

101. Yan, J. *et al.* Tim-3 Expression Defines Regulatory T Cells in Human Tumors. *PLoS One* (2013). doi:10.1371/journal.pone.0058006
102. Wiener, Z. *et al.* TIM-3 is expressed in melanoma cells and is upregulated in TGF-beta stimulated mast cells. *J. Invest. Dermatol.* (2007). doi:10.1038/sj.jid.5700616
103. Shang, Y., Li, Z., Li, H., Xia, H. & Lin, Z. TIM-3 expression in human osteosarcoma: Correlation with the expression of epithelial-mesenchymal transition-specific biomarkers. *Oncol. Lett.* (2013). doi:10.3892/ol.2013.1410
104. Cao, Y. *et al.* Tim-3 Expression in Cervical Cancer Promotes Tumor Metastasis. *PLoS One* (2013). doi:10.1371/journal.pone.0053834
105. Komohara, Y. *et al.* The coordinated actions of TIM-3 on cancer and myeloid cells in the regulation of tumorigenicity and clinical prognosis in clear cell renal cell carcinomas. *Cancer Immunol. Res.* (2015). doi:10.1158/2326-6066.CIR-14-0156
106. Das, M., Zhu, C. & Kuchroo, V. K. Tim-3 and its role in regulating anti-tumor immunity. *Immunol. Rev.* **276**, 97–111 (2017).
107. Huang, X. *et al.* Lymphoma endothelium preferentially expresses Tim-3 and facilitates the progression of lymphoma by mediating immune evasion. *J. Exp. Med.* (2010). doi:10.1084/jem.20090397
108. Silva, I. G., Gibbs, B. F., Bardelli, M., Varani, L. & Sumbayev, V. V. Differential expression and biochemical activity of the immune receptor Tim-3 in healthy and malignant human myeloid cells. *Oncotarget* (2015). doi:10.18632/oncotarget.5257
109. Borate, U. *et al.* Phase Ib Study of the Anti-TIM-3 Antibody MBG453 in

Combination with Decitabine in Patients with High-Risk Myelodysplastic Syndrome (MDS) and Acute Myeloid Leukemia (AML). *Blood* (2019). doi:10.1182/blood-2019-128178

110. Harding, J. J. *et al.* A phase Ia/Ib study of an anti-TIM-3 antibody (LY3321367) monotherapy or in combination with an anti-PD-L1 antibody (LY3300054): Interim safety, efficacy, and pharmacokinetic findings in advanced cancers. *J. Clin. Oncol.* **37**, 12–12 (2019).
111. Yuan, S. *et al.* TIM-1 acts a dual-attachment receptor for Ebolavirus by interacting directly with viral GP and the PS on the viral envelope. *Protein Cell* **6**, 814–824 (2015).
112. Santiago, C. *et al.* Structures of T Cell Immunoglobulin Mucin Protein 4 Show a Metal-Ion-Dependent Ligand Binding Site where Phosphatidylserine Binds. *Immunity* **27**, 941–951 (2007).
113. DeKruyff, R. H. *et al.* T Cell/Transmembrane, Ig, and Mucin-3 Allelic Variants Differentially Recognize Phosphatidylserine and Mediate Phagocytosis of Apoptotic Cells. *J. Immunol.* **184**, 1918–1930 (2010).
114. Chiba, S. *et al.* Tumor-infiltrating DCs suppress nucleic acid-mediated innate immune responses through interactions between the receptor TIM-3 and the alarmin HMGB1. *Nat. Immunol.* **13**, 832–842 (2012).
115. Zhu, C. *et al.* The Tim-3 ligand galectin-9 negatively regulates T helper type 1 immunity. *Nat. Immunol.* **6**, 1245–1252 (2005).
116. Huang, Y.-H. *et al.* CEACAM1 regulates TIM-3-mediated tolerance and exhaustion. *Nature* **517**, 386–390 (2015).

117. Cao, E. *et al.* T Cell Immunoglobulin Mucin-3 Crystal Structure Reveals a Galectin-9-Independent Ligand-Binding Surface. *Immunity* **26**, 311–321 (2007).

118. van de Weyer, P. S. *et al.* A highly conserved tyrosine of Tim-3 is phosphorylated upon stimulation by its ligand galectin-9. *Biochem. Biophys. Res. Commun.* (2006). doi:10.1016/j.bbrc.2006.10.079

119. Rangachari, M. *et al.* Bat3 promotes T cell responses and autoimmunity by repressing Tim-3-mediated cell death and exhaustion. *Nat. Med.* **18**, 1394–1400 (2012).

120. Lee, J. *et al.* Phosphotyrosine-dependent coupling of Tim-3 to T-cell receptor signaling pathways. *Mol. Cell. Biol.* **31**, 3963–74 (2011).

121. Wolf, Y., Anderson, A. C. & Kuchroo, V. K. TIM3 comes of age as an inhibitory receptor. *Nature Reviews Immunology* **20**, 173–185 (2020).

122. Finger, C., Escher, C. & Schneider, D. The single transmembrane domains of human receptor tyrosine kinases encode self-interactions. *Sci. Signal.* **2**, ra56–ra56 (2009).

123. Godfroy, J. I., Roostan, M., Moroz, Y. S., Korendovych, I. V. & Yin, H. Isolated Toll-like Receptor Transmembrane Domains Are Capable of Oligomerization. *PLoS One* **7**, e48875 (2012).

124. Westerfield, J. M. & Barrera, F. N. Membrane receptor activation mechanisms and transmembrane peptide tools to elucidate them. *Rev. 1792 J. Biol. Chem* 1792–1814 (2019). doi:10.1074/jbc.REV119.009457

125. LIU, N. *et al.* Crystal structures of human TIM members: Ebolavirus entry-enhancing receptors. *Chinese Sci. Bull.* **60**, 3438–3453 (2015).

126. Atchison, D. K. & Beierwaltes, W. H. The influence of extracellular and intracellular calcium on the secretion of renin. *Pflugers Archiv European Journal of Physiology* **465**, 59–69 (2013).

127. Huang, Y.-H. *et al.* Corrigendum: CEACAM1 regulates TIM-3-mediated tolerance and exhaustion. *Nature* **536**, 359–359 (2016).

128. Williamson, M. P. Using chemical shift perturbation to characterise ligand binding. *Prog. Nucl. Magn. Reson. Spectrosc.* **73**, 1–16 (2013).

129. Bonsor, D. A., Günther, S., Beadenkopf, R., Beckett, D. & Sundberg, E. J. Diverse oligomeric states of CEACAM IgV domains. *Proc. Natl. Acad. Sci. U. S. A.* **112**, 13561–13566 (2015).

130. Nagaishi, T., Iijima, H., Nakajima, A., Chen, D. & Blumberg, R. S. Role of CEACAM1 as a regulator of T cells. in *Annals of the New York Academy of Sciences* **1072**, 155–175 (Blackwell Publishing Inc., 2006).

131. Kuespert, K., Pils, S. & Hauck, C. R. CEACAMs: their role in physiology and pathophysiology. *Current Opinion in Cell Biology* **18**, 565–571 (2006).

132. Sabatos-Peyton, C. A. *et al.* Blockade of Tim-3 binding to phosphatidylserine and CEACAM1 is a shared feature of anti-Tim-3 antibodies that have functional efficacy. (2018). doi:10.1080/2162402X.2017.1385690

133. Schanda, P. & Brutscher, B. Very fast two-dimensional NMR spectroscopy for real-time investigation of dynamic events in proteins on the time scale of seconds. *J. Am. Chem. Soc.* **127**, 8014–8015 (2005).

134. Nikolovska-Coleska, Z. *et al.* Development and optimization of a binding assay for the XIAP BIR3 domain using fluorescence polarization. (2004).

doi:10.1016/j.ab.2004.05.055

135. Dudev, T. & Lim, C. Monodentate versus Bidentate Carboxylate Binding in Magnesium and Calcium Proteins: What are the Basic Principles? *J. Phys. Chem. B* **108**, 4546–4557 (2004).

136. Weber, J. K. & Zhou, R. Phosphatidylserine-induced conformational modulation of immune cell exhaustion-associated receptor TIM3. *Sci. Rep.* **7**, 1–10 (2017).

137. Nakayama, M. *et al.* Tim-3 mediates phagocytosis of apoptotic cells and cross-presentation. *Blood* **113**, 3821–3830 (2009).

138. Saad, E. Ben, Oroya, A. & Rudd, C. E. Abstract 6528: Anti-PD-1 induces the endocytosis of the co-receptor from the surface of T-cells: Nivolumab is more effective than Pembrolizumab. in *Cancer Research* **80**, 6528–6528 (American Association for Cancer Research (AACR), 2020).

139. Li, C. W. *et al.* Eradication of Triple-Negative Breast Cancer Cells by Targeting Glycosylated PD-L1. *Cancer Cell* **33**, 187-201.e10 (2018).

140. Zhang, Y. *et al.* Hijacking antibody-induced CTLA-4 lysosomal degradation for safer and more effective cancer immunotherapy. *Cell Res.* **29**, 609–627 (2019).

141. Kuang, Z. *et al.* A novel antibody targeting TIM-3 resulting in receptor internalization for cancer immunotherapy. *Antib. Ther.* **3**, 227–236 (2020).

142. Park, J.-J. *et al.* Checkpoint inhibition through small molecule-induced internalization of programmed death-ligand 1. doi:10.1038/s41467-021-21410-1

143. Banik, S. M. *et al.* Lysosome-targeting chimaeras for degradation of extracellular proteins. *Nature* **584**, 291–297 (2020).

144. Sun, X. *et al.* Protacs: Great opportunities for academia and industry. *Signal*

Transduction and Targeted Therapy **4**, 1–33 (2019).

145. Mullard, A. Targeted protein degraders crowd into the clinic. *Nature reviews. Drug discovery* **20**, 247–250 (2021).

146. Ahn, G. *et al.* LYTACs that engage the asialoglycoprotein receptor for targeted protein degradation. *Nat. Chem. Biol.* 1–10 (2021). doi:10.1038/s41589-021-00770-1

147. Hunter, C. A. & Sanders, J. K. M. The Nature of π-π Interactions. *J. Am. Chem. Soc.* **112**, 5525–5534 (1990).